Modeling Regional Aerosol and Aerosol Precursor Variability over California and Its Sensitivity to Emissions and Long-Range Transport during the 2010 CalNex and CARES Campaigns

Jerome D. Fast[1], James Allan[2], Roya Bahreini[3,4], Jill Craven[5], Louisa Emmons[6], Richard Ferrare[7], Patrick L. Hayes[3,15], Alma Hodzic[6], John Holloway[3,4], Chris Hostetler[7], Jose L. Jimenez[3], Haflidi Jonsson[8], Shang Liu[9], Ying Liu[1], Andrew Metcalf[5,16], Ann Middlebrook[4], John Nowak[10], Mikhail Pekour[1], Anne Perring[3,4], Lynn Russell[11], Art Sedlacek[12], John Seinfeld[5], Ari Setyan[14], John Shilling[1], Manishkumar Shrivastava[1], Steven Springston[12], Chen Song[1], R. Subramanian[13], Jonathan W. Taylor[2], V. Vinoj[1,17], Qing Yang[1], Rahul A. Zaveri[1], and Qi Zhang[14]

[1]Pacific Northwest National Laboratory, Richland, Washington, USA
[2]University of Manchester, Manchester, UK
[3]Cooperative Institute for Research in Environmental Sciences, University of Colorado, Boulder, Colorado, USA
[4]Earth System Research Laboratory, National Oceanic and Atmospheric Administration, Boulder, Colorado, USA
[5]California Institute of Technology, Pasadena, California, USA
[6]National Center for Atmospheric Research, Boulder, Colorado, USA
[7]NASA Langley Research Center, Hampton, Virginia, USA
[8]Center for Interdisciplinary Remotely-Piloted Aerosol Studies, Marina, California, USA
[9]Los Alamos National Laboratory, Los Alamos, New Mexico, USA
[10]Aerodyne, Inc. Billerica, Massachusetts, USA
[11]Scripps Institute of Oceanography, University of California – San Diego, San Diego, California, USA
[12]Brookhaven National Laboratory, Upton, New York, USA
[13]Carnegie Mellon University, Pittsburgh, Pennsylvania, USA
[14]University of California – Davis, Davis, California, USA
[15]Now at Université de Montréal, Montréal, Québec, Canada
[16]Now at University of Minnesota – Twin Cities, Minneapolis, Minnesota, USA
[17]Now at Indian Institute of Technology, Bhubaneswar, India

Jerome D. Fast, jerome.fast@pnnl.gov
James Allan, James.Allan@manchester.ac.uk
Roya Bahreini, bahreini@ucr.edu
Jill Craven, craven@caltech.edu
Louisa Emmons, emmons@ucar.edu
Richard Ferrare, richard.a.ferrare@nasa.gov
Patrick L. Hayes, patricklewishayes@gmail.com
Alma Hodzic, alma@ucar.edu
John Holloway, john.s.holloway@noaa.gov
Chris Hostetler, chris.a.hostetler@nasa.gov
Jose L. Jimenez, jlj.colorado@gmail.com
Haflidi Jonsson, hjonsson@nps.edu
Shang Liu, sliu@lanl.gov
Ying Liu, ying.liu@pnnl.gov
Andrew Metcalf, andrewrmetcalf@gmail.com
Ann Middlebrook, ann.m.middlebrook@noaa.gov
John Nowak, jnowak@aerodyne.com

Mikhail Pekour, mikhail.pekour@pnnl.gov
Anne Perring, anne.perring@noaa.gov
Lynn Russell, lmrussell@ucsd.edu
Art Sedlacek, sedlacek@bnl.gov
John Seinfeld, seinfeld@caltech.edu
Ari Setyan, ari.setyan@gmail.com
John Shilling, john.shilling@pnnl.gov
Manishkumar Shrivastava, manishkumar.shrivastava@pnnl.gov
Steven Springston, srs@bnl.gov
Chen Song, scqz@hotmail.com
R. Subramanian, subu@cmu.edu
Jonathan W. Taylor, jonathan.taylor@manchester.ac.uk
V. Vinoj, vinoj@iitbbs.ac.in
Qing Yang, qing.yang@pnnl.gov
Rahul A. Zaveri, Rahul.zaveri@pnnl.gov
Qi Zhang, dkwzhang@ucdavis.edu

Modeling Regional Aerosol and Aerosol Precursor Variability over California and Its Sensitivity to Emissions and Long-Range Transport during the 2010 CalNex and CARES Campaigns

Abstract

The performance of the Weather Research and Forecasting regional model with chemistry (WRF-Chem) in simulating the spatial and temporal variations in aerosol mass, composition, and size over California is quantified using the extensive meteorological, trace gas, and aerosol measurements collected during the California Nexus of Air Quality and Climate Experiment (CalNex) and the Carbonaceous Aerosol and Radiative Effects Study (CARES) conducted during May and June of 2010. The overall objective of the field campaigns was to obtain data needed to better understand processes that affect both climate and air quality, including emission assessments, transport and chemical aging of aerosols, aerosol radiative effects. Simulations were performed that examined the sensitivity of aerosol concentrations to anthropogenic emissions and to long-range transport of aerosols into the domain obtained from a global model. The configuration of WRF-Chem used in this study is shown to reproduce the overall synoptic conditions, thermally-driven circulations, and boundary layer structure observed in region that controls the transport and mixing of trace gases and aerosols. Reducing the default emissions inventory by 50% led to an overall improvement in many simulated trace gases and black carbon aerosol at most sites and along most aircraft flight paths; however, simulated organic aerosol was closer to observed when there were no adjustments to the primary organic aerosol emissions. We found that sulfate was better simulated over northern California whereas nitrate was better simulated over southern California. While the overall spatial and temporal variability of aerosols and their precursors were simulated reasonably well, we show cases where the local transport of some aerosol plumes were either too slow or too fast, which adversely affects the statistics quantifying the differences between observed and simulated quantities. Comparisons with lidar and in-situ measurements indicate that long-range transport of aerosols from the global model was likely too high in the free troposphere even though their concentrations were relatively low. This bias led to an over-prediction in aerosol optical depth by as much as a factor of two that offset the under-predictions of boundary-layer extinction resulting primarily from local emissions. Lowering the boundary conditions of aerosol concentrations by 50% greatly reduced the bias in simulated aerosol optical depth for all regions of California. This study shows that quantifying regional-scale variations in aerosol radiative forcing and determining the relative role of emissions from local and distant sources is challenging during 'clean' conditions and that a wide array of measurements are needed to ensure model predictions are correct for the right reasons. In this regard, the combined CalNex and CARES datasets are an ideal testbed that can be used to evaluate aerosol models in great detail and develop improved treatments for aerosol processes.

1 Introduction

Accurately simulating aerosol number, mass, composition, size distribution, and hygroscopicity continues to be a major challenge for air quality and climate models. There are several factors that contribute to errors in regional-scale model predictions of aerosol properties. First, it is well known that the complex spatial and temporal variability in human activities (e.g. fossil fuel uses, biomass burning) and natural sources (e.g. biological emissions, dust, sea-salt) contribute to uncertainties in trace gas precursor and primary aerosol emission estimates. Emission inventories suitable for regional models have been developed by many organizations for specific cities, regions, or countries, but they are often rely on different assumptions and apply only for specific time periods [e.g. *Granier et al*., 2011]. Second, errors arising from meteorological parameterizations in regional models directly affect the simulated aerosol lifecycle. Meteorological processes that have large uncertainties include, turbulent vertical mixing that affects the dilution and chemical processing of aerosols and their precursors [e.g. *Aan de Brugh et al*., 2012; *Nilsson et al*., 2001], vertical motions associated with sub-grid scale clouds that affect the vertical transport of aerosols [e.g. *Gustafson et al*., 2008], the spatial extent and lifetime of clouds that affects aerosol chemical and size transformation within clouds [e.g. *Ervens et al*., 2011; *Fahey and Pandis*, 2001] and photochemistry above and below clouds [e.g. *Feng et al.,* 2004; *Tang et al*., 2003], and precipitation that controls wet removal of aerosols and their trace gas precursors [e.g. *Wang et al*., 2013; *Yang et al*., 2012; *Barth et al.*, 2007]. Third, the level of complexity in the treatment of aerosol chemistry (equilibrium versus dynamic approach for gas-to-particle partitioning, the number of aerosol species and gas-phase precursors) [e.g. *Baklanov et al*., 2014] and size distribution (bulk, modal, and sectional approaches) varies among models. A fourth factor is the incomplete understanding of secondary organic aerosol (SOA) formation, aging, and removal based on laboratory and field studies, which leads to large uncertainties in simulated SOA [e.g. *Heald et al*., 2011; *Spracklen et al*., 2011; *Hodzic et al*., 2013]. The spatial resolution of regional models contributes to all four of these factors, but the implications of ignoring the sub-grid scale variability of aerosol properties [*Qian et al.,* 2010; *Gustafson et al.,* 2011] is largely unexplored. Therefore, inadequate resolution of the large observed spatial and temporal variability of aerosols is a fifth factor. Finally, regional model predictions are often influenced by boundary conditions that are either specified by prescribed climatological values or obtained from coarser global models that can represent long-range transport of trace gases and aerosols that affect local concentrations. Therefore a sixth factor consists of errors from global model predictions that are propagated into the regional model domains. It is likely that one or more of these six factors are more significant for some regions than others.

Previous chemical transport modeling studies over the continental U.S. have shown geographical variations in model performance. For example, *Kang et al*. [2010] used the CMAQ model with a

horizontal grid spacing of 12 km over the continental U.S. for a one-year period and showed that $PM_{2.5}$ concentrations were generally too low over the eastern U.S. during the summer of 2007 and too high during the winter months of 2007. The model performance was more variable in California, a region with large topographic, land use, and population variations, with positive biases at some stations and negative biases at other stations. A simulation over the continental U.S. for 2009 using the GEOS-Chem model [*Walker et al*., 2012] with a horizontal grid spacing of 0.5^{o} x 0.67^{o} showed that while predicted annual mean sulfate concentrations over the continental U.S. were similar to observations, nitrate and ammonium were too high over the eastern and mid-western U.S. and too low over California where the observed concentrations were the highest. They indicated that the bias in nitrate over California was likely due to both ammonia emission estimates that were too low and simulated boundary-layer depths that were too high. *Heald et* al. [2012] reported similar spatial variations in the biases in sulfate and nitrate over the U.S. during 2004, 2009, and 2010 from their GEOS-Chem simulations over North America. *Huang et al*. [2012] used the STEM model with a 60 km grid spacing to show that the performance in simulating surface black carbon over a two-week period during June, 2008 varied over the U.S., with the largest negative biases in the southeastern U.S. and the highest positive biases over the northeastern U.S. They also noted that black carbon was also ~30% too low on average for surface sites in the southwestern U.S. and that the differences in simulated vertical profiles of black carbon compared with NASA DC-8 aircraft data over California could be attributed to the coarse spatial grid spacing that does not permit the model to resolve the variability in meteorology associated with topographic variations in the vicinity of Los Angeles and the San Joaquin Valley.

Several field campaigns have been conducted in California to collect data needed to better understand and characterize ozone and particulates in the region and to address modeling challenges using higher spatial resolution that better represents the terrain inhomogeneity in California. These campaigns include the Southern California Air Quality Study (SCAQS) conducted in August 1987 [*Lawson*, 1990], the South Coast Air Basin of California (SoCAB) study during September 1993 [*Frasier et al.*, 1996], the Southern California Ozone Study (SCOS) conducted between June and October of 1997 [*Croes and Fujita*, 2003], the 1999-2001 California Regional Particulate Air Quality Study (CRPAQS) conducted between December 1999 to February 2001 [*Chow et al.,* 2006], the 2000 Central California Ozone Study (CCOS) [*Fujita et al.*, 2005], the Study of Organic Aerosols at Riverside (SOAR) conducted between July and August 2005 [*Docherty et al.,* 2011], the Biosphere Effects on AeRosols and Photochemistry Experiment (BEARPEX) conducted between August and October 2007 [*Bouvier-Brown et al*., 2009], and the Arctic Research of the Composition of the Troposphere from Aircraft and Satellites - California Air Resources Board (ARCTAS-CARB) experiment conducted in June 2008 [*Jacob et al*., 2010]. Many modeling studies that employ these field campaign data have focused on the performance of simulated

meteorology [e.g. *Bao et al*., 2008] and ozone [e.g. *Jacobson*, 2001; *Jin et al.,* 2010; *Lu et al*., 1997]. Modeling studies of aerosol mass, composition, and size distribution using these field campaign data have focused on the performance in regions where concentrations are usually the highest, either in the vicinity of Los Angeles [e.g. *Griffin et al*., 2002; *Held et al*., 2005; *Jacobson*, 1997; *Meng, et al*., 1998; *Vutukuru et al*., 2006; *Zhang et al.*, 2004] or over the San Joaquin Valley [e.g. *Pun et al*., 2009; *Ying and Kleeman*, 2009; *Zhang et al*., 2010]. Since regional-scale models depend on boundary conditions provided by other models, *Huang et al*. [2010] and *Pfister et al.* [2011] use large-scale chemical transport models and ARCTAS-CARB measurements to show that uncertainties in long-range transport of pollution from Asia can lead to errors in simulated regional-scale trace gas and aerosol concentrations over California.

While air quality issues associated with $PM_{2.5}$ concentrations have been the driving factor for previous measurements and modeling studies in California, improving the understanding of regional-scale climate-chemistry interactions and aerosol radiative forcing has received increasing attention in recent years [e.g. *Xu et al*., 2013; *Zhao et al*., 2013]. National and local agencies are interested in knowing the relative contributions of local and upwind anthropogenic pollution and their impact on current and future climate. Understanding the climate impact of aerosols first requires that the aerosol lifecycle be represented reasonably well, which requires that models accurately simulate aerosol composition, size distribution, hygroscopicity, and optical properties in addition to total mass. This is a challenging task. To address model uncertainties associated with climate and air-quality relevant atmospheric processes, two campaigns were conducted in California during the spring and early summer of 2010 that collected extensive meteorological, trace gas, and aerosol data: California Nexus (CalNex): Research at the Nexus of Air Quality and Climate [*Ryerson et al*., 2013] and the Carbonaceous Aerosol and Radiative Effects Study (CARES) [*Zaveri et al.,* 2012]. A few meteorological and aerosol model evaluation studies for this period have been completed. The WRF model with a 4 km horizontal grid spacing was used to evaluate the simulated boundary layer and thermally-driven circulations over central California using CARES measurements [*Fast et al.,* 2012] and the simulated boundary layer and land/sea breezes over the southern California coastal zone using CalNex measurements [*Angevine et al*., 2012]. *Ensberg et al*. [2013] used CalNex ground and aircraft measurements to evaluate predictions of trace gases, inorganic aerosols, and black carbon made by the CMAQ model with a 4 km grid spacing over southern California, while *Knote et al.* [2013] used the CARES and CalNex data and the WRF-Chem model to evaluate the effect of various glyoxal treatments on the formation of SOA.

The combined CalNex and CARES field campaigns provide an unprecedented data set in terms of the number of parameters measured and their spatial and temporal resolution that can be used to evaluate predictions of aerosol concentration, composition, hygroscopicity, and size needed to understand the sources of uncertainties in estimates of aerosol radiative forcing. We have combined the data from these

two field campaigns with other operational monitoring data set into the Aerosol Model Testbed (AMT) framework as described by *Fast et al*. [2011]. The first objective of this study is to evaluate regional-scale predictions of aerosols, aerosol precursors, and meteorological processes affecting aerosols using as much of the measurements collected over California during the field campaign period. While several factors are known to contribute to errors in aerosol predictions, it is not feasible to investigate all of them in a single study. Therefore, our second objective is using the AMT and the CalNex and CARES dataset to investigate two sources of uncertainties, emissions estimates and long-range transport, and their effect on the predictions of aerosols and their precursor over California. In contrast to most previous modeling studies that focus on either the Los Angeles Basin or San Joaquin Valley, the combined CalNex and CARES data set enables the model to be evaluated over a larger region where aerosols are influenced by a wider range of meteorological conditions. Not surprisingly, we find that model performance varies over the region and some trace gases and aerosol species are simulated better than others. The sensitivity simulations show many trace gases and black carbon emissions in the latest emissions inventory are likely too high in the entire region. We also show that while errors in long-range transport do not significantly affect simulated aerosol properties close to the surface near emissions sources, small errors in free tropospheric aerosol concentrations led to a large positive bias in simulated aerosol optical depth. This indicates that regional-scale climate simulations can easily produce erroneous results regarding the relative role of local emissions and long-range transport on local aerosol radiative forcing, even over regions with substantial overall emissions such as California.

A brief description of the field campaign measurements and how they are incorporated into the AMT is included in Section 2. The configuration of the regional aerosol model is described in Section 3. The comparison of the model simulation with the measurements is presented in Section 4, starting with discussion of model performance associated with meteorological and trace gas quantities in Sections. 4.1 and 4.2, respectively. Most of our analysis will focuses on model performance in simulating aerosol properties, divided into carbonaceous aerosols in Section 4.3 and inorganic aerosols in Section 4.4. Section 4.5 presents the model performance on aerosol volume and number distributions. The impact of simulated aerosols on aerosol optical depth and extinction is presented in Section 5 since comparisons with observations is way of evaluating simulated aerosol concentrations throughout a vertical column where in situ measurements may not exist. Section 6 is a discussion that compares the present simulations with those conducted by other CalNex investigators and describes how various model uncertainties contribute to model performance, while Section 7 summarizes our primary findings.

2. Measurements

Measurements collected in California during May and June of 2010 as part of the CalNex and CARES campaigns are used to evaluate mesoscale predictions of aerosols and aerosol precursors. CalNex was designed to address science issues relevant to emission inventory assessment, dispersion of trace gases and aerosols, atmospheric chemistry, and the interactions of aerosols clouds, and radiation [*Ryerson et al*., 2013]. Ground-based instruments were deployed at two sites in southern California as shown in Fig. 1a: one in Pasadena (34.141 ^{o}N, -118.112 ^{o}W, ~240 m MSL) [*Chan et al*., 2013; *Hayes et al*., 2013; *Pennington et al.*, 2012; *Thompson et al*., 2012; *Veres et al*., 2011] and one in Bakersfield (35.346 ^{o}N, -118.965 ^{o}W, ~123 m MSL) [*Alm et al.,* 2012; *Liu et al*., 2012; *Rollins et al*., 2012; 2013; *Zhao et al.* 2013]. Four research aircraft, the NOAA WP-3D, the NOAA Twin Otter, the CIRPAS Twin Otter and the NASA B-200, sampled atmospheric conditions aloft and the NOAA research vessel (R/V) Atlantis sampled atmospheric conditions along the coast of California. In-situ measurements of meteorological, trace gas, and aerosol quantities were collected by the WP-3D [*Bahreini et al*., 2012; *Ryerson et al*., 2013; *Langridge et al.* 2012; *Moore et al*., 2012; *Pollack et al*., 2012; *Warneke et al.,* 2011; *Peischl et al*., 2012], CIRPAS Twin Otter [*Duong et al*., 2011; *Metcalf et al*., 2012; *Craven et al*., 2013; *Hersey et al*., 2013], and the R/V Atlantis. The Tunable Optical Profiler for Aerosols and oZone (TOPAZ) differential absorption lidar (DIAL) was deployed on the NOAA Twin Otter [*Langford et al*., 2012] and the High Spectral Resolution Lidar (HSRL-1) [*Hair et al*., 2008] was deployed on the B-200 [*Scarino et al*., 2013]. As shown in Fig. 1a, most of the CalNex aircraft and research vessel sampling was conducted in southern California in the vicinity of the Los Angeles basin. Ozonesondes were launched at 6 sites to obtain profiles of meteorological quantities along with ozone mixing ratio in the region [*Cooper et al*., 2011]. A detailed description of the instrumentation for each of the CalNex surface sites and mobile platforms is given by *Ryerson et al.* [2013].

CARES was designed to address science issues associated with the interactions of biogenic and anthropogenic precursors on secondary organic aerosol (SOA), black carbon mixing state, and the effects of organic species and aerosol mixing state on optical properties and the activation of cloud condensation nuclei (CCN) [*Zaveri et al*., 2012]. As shown in Fig. 1b, ground-based instruments were deployed at two sites in northern California: one in Sacramento (38.649 ^{o}N, -121.349 ^{o}W, ~30 m MSL) and the other in Cool (38.889 ^{o}N, -120.974 ^{o}W, ~450 m MSL), a small town located about 40 km northeast of Sacramento. The Sacramento and Cool sites are also referred to as "T0" and "T1", respectively, to denote transport time intervals associated with the predominately southwesterly daytime winds. This sampling strategy was based on the known transport pathways of the Sacramento plume that was also observed during BEARPEX [*Bouvier-Brown et al*., 2009]. Three research aircraft, the DOE G-1, the NASA B-200, and the NOAA Twin Otter sampled atmospheric conditions aloft in the vicinity of the T0 and T1

sites. In-situ measurements of meteorological, trace gas, and aerosol quantities were collected by the G-1 while the NOAA Twin Otter and the B-200 had the same remote sensing instrumentation as during CalNex. *Zaveri et al*. [2012] describe the instrumentation for each of the surface sites and mobile platforms. Most of the sampling during CalNex occurred between May 15 and June 16, while sampling during CARES occurred between June 2 and 28.

In addition to the extensive measurements collected from the two campaigns, a wide range of meteorological and air-quality data are routinely collected over California as shown in Figs. 1c and 1d, respectively. Meteorological data collected by several agencies were available from several hundred surface sites, hourly profiles of wind speed and direction were available from 14 radar wind profilers, and profiles of temperature, humidity, pressure, wind speed, and wind direction from radiosondes were launched up to twice a day at four sites in California. An air-quality monitoring network operated by the California Air Resources Board (CARB) provides hourly data on ozone (O_3), nitrogen oxides (NO_x), sulfur dioxide (SO_2), carbon monoxide (CO), $PM_{2.5}$, and PM_{10} at sites throughout California [*http://www.arb.ca.gov/aqd/aqmoninca.htm*]. The Interagency Monitoring of Protected Visual Environment (IMPROVE) network [*Malm et al.,* 1994] provides 24-h average aerosol composition at 20 sites in California. Additionally, there were 10 sites during 2010 that provided measurements of column integrated aerosol optical properties (e.g. aerosol optical depth) as part of the NASA's AErosol RObotic NETwork (AERONET) [*Holben et al*., 1998; *Dubovik et al*., 2002].

A discussion on how the CARES, CalNex, and operational measurements have been merged into a single dataset [*Fast et al.*, 2011] is included in the Supplemental Information and in Fig. S1.

3 Model Description

Version 3.3.1 of the WRF-Chem community model is used in this study to simulate the evolution of aerosols over California. The model configuration is similar to that used for operational meteorological and tracer forecasting during CARES as described by *Fast et al*. [2012], except that trace gas and aerosol chemistry are now included. The specific physical parameterizations used in this study, also available in the public release of the model, are listed in Table 1. We use the SAPRC-99 photochemical mechanism [*Carter*, 2000a,b] to simulate gas-phase chemistry, and the MOSAIC module [*Zaveri et al*., 2008] with 8 size bins to simulate aerosol chemistry, thermodynamics, kinetic gas-particle partitioning for inorganic species, and aerosol dynamics. The simplified 2-product volatility basis set (VBS) parameterization is used to simulate equilibrium SOA partitioning as described in *Shrivastava et al*. [2011], except that the factor of two used to increase primary organic aerosol emissions in that study to obtain better agreement between simulated primary organic aerosol (POA) and estimates of POA derived from AMS data is not employed here.

The model domain encompasses all of California, Nevada, and the adjacent Pacific Ocean using a horizontal grid spacing of 4 km. The domain is identical to the domain used in *Fast et al.* [2012], and extends ~150 km further over the ocean than is shown in Fig. 1. A stretched vertical coordinate that uses 65 grid levels extends up to 16 – 20 km AGL, with a 30-m grid spacing adjacent to the surface and 43 levels located within 2 km of the ground. The simulation period is from May 1 to June 30, 2010. Initial and boundary conditions for the meteorological variables were based on analyses from the National Center for Environmental Prediction's North American Mesoscale (NAM) model, while initial and boundary conditions for trace gases and aerosols were obtained from the global MOZART model [*Emmons et al*., 2010]. Boundary conditions were updated at 6-h intervals from both models and then interpolated linearly in time by WRF. Instead of performing a series of short forecasts, a single simulation was performed over the 2-month period in which four-dimensional meteorological data assimilation was applied above 1.5 km AGL using analyses from the NAM model so that the simulated large-scale flows did not diverge from observed synoptic conditions. A test simulation without data assimilation (not shown) produced similar results, suggesting that the free tropospheric meteorological conditions were largely governed by the lateral boundary conditions.

Anthropogenic emissions were obtained from the CARB 2008 ARCTAS emission inventory developed for the NASA Arctic Research of the Composition of the Troposphere from Aircraft and Satellite (ARCTAS) mission over California [*Pfister et al*., 2011]. The CARB inventory contains hourly emissions for a 13-day period using a 4 km grid spacing over California. We created diurnally-averaged emissions from five of the weekdays and two of the weekend days and used those averages for all weekdays and weekends in the entire two-month simulation period. Anthropogenic emissions from the 2005 National Emissions Inventory (NEI) were used for regions outside of California. Emissions of semi-volatile and intermediate volatility SOA trace gas precursors were assumed to be 6.5 times the mass of primary organic aerosol emissions from anthropogenic and biomass burning sources as in *Shrivastava et al*. [2011] and *Tsimpidi et al*. [2010]. Biogenic emissions were computed on-line using the Model of Emissions of Gases and Aerosols from Nature (MEGAN) model [*Guenther et al*., 2006] and lumped into isoprene, terpenes, and sesquiterpenes for the SAPRC-99 photochemical mechanism. Sea-salt emissions (sodium and chloride) from the ocean were computed online using fluxes based on predicted surface winds and boundary layer quantities as described by *Gong et al*. [2002]. While biomass burning and dust emissions are not considered in the present study, long-range transport of smoke and dust from Asia as represented by MOZART were included through the boundary conditions. Satellite detection methods indicated that there were very few fires in California during this two-month period.

Anthropogenic VOC and biogenic isoprene emission rates over California and in the vicinity of the Los Angeles and Sacramento supersites at 10 Local Standard Time (LST) on a representative day are

shown in Fig. 2. As expected, the highest anthropogenic volatile organic compound (VOC) emission rates are proportional to population density. A portion of the interstate highway system is also evident in the figure, especially in the sparsely populated regions of Nevada and southeastern California. While biogenic emissions occur in most non-desert regions of California, the emission rates are highest along the foothills of the Sierra Nevada that are dominated by oak trees.

Two preliminary simulations (not shown here) were performed that used either the merged CARB 2008 and NEI 2005 inventories or only the NEI 2005 inventory over the entire model domain. While both simulations usually over-predicted CO, NO_x, and black carbon (that largely originate from traffic emissions), concentrations from the simulation that used the CARB 2008 inventory were closer to observations in both southern and northern California (not shown). This is consistent with the decrease in anthropogenic emissions over the past decade in California reported by *Bahadur et al*., [2011] and *CARB* [2009]. Table 2 lists the total daily trace gas and aerosol emissions over the modeling domain for weekday and weekend periods. It is reasonable to assume anthropogenic emissions during 2010 would be less than during 2008, but the exact amount is still under investigation using a variety of methods. A few recent modeling studies have examined how reasonable the 2008 emission inventory is for this region. Using inverse modeling, *Brioude et al*. [2013] developed an improved CO and NO_x emission inventory for the Los Angeles basin to correct for inconsistencies in amounts and spatial distributions found in the CARB emission inventory. To reduce uncertainties in VOC emissions and their speciation, *Knote et al*. [2013] applied measured VOC/CO emission ratios obtained from the Los Angeles basin during CalNex. They found considerable differences (up to a factor of ~10 for some VOC species) in the estimates of VOC emissions as well as OH concentrations between the CARB inventory and the amounts estimated from the measured VOC/CO emission ratios in the Los Angeles basin. These updates have not yet been incorporated in the publically released inventory, and have not been considered in our study.

Until a more refined inventory for 2010 is available, we performed a default simulation, called "DEF_ANT", that employed the merged CARB 2008 and NEI 2005 inventories (Table 2) and two sensitivity simulations, called "50%_ANT" and "0%_ANT" as indicated in Table 3. The two sensitivity simulations reduce the anthropogenic emissions by 50% (except for SO_2 and NH_3) in the former and eliminate them in the latter. Reducing anthropogenic emissions by 50% is a rather large adjustment considering a 2-year trend, but this factor also assumes the CARB 2008 emission estimates may be too high for that time period. *Kozawa et al.* [2014] recently reported similar reductions in NO_x and BC emission estimates based on truck-dominated freeways in Los Angeles from 2009 to 2010. All three simulations include on-line biogenic and sea-salt emissions. The simulation with no anthropogenic emissions is performed to estimate the relative contribution of local emission sources and long-range transport on aerosol concentrations throughout California. One additional sensitivity simulation is

performed, called "50%_LBC" in which aerosols for the initial and boundary conditions obtained from MOZART are reduced by half in addition to reducing the anthropogenic emissions by 50%. As will be shown later, total aerosol mass near the surface is usually not significantly affected by long-range transport, but small aerosol concentrations in the free troposphere transported from Asia are the primary contributor to aerosol optical depth outside of major urban areas.

The four simulations all employ aerosol direct effects [*Fast et al*., 2006], primarily to obtain aerosol optical properties to compare with measurements. The impact of different aerosol loading and distributions among the simulations on radiation and subsequently meteorology is small (not shown); therefore, evaluation of the simulated meteorological quantities is presented only for the DEF_ANT simulation. Aerosol indirect effects, cloud chemistry, and wet scavenging are currently neglected since there were relatively few clouds and little rain over land during the two-month period.

4. Model Evaluation

The AMT software is used to extract variables related to meteorological, trace gas, aerosol, and aerosol optical properties from the four WRF-Chem simulations compatible with most of the measurements collected during CARES and CalNex and perform most of the statistics shown in this section. Bias is expressed in terms of simulated minus observed values. In addition to Root Mean Square Error (RMSE) and correlation coefficient (R), we also use the Index of Agreement (IA) developed by Willmott [1981] that varies between 0 and 1 where 1 indicates a perfect match. While the AMT was originally conceived to test aerosol process modules while all other processes remain the same, the same methodology is used here to assess model sensitivity to emissions and boundary conditions.

Meteorological predictions during CalNex and CARES using the WRF model have been discussed previously by *Angevine et al.* [2012] and *Fast et al.* [2012], respectively. An evaluation of the simulated meteorological quantities not described previously is included in the supplemental information. In summary, the overall simulated diurnal and multi-day variations in meteorological quantities (temperature, humidity, wind speed and direction, boundary layer depth) that affect the evolution of trace gases and aerosols are consistent with a wide range of CARES and CalNex measurements and the model's statistical performance is similar to those from other chemical transport modeling studies. While the near-surface wind speeds are too high, the overall bias in simulated winds aloft is closer to zero and transport processes throughout the troposphere controls the movement of trace gas and aerosol plumes. Nevertheless, relatively small errors in the simulated meteorological quantities can still impact the timing and spatial variability of these plumes as will be shown later.

4.1 Trace gases

As mentioned previously, it is likely that the CARB emission inventory developed for the 2008 ARCTAS field campaign may not be representative for the CalNex and CARES field campaign period in 2010. To demonstrate the sensitivity of the model results to trace gas emission rates, the observed and simulated diurnally-averaged mixing ratios of CO, NO, NO_2, NH_3, SO_2, five volatile organic compounds (VOCs), and ozone at the four supersites are shown in Figs. 3, 4 and 5. Since CO reacts slowly, its spatial and temporal variations can be used to evaluate how well transport and mixing processes are represented by models. Nitrate evolution is controlled by temperature and concentrations of NO, NO_2, and NH_3, while sulfate is produced by oxidation of SO_2. VOCs will influence oxidant chemistry and play a role in SOA formation. Finally, ozone is a useful quantity to examine since it is the byproduct of photochemistry that also impacts aerosol chemistry and high concentrations can adversely affect human health. Ozone has also been shown to be correlated with SOA [*Herndon et al.,* 2008; *Wood et al*., 2010] and the SOA treatment used by the model depends on simulated hydroxyl radical (OH) concentrations [*Shrivastava et al*., 2011].

As seen in Fig. 3a, simulated CO from the 50%_ANT simulation performs better than DEF_ANT at all the supersites. The diurnal and multi-day variations from 50%_ANT at the urban supersites agree reasonably well with observations as shown in Fig S5. Errors in the simulated boundary layer depth cannot account for the large CO mixing ratios simulated by DEF_ANT. At the rural T1 site, the simulated CO from 50%_ANT is still too high. The 0%_ANT simulation shows that there are periods when the background mixing ratios from long-range transport lead to higher than observed CO mixing ratios (June 12-16 and 20-24 in Fig. S5d), suggesting that the global MOZART simulation contributes to these errors over California. In general, the CO from the boundaries may be 20-30 ppb too high on many days. Therefore, errors in simulated CO are due to both uncertainties in the emissions rates and boundary conditions, with the errors associated from boundary conditions relatively more important at rural locations, such as T1, where emission rates are much smaller than in the urban areas.

Uncertainties in the boundary conditions do not likely contribute to the over-predictions of NO and NO_2 in the DEF_ANT simulation, since the mixing ratios from 0%_ANT are very low compared to the observations as shown in Figs. 3b, 3c, S6, and S7. As with CO, NO and NO_2 are in better agreement with observations from the 50%_ANT simulation; however, the simulated mixing ratios are still too high in Pasadena. As shown in Figs. 3d and S8, the observed and simulated diurnal variation in ammonia (NH_3) at Bakersfield are very similar, although simulated mixing ratios are somewhat lower than observed. At the Pasadena site, simulated NH_3 is too high, with peak mixing ratios occurring just before sunrise when the observations have a minimum value. The simulated diurnal variation in NH_3 at Pasadena and Bakersfield are very similar, but the observations at Pasadena exhibit much less diurnal variability. While the observed diurnal variation in HNO_3 is reproduced by the model and the mixing

441 ratios from the 50%_ANT simulation are similar to observed at Bakersfield (Fig. 3e and S9), HNO_3 from
442 all the simulations is too low at the Pasadena site.
443 Model results also indicate that the amount of SO_2 transported from Asia is also very small, as
444 shown by comparison of the observations with the 0%_ANT simulation in Figs. 3f and S10. The diurnal
445 and multi-day variation of SO_2 is simulated reasonably well at the T0 site, although the magnitude is
446 higher than observed at night. The episodic nature of the SO_2 mixing ratios associated with the
447 interacting synoptic and thermally-driven flows [*Fast et al*., 2012] and their impact on sulfate (SO_4^{2-}) in
448 the vicinity of Sacramento will be discussed in Section 4.4. In Bakersfield, the overall magnitude of SO_2
449 simulated is similar to observed but the diurnal variation is not represented well by the model. While the
450 model often has the highest concentration at night after midnight that decreases rapidly with daytime
451 vertical mixing in the boundary layer, the observations indicate an increase in SO_2 mixing ratios around
452 sunrise that do not decrease dramatically during the day. In contrast, the observed and simulated average
453 diurnal variation in SO_2 at Pasadena is similar, but the simulated mixing ratios are far too high suggesting
454 that emissions in this region are likely too high.
455 VOCs, including isoprene, terpene, and methyl-vinyl-ketone + methacrolein (MVK+MACR),
456 toluene and formaldehyde were measured by Proton Transfer Reaction Mass Spectrometer (PTR-MS)
457 instruments [*Lindinger et al.,* 1998] deployed at Pasadena, T0, and T1 and a gas chromatography
458 instrument [*Gentner et al*., 2012] at Bakersfield. Isoprene, terpene, and MVK+MACR originate primarily
459 from biogenic emissions, while toluene and formaldehyde are associated with anthropogenic emissions.
460 We note that *Liu et al*. [2013] recently found that isoprene-derived peroxyl radicals were measured by the
461 PTR-MS at the same mass-to-charge (*m/z*) ratio as MVK and MACR; therefore, the measurements are
462 likely to be higher than reality.
463 The model reproduces the observed diurnal and multi-day variations in isoprene (Figs. 4a and
464 S11) as well as the trend in peak mixing ratios, with the highest mixing ratios at the T1 site, followed by
465 T0, Pasadena, and Bakersfield. However, daytime mixing ratios from DEF_ANT and 50%_ANT are
466 usually a factor of two too low. Simulated terpene at the T0 site is also a factor of two too low as shown
467 in Figs. 4b and S11, but the mixing ratios are closer to observed at night. Conversely, simulated terpene
468 mixing ratios are similar to observations during the day but a factor of three too high at night at the T1
469 site. Figs. 4c and S13 show that simulated MVK+MACR is too low at Pasadena, T0, and the T1 sites
470 throughout the day. These results suggest that there are likely uncertainties in biogenic emission rates
471 obtained from MEGAN. As shown in Guenther et al. (2006) a 1 degree error in simulated temperature
472 could lead to a ~15% error in isoprene emission rate, but the relatively small errors in simulated
473 temperature do not fully explain the under-prediction in isoprene. While MEGAN computes 138 biogenic
474 species, SAPRC-99 (as with any photochemical model) has a limited number of VOC species and

consequently many of the biogenic species computed by MEGAN are lumped together. *Knote et al*. [2013] suggest that there is a deficient description of vegetation in urban areas in the MEGAN land use database, leading to too low biogenic emissions over Los Angeles. In their work with WRF-Chem, they increased emissions of all biogenic VOCs as determined in MEGAN by a factor of 2.5 over grid points with an "urban" land use type in WRF-Chem. Thus, uncertainties in the biogenic trace gases can arise from the species-lumping in SAPRC-99 and from how well vegetation is represented in the model, particularly in the vicinity of the sampling sites. For example, Fig. 2 shows that simulated biogenic emissions vary by a factor of 2 within 8 km of the T1 site. The 0%_ANT simulation also demonstrates that isoprene and terpene mixing ratios are sensitive to anthropogenic emissions rates while MVK+MACR are not very sensitive; therefore, uncertainties in some biogenic species are also affected by uncertainties in anthropogenic emissions. Toluene is emitted by anthropogenic sources, and as with the other primary anthropogenic emissions the 50%_ANT simulation is closer to observed at all four sites as shown in Figs. 4d and S14, except during the night at Bakersfield. As shown in Figs. 4e and S15, afternoon formaldehyde mixing ratios from the DEF_ANT simulation are closer to observations at the four supersites, while the 50%_ANT simulation better represents the mixing ratios at night and several hours after sunrise.

As seen in Figs. 5a and S16, the model captures the diurnal and multi-day variability of ozone. Daytime peak values are well simulated at the T0 and T1 sites, but are too low at the Bakersfield and Pasadena sites. Reducing ozone precursor emissions in the 50%_ANT simulation, increased peak ozone mixing ratios at Pasadena, but reduced daytime ozone concentration at Bakersfield. Statistics describing the performance of the model in simulating ozone at all the surface monitoring sites are given in Tables S15- S17. Ozone from the DEF_ANT simulation is too low overall by 3.9 ppbV in contrast with the results at the Bakersfield and Pasadena sites that are 13 to 15 ppbV too low on average. The overall bias over California from the 50%_ANT simulation is nearly identical to the bias from the DEF_ANT simulation; however, the bias in ozone is improved for the southern California and Sacramento Valley regions. A similar difference between the two simulations is also produced for the sum of NO and NO_2.

Observed and simulated O_x, the sum of O_3 and NO_2, is shown in Fig. 5b because it is often used as an indicator of photochemistry that removes the effect of titration by NO. O_x from the 50%_ANT simulation is in much better agreement with observations at the Pasadena site during much of the day, but is still too low during the afternoon. While Ox from the DEF_ANT simulation is in better agreement with the observations at Bakersfield and Sacramento, we have shown that NO, NO_2, and some of the VOCs in that simulation are too high. Observed and simulated OH is shown in Fig. 5c for the Pasadena site. OH is a useful indicator of daytime photochemistry; however, OH measurements have large uncertainties and the observed nighttime mixing ratios in Fig. 5c were removed since there are much fewer measurements

509 contributing to the diurnal average. Decreasing anthropogenic emissions in the 50% ANT simulation
510 results in higher OH mixing ratios than in DEF_ANT and somewhat higher than observed on average.
511 The impact of OH mixing ratios on simulated SOA formation will be discussed in Section 4.3.
512 Fig. 6 shows the comparison of observed and simulated CO, NO, NO_2, NH_3, HNO_3, SO_2, and O_3
513 distributions in terms of percentiles for all the G-1 flights (as high as ~3.2 km MSL), all the WP-3D
514 flights north of 35^o N (as high as ~6.8 km MSL), all the WP-3D flights south of 35 ^{o} N (as high as ~5.6
515 km MSL), and the entire RV-Atlantis transect in the marine boundary layer. The statistics for the WP-3D
516 aircraft are divided in this way so that the northern transects are more comparable to the G-1 in the
517 vicinity of the Sacramento while the southern transects are expected to have higher mixing ratios
518 associated with the large emissions in the Los Angeles Basin. As with CO, NO, and NO_2 at the
519 supersites, the results from the 50%_ANT simulation are in better agreement with the observations than
520 the DEF_ANT simulation. However, the 50%_ANT simulation still has significantly higher than
521 observed mixing ratios along the RV-Atlantis transects in the marine boundary layer. These over-
522 predictions are likely related to the simulated marine boundary layer depth near the coast of southern
523 California that was often too shallow (as low as 30 m - one vertical model level). In contrast, radiosondes
524 launched from San Nicolas Island indicated that the average depth of the marine boundary layer was ~250
525 m [*Angevine et al*., 2012]. Off-shore profiles made by the WP-3D flight on May 16 indicated a well
526 mixed layer that was ~550 m deep [*Angevine et al*., 2012]; however, the simulated boundary layer depth
527 in that region varied from 300 to 500 m. The largest over-predictions of CO, NO, and NO_2 over the
528 ocean occurred when the ship is in the vicinity of Los Angeles (not shown), suggesting that emissions
529 may also be too high along the coast or that the simulated local circulations transport too much material
530 from the land to the ocean. As with the rural T1 site, background mixing ratios from the global
531 MOZART model may affect CO mixing ratios over the ocean but uncertainties in the boundary
532 conditions are not likely to affect simulated NO and NO_2. The median simulated NH_3 mixing ratios of ~1
533 ppb over northern California are about 2.5 ppb lower than observed (Fig. 6b), which is similar to the
534 average difference between average observed and simulated mixing ratios at the Bakersfield site (Fig. 3d)
535 during most of the day. In contrast with the over-prediction in NH_3 at the Pasadena site (Fig. 3d), the
536 simulated NH_3 aloft over southern California is close to observed (Fig. 6c). HNO_3 mixing ratios from the
537 DEF_ANT and 50%_ANT simulations are somewhat higher and lower, respectively, than observed over
538 both northern and southern California. In addition, the simulated HNO_3 mixing ratios are usually closer
539 to observed than at the Pasadena site (Fig. 3e). Simulated SO_2 is generally too low aloft along all the G-1
540 and WP-3D flights, even though the overall simulated magnitude was similar to that observed at the T0
541 and Bakersfield sites. Observed median SO_2 values are between 0.4 and 0.7 ppb, while the simulated
542 values are between 0.05 and 0.2 ppb. In contrast, the model significantly over predicts SO_2 in the marine

boundary layer along the RV-Atlantis transects. The simulated 75th percentiles are ~5 ppb, but the observed values are ~0.5 ppb. The factors that contribute to the over-prediction in marine boundary layer SO_2 are likely the same as those for NO and NO_2. As with the supersites, the DEF_ANT simulation produces ozone aloft in the vicinity of Sacramento that is similar to observed, but is too low everywhere else. The 50%_ANT simulation decreases ozone aloft, but improves the simulation over the ocean somewhat. The high simulated NO mixing ratios lead to too much ozone titration in the marine boundary layer.

PTR-MS instruments were also deployed on the G-1 [*Shilling et al.,* 2013] and WP-3D [*Warneke et al*., 2011] aircraft; therefore, we also compare the observed and simulated isoprene, terpene, MVK+MACR, toluene, and formaldehyde distributions in Fig. 7. Observed biogenic trace gas mixing ratios from the G-1 are about an order of magnitude higher than those from the WP-3D north of 35^{o} N because a large fraction of the G-1 samples occurred over the forested foothills of the Sierra Nevada (Figs. 1a and 1b). As with the supersites, simulated mixing ratios of biogenic species aloft are too low, although the simulated isoprene along the WP-3D transects in northern California are only somewhat lower than observed. While toluene along the G-1 flights from the DEF_ANT simulation are similar to observed, simulated toluene is somewhat higher than observed along the WP-3D flights over both southern and northern California. Simulated toluene from the 50%_ANT simulation is in better agreement with the WP-3D data, but lower than observed for the G-1 data. As with ozone, formaldehyde from the 50%_ANT simulation is too low and somewhat lower than from the DEF_ANT simulation.

Additional statistics for the same trace gases as in Figs. 6 and 7 are given in Tables 8 and 9 for the G-1 and WP-3D flights, respectively. The biases are similar to the percentile shown previously. As expected, the statistics from the 0%_ANT simulation are usually poor because it neglects anthropogenic emissions. For the simulations that include anthropogenic emissions, the temporal and spatial variations in ozone, CO, and formaldehyde are similar to those observed along the flight paths as indicated by correlation coefficients between 0.6 and 0.8. Somewhat lower correlation coefficients between 0.4 and 0.6 were produced for NO, NO_2, isoprene, and toluene. The lowest correlation coefficients were produced for SO_2, MVK+MACR, and terpene. Statistics quantifying the performance in select trace gases averaged over all the surface monitoring sites in California by region (Fig. 1c) and for the individual supersites are given in Tables S15, S16, and S17 for the DEF_ANT, 50%_ANT, and 0%_ANT simulations, respectively. Model performance varies from day to day based on the simulated meteorological conditions and how well emissions are represented for a particular day. Therefore, additional statistics on the trace gases from the DEF_ANT simulation for the individual G-1 flights are given in Tables S18 – S26 and for the individual WP-3D flights in Tables S26 – S36.

In summary, the simulated anthropogenic trace gases from the 50%_ANT and 50%_LBC simulations that reduced the emission rates in the 2008 CARB inventory were usually closer to the surface and aircraft measurements collected during the CARES and CalNex campaigns. Simulated isoprene and terpene mixing ratios were usually too low at the surface and aloft, except that simulated terpene was too high at night at two surface sites. A number of factors probably contribute to the errors in simulated biogenic species, such as meteorological uncertainties, specification of vegetation types and lumping of VOC species in MEGAN, and errors in simulated anthropogenic emissions that interact biogenic sources as shown by simulation 0%_ANT.

4.2 Carbonaceous aerosols

Single Particle Soot Photometers (SP2) were used to measure black carbon (BC) concentrations at three of the supersites and on three research aircraft. The SP2 measures single-particle refractory BC mass for particles for a discrete size range. *Metcalf et al.* [2012] report a detection range of 80 to 696 nm volume equivalent diameter for the SP2 on the CIRPAS Twin Otter. Therefore, we use the first four size-bins in the model (0.625 μm) to compare BC simulated mass with the SP2 measurements. Both *Metcalf et al*. [2012] and *Langridge et al.* [2012] note that the overall uncertainties on SP2 reported BC mass due to calibration and other factors could be as much as +/-40%. *Laborde et al*. [2012] report that uncertainty in BC mass of +/-10% can be achieved when the SP2 is carefully tuned and calibrated. The detection limits and uncertainty in mass may vary somewhat among the CalNex and CARES SP2 instruments and as a function of time, depending on the size of the peak BC mass distribution, and are not accounted for here.

The time series and diurnal averages of observed and simulated BC at the supersites are shown in Fig. 8. As with CO and NO that are emitted predominately by transportation sources, BC concentrations in the 50%_ANT simulation are closer to observations than in the DEF_ANT simulation where simulated values are usually too high. The model also reproduces much of the diurnal variability of BC, except at the T1 site. While some of the multi-day variations in BC that are associated with the changing meteorological conditions are also reproduced, there are days in which the model performs better than others. Simulated BC from 50%_ANT can be twice as high as observed on some days and it did not produce the occasional peak concentrations that were observed to exceed 1 $\mu g\ m^{-3}$ at the Pasadena site. BC concentrations from the 0%_ANT simulation are occasionally higher than the observations and during the same time periods when background CO concentrations were higher than observed. The background BC concentrations are small, usually less than 0.03 $\mu g\ m^{-3}$; however, this is ~43% of the average observed concentration of 0.07 $\mu g\ m^{-3}$ at the rural T1 site. Reducing background BC concentrations improves simulated BC at the T1 site (not shown), but does not have as large an impact at the Pasadena and T0 sites

since the overall concentrations are higher. These results suggest that long-range transport of BC as simulated by MOZART may be too large. While the uncertainties in background BC will have negligible impact on total $PM_{2.5}$ mass, it does have a significant impact on computed aerosol radiative forcing over most of California as will be discussed in Section 5.

Simulated BC aloft was also compared with SP2 measurements collected along the entire G-1, WP-3D, and CIRPAS Twin Otter aircraft flight paths in terms of percentiles over the sampling period as shown in Fig. 9a. Similar to the surface BC concentrations in Fig. 8 and to simulated CO and NO aloft (Fig. 6), BC concentrations from the 50%_ANT simulation were closer to observations although they are still somewhat higher than observed. Observed and simulated concentrations along the G-1 flight paths and the WP-3D flight paths north of 35^{o} N have similar medians and range of values. Higher concentrations were observed and simulated by the WP-3D and CIRPAS Twin Otter aircraft in the vicinity of the Los Angeles Basin; therefore, the model was able to reproduce the overall characteristics of higher and lower BC concentrations over southern and northern California. The observed and simulated percentiles along the CIRPAS Twin Otter flight paths are also higher than those from the WP-3D since the Twin Otter usually flew in the immediate vicinity of the Los Angeles Basin, while the WP-3D also often flew over the ocean and desert farther from the Los Angeles Basin where BC concentrations were lower. The 50%_LBC simulation produced the best results for all locations. Statistics on BC for individual aircraft flights from the DEF_ANT simulation are given in Table S37.

To demonstrate how well the model represents the spatial and temporal variability of BC, observed and simulated BC for two flights on May 21in the vicinity of Los Angeles are shown in Fig. 10. On this day, the CIRPAS Twin Otter flew over the urban area and through Cajon Pass northeast of Los Angeles, and the WP-3D sampled primarily over the ocean. While observed BC concentrations from the WP-3D close to the ocean surface in the marine boundary layer were usually around 0.02 $\mu g\ m^{-3}$, somewhat higher concentrations between 0.02 and 0.05 $\mu g\ m^{-3}$ were observed ~1 km MSL above the ocean. The model suggests that the higher BC concentrations at 1 km MSL were influenced by local emissions that were transported over the ocean. BC concentrations from the DEF_ANT and 50%_ANT simulations are higher than observed at both altitudes. As with the rural surface sites, the BC concentrations from the 0%_ANT simulation are frequently higher than observed over the ocean. Consequently, simulated BC from 50%_LBC is usually closer to observations than the other simulations. As expected, BC concentrations were an order of magnitude or more higher over the urban areas. BC concentrations measured on the CIRPAS Twin Otter were as high as 0.3 $\mu g\ m^{-3}$. BC from the DEF_ANT simulation was too high except above 2 km MSL, and the 50%_ANT and 50%_LBC simulations were in much better agreement with observed BC. The location and magnitude of the simulated peak BC concentrations were sometimes consistent with the measurements, but the simulated BC concentrations

644 from 50%_ANT and 50%_LBC were still too high between 10.25 and 10.75 and 12.5 and 13 LST. This
645 indicates that there are still uncertainties in simulated thermally-driven circulations, boundary layer
646 turbulent mixing, and/or emissions over the Los Angeles Basin that affect local variations in BC.
647 May 24 is another day in which both the WP-3D and CIRPAS Twin Otter flew over southern
648 California; however, the WP-3D sampled primarily over the southern San Joaquin Valley as shown in
649 Fig. 11. These flights enable the model to be evaluated over a larger geographic area. As the WP-3D
650 flew across the San Joaquin Valley, higher BC concentrations were observed over the eastern side of the
651 valley that contribute to peak concentrations of 0.04 μg m^{-3} between 16.5 and 20.5 LST. The model does
652 not produce the strong gradient across the valley during the aircraft sampling period. The simulated BC at
653 ~1 km AGL in the right panel of Fig. 11 shows that at 14 LST, just prior to the WP-3D flight, higher
654 concentrations are simulated along the eastern side of the valley consistent with measurements. Higher
655 concentrations of BC originating from the Bay Area are transported into the San Joaquin Valley, reducing
656 the simulated variability of BC in the valley after 16 LST. Thus, transport errors in the model contributed
657 to the differences between the observed and simulated variability in BC along the WP-3D flight path.
658 The agreement between the observed and simulated BC concentrations is much better in the vicinity of
659 Los Angeles at all altitudes. The simulated variability in BC concentrations from the 50%_ANT and
660 50%_LBC simulation are nearly identical to observations, although the simulated concentration are
661 somewhat higher than observed.
662 In contrast to the CARES and CalNex data, somewhat different statistics are obtained when
663 comparing the simulations to the daily-averaged BC measurements at the remote IMPROVE site as
664 shown in Table 10. For this dataset, correlation coefficients that were greater than 0.64 represent the
665 model's ability to replicate the multi-day variations rather than the diurnal variations. The bias in BC
666 from the DEF_ANT and 50%_ANT simulations was 0.02 and -0.02 μg m^{-3}, respectively. When the
667 boundary conditions of BC are reduced in the 50%_LBC simulation, the biases increased to -0.04 μg m^{-3}.
668 Based on this dataset, the bias could be due to local anthropogenic emissions, boundary conditions, or a
669 combination of both. In contrast with the evaluations using CARES and CalNex data, the 50%_LBC
670 simulation performed worse. If the field campaign observations were unavailable, it is possible to
671 conclude that reducing the CARB emissions by 25% would produce BC concentrations closer to the
672 observations. Part of the reason for the different BC statistics between IMPROVE and SP2 data sets are
673 likely due to measurement technique; the IMPROVE method could have interference from organic carbon
674 [e.g. *Lack et al*., 2014] that erroneously increases reported BC concentrations. The differences in
675 statistics stress the importance of modeling studies to not rely solely on routine monitoring measurements.
676 As shown by *Hayes et al*. [2013], *Hersey et al.* [2013], *Liu et al*. [2012], *Setyan et al.* [2012], and
677 *Shilling et al*. [2013], organic aerosol (OA) is the largest fraction of total non-refractory aerosols observed

during CARES and CalNex. The time series and diurnally averaged OA obtained from High-Resolution Time-of-Flight Aerosol Mass Spectrometers (AMS) deployed at each of the supersites are shown in Fig. 12 along with simulated OA. Since the AMS measures submicron aerosol mass [*Canagaratna et al.,* 2007], OA from the first four model aerosol size bins up to 0.625 μm diameter are used to compute OA comparable to the measurements. While there will be some uncertainty in the comparison due to the exact cut-off of the AMS measurements (which may vary among the four instruments), simulated OA in the fifth size bin (0.625 – 1.25 μm) is usually small and does not contribute significant mass, as will be shown later (Fig. 22a). Uncertainties in the aerosol mass from the AMS instruments vary but typical errors have been reported to be up to about 30% [*Bahreini et al*., 2009; *Canagaratna et al*., 2007; *Middlebrook et al.*, 2012]. Detection limits depend on the averaging time period. For the AMS at the T1 site, the 2.5-min detection limits were reported to be 0.075, 0.011, 0.018, and 0.01 μg m^{-3} for OA, SO_4^{2-}, nitrate (NO_3^-), and ammonium (NH_4^+), respectively [*Setyan et al*., 2012]. For the AMS on the G-1 aircraft, the 13-s detection limits of 0.3, 0.07, 0.05, and 0.15 μg m^{-3} for OA, SO_4^{2-}, NO_3^-, and NH_4^+, respectively [*Shilling et al*., 2013], were higher because of the much shorter sampling period needed for aircraft operations. The detection limit for OA from the AMS on the CIRPAS Twin Otter aircraft was reported to vary between 0.141 to 0.382 μg m^{-3}, depending on the flight [*Craven et al.,* 2013] and is similar to the G-1. Observed and simulated composition concentrations are usually well above AMS detection limits, and thus the limits do not affect the model evaluation significantly.

At the Pasadena site, observed peak concentrations of OA exceeded 10 μg m^{-3} on several days; however, simulated OA concentration in from all the simulations were too low and usually less than 5 μg m^{-3} (Fig. 12). OA concentrations from the DEF_ANT simulation are closer to observations at the Bakersfield, T0, and T1 sites, with the model reproducing much of the observed multi-day and diurnal variability. At these sites, OA from the 50%_ANT and 50%_LBC simulations are lower than observed and 1 – 1.5 μg m^{-3} lower than those from the DEF_ANT simulation. The 0%_ANT simulation shows that boundary condition OA is a small fraction of the total OA at the Pasadena site, so that OA is dominated by local sources. While OA from the 0%_ANT simulation is still small at the other sites, it is not an insignificant fraction of the total OA. The relatively higher OA from this simulation is not from long-range transport, but associated with biogenic SOA since the biogenic precursor emissions are larger at these sites and particularly for T1. As described in *Fast et al*. [2012] and *Setyan et al.* [2012], the meteorological conditions after June 20 are more favorable for SOA formation, which is consistent with the increase in biogenic SOA from the 0%_ANT simulation during this time period.

Since OA is composed of primary and secondary material, we use the results of Positive Matrix Factorization (PMF) analyses that have been applied to the AMS data from the Pasadena [*Hayes et al.,*

711 2013], Bakersfield [*Liu et al.,* 2012], T0, and T1 [*Setyan et al*., 2012] datasets to provide estimates of
712 observed POA and SOA. To assess the model sensitivity to emissions, a direct comparison of observed
713 and simulated POA is more appropriate than relying on OA alone. Fig. 13 compares the diurnally
714 averaged simulated POA and SOA with estimates derived from PMF. At the Pasadena site (Fig. 13a), the
715 overall magnitude of POA from the DEF_ANT simulation is similar to the PMF estimate, except that the
716 model is up to 1 μg m^{-3} too high at midnight and up to 1 μg m^{-3} too low during the afternoon. The
717 DEF_ANT simulation also produces a diurnal average that is similar to the PMF estimate at the T0 site
718 (Fig. 13b), except that simulated POA is up to 0.5 μg m^{-3} too low during the afternoon. For both
719 Pasadena and the T0 site, POA from 50%_ANT is lower as expected and is lower than the PMF estimate.
720 At the Bakersfield and T1 sites (Fig. 13c and 13d), however, the 50%_ANT simulation produces a diurnal
721 average that is nearly identical to the PMF estimate while the POA from the DEF_ANT simulation is too
722 high all day. These results suggest that POA emission rates from the CARB emission may be reasonable,
723 at least in the highly populated areas. The over-prediction in POA from the DEF_ANT simulation at the
724 rural T1 site could be due to the horizontal resolution. As seen in Fig. 2, the city of Auburn is located just
725 northwest of T1 and the 4 km grid spacing, which is the same resolution as the 2008 CARB emission
726 inventory, likely results in numerical smoothing of anthropogenic plumes to the adjacent model grid cell
727 over the T1 site. The spatial resolution of the emission inventory could also be an issue at the Bakersfield
728 site since it is located at the edge of the city [*Alm et al*., 2012].
729 Fig 13a shows that the large under-prediction in OA at Pasadena for both the DEF_ANT and
730 50%_ANT simulations is due primarily to simulated SOA that is too low. The model does produce more
731 SOA during the day similar to the observed increase during the late morning and afternoon, but the
732 formation rate is far too low. The uncertainties in POA emissions are far less than those associated with
733 SOA, so that changing the POA emissions is unlikely to solve the under-prediction in SOA for the current
734 volatility basis set approach to SOA unless POA is increased to unrealistic levels compared with PMF
735 estimates. As shown in Fig. 5c, simulated OH is too high in the DEF_ANT simulation. Since SOA
736 formation rate in the VBS approach depends on OH, the over-prediction in OH would suggest that
737 simulated SOA should be too high. The results indicate that SOA formation processes from
738 anthropogenic sources are missing or not represented adequately at this urban site. In contrast, simulated
739 SOA is closer to the PMF estimates at the other sites (Figs. 13b – 13d). *Setyan et al.* [2012] show that a
740 large fraction of SOA at the T1 site originates from biogenic sources. However, the 0%_ANT simulation
741 that includes only biogenic SOA produces less than 0.5 μg m^{-3} on average at T1, suggesting that most of
742 the simulated SOA is from anthropogenic sources. Since POA in the DEF_ANT simulation is too high
743 and biogenic SOA is a small fraction of the total SOA, the model is likely producing the correct
744 magnitude in SOA for the wrong reasons at the T1 site. It appears that uncertainties associated with

anthropogenic semi-volatile and intermediate volatility precursor emissions that are poorly constrained and yields of multigenerational biogenic chemistry are cancelling each other out to some extent. In addition, semi-volatile and intermediate VOCs form SOA rapidly in the current VBS approach, whereas light aromatics (e.g. toluene) will make SOA continuously over several days. Multi-generational chemistry for aromatics is currently ignored; however, *Hodzic et al.* [2013] use an explicit model to show that this process could be important at regional scales over several days of chemical processing.

Simulated OA aloft was also compared with AMS measurements collected by the G-1, WP-3D, and CIRPAS Twin Otter aircraft in terms of percentiles over the sampling period as shown in Fig. 9b. The observed OA concentrations from the G-1 are higher than those from the WP-3D since the highest OA concentrations occurred during the last few days of June and the last WP-3D flight north of 35^{o} N was on the June 18. As with the T0 and T1 sites, OA concentrations from the DEF_ANT simulation were closer to observations over northern California than the other simulations. While OA from the DEF_ANT simulation was very similar to observations from the WP-3D south of 35 ^{o} N, that simulation produced higher than observed concentrations along the CIRPAS Twin Otter paths. The variations in OA concentrations from the 50%_ANT simulation were also closer to Twin Otter observations. Note that the flight days and sampling period for the WP-3D (May 4 – June 22) and Twin Otter flights (May 6 – 28) are not identical, so that observed and simulated percentiles for these two data sets are likely to be different. Nevertheless, these results aloft are substantially different than the under-predictions of OA at the Pasadena site. Statistics on OA for individual aircraft flights from the DEF_ANT simulation are given in Table S38.

To further illustrate the uncertainties in OA predictions, Fig. 14 compares the observed and simulated OA and CO from the G-1 flights on June 28 and June 12. The afternoon G-1 flight on June 28 had the highest OA observed during CARES, while June 12 had low OA concentrations as a result of strong northwesterly winds associated with an upper-level trough [*Fast et al*., 2012]. The simulated CO along the flight path on June 28 is similar to observations downwind of Sacramento, except that the peak concentrations in center of the plume (points A and B in Fig. 14a) are too low. While the simulated southwesterly up-slope winds are simulated reasonably well as described in *Fast et al*. [2012], the simulated BL depth during the afternoon of June 28 was 61% higher than observed at 13 LST and 25% higher than observed at 16 LST, leading to excessive dilution within the model. The spatial variation in simulated OA is similar to CO, indicating that simulated SOA is influenced or controlled by anthropogenic sources; however, the concentrations from both DEF_ANT and 50%_ANT are much lower than the AMS measurements. Peak values from DEF_ANT are ~7 μg m^{-3}, while observations are as high as 25 μg m^{-3}. In addition to too much dilution, two other factors likely account for the under-prediction in OA. First, the regional OA background concentrations transported into the Sacramento region are too

779 low, even though background concentrations of CO are close to observed. Second, the model likely
780 under-estimates enhanced SOA production resulting from anthropogenic emissions mixing with biogenic
781 SOA precursors as described in *Setyan et al*. [2012] and *Shilling et al.* [2013].
782 Similar to the G-1 measurements, lower OA concentrations are simulated during the afternoon of
783 June 12 than on other days. The simulated concentrations are usually less than 1 μg m^{-3} while the
784 observed concentrations are between 2 and 3 μg m^{-3} (Fig. 14b). The model also fails to capture the spatial
785 variability in OA and CO on this day. The bottom panel of Fig. 14b shows that highest concentrations of
786 observed OA are located on the eastern side of the valley, but the model produced peak concentrations
787 over the western side of the valley. The spatial pattern in simulated CO is similar to OA (not shown).
788 While the simulated wind speed and direction at the Sacramento radar wind profiler ~1 km AGL was very
789 similar to the observations (Fig. S4a), the simulated winds along the G-1 flight path were northerly along
790 the foothills of the Sierra Nevada and the observations were northwesterly. Table S3 and S4 show that
791 the performance in simulated winds along the G-1 flight path was reasonable during the morning of June
792 12 but decreased significantly during the afternoon. While transport errors likely accounts for all of the
793 errors in simulated CO, they cannot explain the bias in simulated OA. The production of SOA is likely
794 too low on this day as well.
795 In contrast, the spatial distributions of OA were usually simulated better in the vicinity of the Los
796 Angeles Basin. Examples are shown in Fig. 15 for WP-3D flights on June 20 and 3 that had relatively
797 higher and lower peak OA concentrations, respectively. On both days, the model reproduced the spatial
798 variability in both CO and OA reasonably well. The correlation coefficients for OA on June 20 and 3
799 were 0.83 and 0.7, respectively. The peak concentrations in OA from the DEF_ANT and 50%_LBC
800 simulations were 5 and 3 μg m^{-3}, respectively, for both days while the observed peak values were between
801 7 and 10 μg m^{-3}. OA concentrations from both simulations were much closer to observed on June 3, with
802 the DEF_ANT simulated OA somewhat higher than observed and 50%_ANT simulated OA somewhat
803 lower than observed.
804 In general, BC from the 50%_ANT simulation was much closer to most surface and aircraft
805 measurements than the simulation that used the default emission inventory. Simulated BC was also
806 somewhat further improved in the 50%_LBC simulation in remote regions where a relatively higher
807 fraction to the total aerosol mass is influenced by boundary conditions provided by the global model. In
808 contrast, OM simulated by the DEF_ANT simulation was usually closer to observations than the other
809 simulations but the statistics show that performance varies significantly over California. Simulated POA
810 from the DEF_ANT simulation was also closer to POA derived from AMS measurements at the Pasadena
811 and T0 site, but the 50%_ANT simulation POA was closer to the derived POA at the Bakersfield and T1

812 sites. While uncertainties in POA emissions contribute to errors in simulated OM, the largest source of
813 uncertainty in simulated OM is the treatment of SOA.
814
815 **4.3 Inorganic aerosols**
816 The time series and average diurnal variation of SO_4^{2-} obtained from the AMS instruments at the
817 four supersites along with the simulated values are shown in Fig. 16. SO_4 concentrations from the
818 DEF_ANT and 50%_ANT simulations at the Pasadena site are about a factor of two too low on average
819 and the simulated diurnal variability is weaker than observed. The simulated multi-day variations are
820 qualitatively similar to observed with higher concentrations between May 15 and 20 and between May 31
821 and June 8. While the average SO_4^{2-} concentrations from the DEF_ANT and 50%_ANT simulations are
822 similar to observations at the Bakersfield site, the model fails to capture peak concentrations frequently
823 observed during the late afternoon. In contrast, the simulated diurnal and multi-day variability is
824 predicted reasonably well by the model at the T0 and T1 sites, but the concentrations from the DEF_ANT
825 and 50%_ANT simulation are up to 50% too high. While SO_2 emissions were the same in the DEF_ANT
826 and 50%_ANT simulations, differences in photochemistry altered the formation rate of SO_4^{2-}. SO_4^{2-}
827 concentrations of ~0.5 μg m^{-3} were produced by the 0%_ANT simulation at all four sites. Concentrations
828 as high as 3 μg m^{-3} were produced in Pasadena between May 31 and June 8, suggesting that that the
829 overall increase in SO_4^{2-} during that period was associated with sources outside of the domain. In fact,
830 the magnitude and multi-day variability of SO_4 from the 0%_ANT simulation were close to observed,
831 suggesting that local emissions of SO_2 do not significantly contribute to SO_4^{2-} production in the vicinity
832 of Sacramento during June. However, this does not seem plausible since there are large emissions of SO_2
833 upwind of Sacramento in the Carqueniz Strait and intrusions of marine air transports SO_4^{2-} produced by
834 these emissions towards Sacramento [*Fast et al*., 2012; *Setyan et al*., 2012; *Zaveri et al*., 2012].
835 Decreasing the boundary conditions of aerosols from MOZART for the 50%_LBC simulation results in
836 SO_4^{2-} concentrations that are close to observed most times of the day.
837 An example of the impact of the marine intrusions on the formation and transport of SO_4^{2-} from
838 the Bay Area to the T1 site on June 26 is shown in Fig. 17. On this day, the observed and simulated near-
839 surface winds are southwesterly (up-slope) throughout the late morning and afternoon (10 – 18 LST),
840 although the observations are more variable than simulated. Simulated SO_4^{2-} from the 50%_LBC
841 simulation is very similar to observed, with concentrations increasing from 0.4 to 1.0 μg m^{-3} between 8
842 and 14 LST. The contour plots of simulated SO_4^{2-} distributions over central California at 5, 9, and 14
843 LST also show a trajectory of the mean winds originating at the oil refinery source at 5 LST. By 9 LST, a
844 plume of SO_4^{2-} is produced downwind of the oil refinery that has been transported more than halfway
845 towards the T1 site. The model also indicates that SO_4^{2-} is formed locally in the vicinity of the T1 site as

a result of photochemistry acting on previous days emissions. By 14 LST, the air mass from the oil refinery reached the T1 site at the same time as the observed peak concentrations. The highest SO_4^{2-} concentrations, up to 1.5 μg m^{-3}, are produced south of Sacramento because of the spatial and temporal variations in the thermally-driven winds during the day that spread the plume along the foothills of the Sierra Nevada. A time series of simulated SO_2 and SO_4^{2-} along the air mass trajectory indicates that as SO_4^{2-} is gradually produced along the trajectory. SO_2 decreases as a result of both photochemistry and mixing in the growing convective boundary layer. Peak concentrations of SO_4^{2-} are actually produced at 12 LST over Sacramento as vertical mixing rates after that time exceed photochemical production during the late afternoon. The model therefore suggests that the increase in SO_4^{2-} at the T1 site is due to both local photochemistry of aged emissions and same-day transport from the Bay Area superimposed on a background concentration that decreases slightly during the day (not shown).

The observed and simulated NO_3^- at the four supersites is shown in Fig. 18. Pasadena had the highest observed NO_3^-, with concentrations up to 20 μg m^{-3} on two days and concentrations exceeding 5 μg m^{-3} on many days. Daily peak concentrations were usually less than 3 μg m^{-3} at Bakersfield, although concentrations were as high as 7.5 μg m^{-3} on one day. At the T0 and T1 sites, NO_3^- concentrations were much lower, usually less than 0.3 μg m^{-3} so that it comprised only a minor fraction of the total aerosol mass. In contrast with the poor simulation of SO_4^{2-}, the magnitude and temporal variability in NO_3^- is predicted reasonably well at the Pasadena site. Decreasing anthropogenic precursor emissions in the 50%_ANT simulation increases the concentration of NO_3^- somewhat to be closer to observed, but both the DEF_ANT and 50%_ANT underestimate the daily peak concentrations on many days. The performance in simulated NO_3^- at the Bakersfield site is not as good as at the Pasadena site. While the observed and simulated peak concentrations both occur around sunrise, the simulated NO_3^- falls to near zero by the late afternoon and the rate of increase at night is lower than observed. The AMS measurements at the T0 and T1 sites indicate the presence of low concentrations at all times; however, the simulated NO_3^- is nearly zero except for short periods of time in June in which NO_3^- concentrations are as high as 1 μg m^{-3}. The low observed NO_3^- concentrations that do not exhibit significant diurnal variations coupled with the known transport patterns suggest a regional background of NO_3^- that the model does not reproduce. Given the lack of HNO_3 or NH_3 measurements at these sites, it is difficult to determine the reason for the under-predictions; however, comparisons with the WP-3D measurements (Fig. 6b) suggest that NH_3 emissions over northern California are likely too low that could also impact NO_3^- production.

Figure 19 depicts the performance in simulated NH_4^+ at the four supersites. While the instantaneous data from the T0 AMS is noisy, the average values are similar to those at the T1 site; therefore, the data are included for completeness. As with SO_4^{2-}, reducing anthropogenic emissions in the 50%_ANT simulation leads to lower NH_4^+ at all sites. The overall performance in simulated NH_4^+ at the

Pasadena site is very similar to NO_3^- in that much of the diurnal and multi-day variability is captured by the model, although the concentrations are a factor of two too low on average. At the Bakersfield site, the model produces an average diurnal variation similar to observed with the peak concentration of NH_4^+ around sunrise as observed, but the daily peak concentrations are better simulated in May than during June. The performance of the model is best at the T1 site; however, the simulated NH_4^+ concentrations from the DEF_ANT and 50%_ANT simulations are somewhat too high. Similar to SO_4^{2-} at this site, reducing the boundary conditions of aerosols also lower NH_4^+. The average reduction in NH_4^+ is ~0.08 $\mu g\ m^{-3}$ even though the background concentrations from the 0%_ANT simulation are 0.03 $\mu g\ m^{-3}$ or less. This indicates that reduction in NH_4^+ is due primarily to the reduction of pre-existing aerosols that ammonia can condense upon, rather than reducing NH_4^+ from the boundaries.

As with OA, we also compared the simulated SO_4^{2-}, NO_3^-, and NH_4^+ with the AMS measurements collected on the G-1, WP-3D, and CIRPAS Twin Otter aircraft in terms of percentiles as shown in Fig. 20. In contrast with over-predictions in SO_4^{2-} from DEF_ANT and 50%_ANT simulation at the T0 and T1 sites, the overall median and range of SO_4^{2-} simulated aloft is similar to the G-1 measurements. Even though the average concentrations from the 50%_LBC simulation were very similar to observed at the T0 and T1 sites, reducing the boundary conditions of aerosols leads to simulated SO_4^{2-} aloft that is 50% lower than observed. A similar trend in the SO_4^{2-} percentiles among the simulations was produced along the WP-3D flights north of 35^o N, except that the overall concentrations from the DEF_ANT and 50%_ANT simulations concentrations are lower than observed. The simulated SO_4^{2-} from the DEF_ANT, 50%_ANT and 50%_LBC simulations are higher over southern California than over northern California, similar to the aircraft observations. While the simulated SO_4^{2-} is lower than observed along the WP-3D flight paths, the DEF_ANT and 50%_ANT simulation are higher than observed along the CIRPAS Twin Otter flight paths. The overall concentrations from the 50%_LBC simulation are closest to the CIRPAS Twin Otter measurements. As with the AMS measurements, the simulated NO_3^- and NH_4^+ are much lower over northern California than over southern California. The DEF_ANT simulation produced NO_3^- concentrations closer to observed over southern California and NH_4^+ concentrations were comparable to the CIRPAS Twin Otter measurements. In contrast, the simulated NH_4^+ from the 50%_LBC simulation is closest to the WP-3D measurements. Additional statistics for all of the aircraft flights are shown in Tables 11 – 13 and statistics from the DEF_ANT simulation for individual flights are given in Tables S39 – S41. The spatial and temporal variations as reflected by the correlation coefficient and index of agreement are in general the best for OA, followed by BC, SO_4^{2-}, NH_4^+, and NO_3^-.

In summary, the model is able to simulate much of the diurnal and multi-day variability of the inorganic aerosol concentrations. Simulated SO_4^{2-} concentrations were too low at Pasadena and Bakersfield, but much closer to observations at the northern California surface sites and along most of the

914 CARES and CalNex aircraft flight paths. NO_3^- concentrations from all the simulations were generally too
915 low, except along the CIRPAS Twin Otter flight paths. In general, SO_4^{2-} is better simulated in northern
916 California and NO_3^- is better simulated in southern California. While the statistical performance for all
917 the simulations is similar at most locations, the DEF_ANT simulation produced inorganic aerosol
918 concentrations that were somewhat closer to observations..
919
920 **4.4 Aerosol Mass, Volume, and Size Distribution**
921 Table 14 presents statistics that quantify the performance in simulated total $PM_{2.5}$ mass at all the
922 available operational monitoring sites shown in Fig. 1d. The simulated $PM_{2.5}$ mass from the DEF_ANT
923 simulation is too low in general except over the Sacramento Valley, with the largest average bias of -4.5
924 $\mu g\ m^{-3}$ over southern California which is ~38% lower than the observed mean concentration of 11.8 $\mu g\ m^{-3}$.
925 Reducing the primary emissions by 50% leads to larger biases in the 50%_ANT simulation, with biases
926 ranging from -1.3 $\mu g\ m^{-3}$ (27% lower than observed) over the Sacramento Valley to -6.8 (58% lower than
927 observed) over southern California. The temporal variability in $PM_{2.5}$ is also better simulated in some
928 regions of California than others. For example, relatively higher correlation coefficients of 0.48 and 0.44
929 were obtained for southern California stations where the biases were the greatest for both the DEF_ANT
930 and 50%_ANT simulations, respectively. The lowest correlation coefficients of 0.09 and 0.16 from the
931 DEF_ANT simulation were produced for the Coastal and Interior Mountain regions, respectively that are
932 the stations that are least influenced by local anthropogenic emissions.
933 In addition to total aerosol mass, it is also important to adequately simulate the aerosol size
934 distribution to show that the model represents the total aerosol mass for the right reasons. Accurately
935 representing the aerosol size distribution also affects aerosol radiative forcing and the ability of aerosols
936 to serve as CCN. The T0 and T1 sites had measurements from Scanning Mobility Particle Sizer (SMPS)
937 and Aerodynamic Particle Sizer (APS) instruments that were used to evaluate the simulated number and
938 volume size distributions in terms of percentiles as shown in Fig. 21. The SMPS measures number as a
939 function of mobility diameter that is similar to geometric diameter used by the model. The APS measures
940 number as a function of aerodynamic diameter; therefore, the observed values have been adjusted to
941 geometric diameter [*Baron and Willeke*, 2001] using a density of 2.36 g m^{-3} based on 20% SO_4^{2-} (1.8 g
942 cm^{-3}), 20% sea salt (2.2 g cm^{-3}), and 60% other inorganics (2.6 g cm^{-3}). Note that some uncertainty is
943 introduced here since the actual composition of aerosols > 1 μm was not measured and composition will
944 likely vary in time [*DeCarlo et al.*, 2004]. The results from the 50%_LBC simulation are shown since it
945 better represented the observed composition, except for OA, than the other simulations. The gray shading
946 in Fig. 21 denotes the size range of the eight size bins employed by the MOSAIC aerosol model. The
947 average number distributions (Figs. 21a,b) at both sites are lower than observed for bin 1 (0.039 - 0.078

μm), higher than observed for bins 2 and 3 (0.078 - 0.313 μm), similar to observed for bins 4-6 (0.313 – 2.5 μm), and lower than observed for bin 7 (2.5 - 5 μm). The corresponding volume distributions have similar biases as expected (Figs. 21c,d).

The simulated aerosol composition distribution is also compared with the AMS distribution at the T1 site [*Setyan et al*., 2012] and is shown in Fig. 22. While the largest OA mass is observed and simulated in the size range of bin 3 (0.156 - 0.313 μm) in the model (Fig. 22a), the simulated distribution is narrower than observed so that the mass is too low in bins 1 - 2 (0.039 - 0.156 μm) and 4 (0.313 - 0.625 μm). As described in *Setyan et al*. [2012], SO_4^{2-} had a bimodal mass distribution with peak values around 0.4 μm. Although the simulated SO_4^{2-} in bin 4 (0.313 - 0.625 μm) was close to the observed mean value, peak concentrations from the model (Fig. 22b) occurred in bin 3 (0.156 - 0.313 μm). Simulated concentrations were also too low in bins 1 – 2 (0.039 - 0.156 μm), and 5 (0.625 – 1.25 μm). As shown previously in Fig. 18 the simulated NO_3^- (< 1.25 μm) is usually too low at the T1 site; however, the model does produce more NO_3^- mass in bins 5 – 7 (0.625 - 5 μm) as shown in Fig. 22c. The shape of the simulated SO_4^{2-} and NH_4^+ mass distributions are similar to one another, as are the shape of the observed SO_4^{2-} and NH_4^+ distributions (Fig. 22d). In contrast with simulated SO_4^{2-}, the simulated NH_4^+ concentrations in bins 3 (0.156 - 0.313 μm) and 5 (0.625 – 1.25 μm) are similar to observed while concentrations in bins 1 – 2 (0.039 - 0.156 μm) and 4 are too low (0.313 - 0.625 μm).

Composition distributions are also shown in Figs. 22e,f as a percent of the total mass for the observed and simulated distributions, respectively. For the simulated composition distribution, BC, sea-salt (NaCl), and other inorganic material (OIN) are shown since they comprise a significant fraction of the total mass. While the T1 site is located ~200 km from the ocean, *Laskin et al*. [2012] provided evidence of chloride depletion in aged sea salt particles sampled along the G-1 flight paths using scanning electron microscopy, scanning transmission X-ray microscopy, and near edge X-ray absorption fine structure spectroscopy techniques. *Moffet et al*. [2013] employ similar microscopy techniques using particles collected at the T0 and T1 sites to show that dust and sea-salt particles were more prevalent at coarser sizes on June 27 and 28. Comparing Fig. 22f with Fig. 21d suggests that simulated coarse mode NaCl and OIN concentrations are too high. Some of the simulated OIN results from long-range transport of dust in the MOZART model, as will be shown in the next section. Simulated sub-micron NaCl and OIN comprise 20- 40% (depending on size) of the total mass at the T1 site. This fraction is much higher than observed at the Pasadena site [*Hayes et al*., 2013], but measurements from the PALMS instrument at the T1 site are not yet available for comparison.

An evaluation of both the fine and coarse aerosol components at the Pasadena site using the available measurements is shown in Fig. 23. The observations suggest that the simulated $PM_{2.5}$ OIN is

roughly twice as high as observed during CalNex. In contrast, simulated sea-salt concentrations are similar to observed for $PM_{2.5} - PM_1$ and are also a much larger fraction of the total mass compared to PM_1. The large amount of simulated sum of OA + SO_4^{2-} + NO_3^- for $PM_{2.5} - PM_1$ is due mostly to NO_3^-. The average simulated PM_1 $NO3^-$ is too low while the simulated PM2.5 – PM1.25 is too high, suggesting that the size distribution is skewed towards the coarser sizes, similar to the T1 site (Fig. 22c).

Additional analyses of the SP2 and single particle measurements are needed to provide more quantitative information to assess the simulated mass and size distributions associated with BC, NaCl, and OIN. Size distribution measurements using different instruments were also collected at other surface sites and on two research aircraft, but additional evaluation of simulated size distributions will be performed later after information from all the SP2 and single particle instruments are available.

5. Extinction profiles, AOT, and AOD

We have also compared the simulated extinction profiles with the observed profiles obtained from the HSRL-1 on the B-200 aircraft during the CARES and CalNex campaigns to infer how well the model represents profiles of aerosol mass that are not necessarily sampled by the in-situ measurements on the other research aircraft. The aerosol optical depth (AOD) is the vertically integrated extinction throughout the entire atmospheric column usually obtained from AERONET and satellite measurements. In contrast, the aerosol optical thickness (AOT) is the vertically integrated extinction over a discrete layer. For CARES and CalNex, AOT from the HSRL was obtained from the ground to the aircraft sampling altitude which was ~9 km MSL.

As an example, the observed and simulated extinction for the B-200 flight on May 25 over southern California is shown in Fig. 24. The highest extinction was observed in the convective boundary layer (below 1.4 km MSL in Figs. 24a,d) over the Los Angeles basin where the emissions are the highest. Extinction from the DEF_ANT simulation is also highest in the convective boundary layer, but the magnitude is 1.5 – 2 times lower than observed on average. This is consistent with the underprediction in aerosol mass at the Pasadena site (e.g. Fig. 23); nevertheless, simulated aerosol mass aloft was closer to observed along the WP-3D and CIRPAS Twin Otter flight paths. When the effect of long-range transport is reduced in the 50%_LBC simulation, the simulated extinction in the free troposphere is much closer to observed but the aerosol mass and extinction in the convective boundary layer is further reduced as well (Figs. 24b,d). Even though the boundary layer extinction is under-estimated, the simulated AOT from DEF_ANT is higher than observed by about a factor of 2 (Fig. 24e) because of over-predictions in the vertically integrated extinction in the free troposphere. Similarly, the AOT from the 0%_ANT simulation is higher than observed which does not seem reasonable and also suggests the background aerosol

concentrations from MOZART are too high. The AOT from the 50%_LBC simulation is the closest to observed outside of the Los Angeles Basin where the emission rates are relatively low.

Another example in the vicinity of Sacramento during CARES on June 27 is shown in Fig. 25. As expected, the highest extinction was observed in the convective boundary layer within 1km MSL; however, the lidar also detected a layer of aerosols between 1.5 and 3.5 km MSL above the boundary layer (Fig. 25a). Extinction from the DEF_ANT simulation was similar to observed in the free troposphere and somewhat lower than observed in the convective boundary layer (Figs. 25b,d). This is consistent with predictions of aerosol mass, particularly OA, that are too low along the G-1 flight paths. The model qualitatively captured the vertical structure of aerosols in the convective boundary layer and the layer aloft. Similar to the layer described in *Fast et al*. [2012], daytime upslope flows transport trace gases and aerosols from the valley over the Sierra Nevada that are subsequently transported back over the valley at night. The 0%_ANT simulation produced no such layer aloft (Fig. 25d), indicating that the layer is produced by local emissions and not long-range transport. As with the previous case in southern California, simulated extinction above 3.5 km was higher than observed. Reducing aerosols from long-range transport in the 50%_LBC simulation improved the extinction above 3.5 km MSL, but also led to extinctions being lower than observed below 3.5 km MSL (Figs. 25c,d). As with Fig. 24, AOT from the DEF_ANT simulation is too high compared to the lidar AOT. The 50%_LBC simulation produces AOT that is closer to observed outside of the anthropogenic plumes, but is too low where extinction in the convective boundary layer was observed to be the highest.

Simulated aerosol water could also play a role in the biases in extinction; however, the observed relative humidity over land was usually low and consequently water uptake on aerosols would likely be small. As shown in Table 5, the mean observed relative humidity aloft ranged between 37 and 49% among the three aircraft. The simulated relative humidity was close to observed for the G-1 flights, but the relative humidity was usually 6% too low for the WP-3D and CIRPAS Twin Otter flights. For the G-1 flight on June 27 (Fig. 25), observed relative humidity ranged from 20 to 55% and the model was ~5% too low over a portion of the flight path. The low relative humidity also implies that errors in simulated relative humidity do not adversely affect simulated water uptake. Nevertheless, the aircraft did not sample the entire vertical column as measured by the HSRL on the B-200 aircraft so there could be locations and times when the relative humidity is sufficiently high and permits condensation of water on aerosols. In addition to errors in aerosol composition mass, errors in the simulated size distribution (as shown in Section 4.4) could also affect the predicted optical properties.

We have also compared the simulated AOD with the AERONET measurements (Fig. 1d) made during the two-month simulation period as well as the measurements from the moving R/V Atlantis platform as shown in Fig. 26. Consistent with the lidar analyses, AOD is usually too high from the two

simulations that employ the MOZART boundary conditions of aerosols (DEF_ANT and 50%_ANT). The 50%_LBC simulation produces the AOD that is most consistent with the measurements. Much of the observed temporal variability is reproduced by the model at all the sites, except at Caltech. It is likely the bias in AOD at the Caltech site results from the large under-prediction of OA (Fig. 12) and SO_4^{2-} (Fig. 16) as well as sub-grid scale variability in emissions and meteorology. While the mean AOD from the 50%_ANT simulation (0.171) is closer to observed (0.160) at Caltech, that result is not consistent with the large under-prediction in surface aerosol concentrations. *Zhao et al.* [2013] use the WRF-Chem model, the 2008 CARB emission inventory, and MOZART boundary conditions to simulate AOD and aerosol radiative forcing over California during 2005. While the model configuration is different than in this study (i.e. coarser spatial resolution, different trace gas chemistry, and simpler aerosol model), their simulated AOD at four AERONET sites were similar to or lower than observed. It is not clear why the performance in simulated AOD is so different, since both modeling studies use MOZART to represent long-range transport of aerosols. It is possible that both global emission inventories (2005 versus 2010) and long-range transport (different synoptic conditions) contribute to different performance in MOZART over California.

As described by *Yu et al*. [2012], aerosols (mostly dust) originating from Asia likely contribute a significant fraction of the AOD over the western U.S. and the mass of dust imported from Asia is similar in magnitude to the total primary particulate emissions over North America. In the 0%_ANT simulation, dust from MOZART contributes on average to 50 – 85% of the total $PM_{2.5}$ in the free troposphere over California. This study clearly demonstrates that regional-scale AOD simulations depend on how well global chemical transport models represent the long-range transport of aerosols from Asia to North America. While there were no large dust events during our simulation period that might be represented reasonably well by global models, simulating relatively clean conditions is important when interpreting the simulated AOD during CalNex and CARES period. In addition to the treatment of dust emissions, uncertainties in anthropogenic emissions over Asia and how well MOZART represents processes that affect aerosol lifetime (e.g. chemical aging, wet removal) subsequently affects the boundary conditions used by the present regional-scale simulation.

6. Discussion

To investigate aerosol radiative forcing over California, as well as other regions, requires that temporal and spatial variations in aerosol mass, composition, and size be simulated reasonably well. While the overall performance of the model in simulating these quantities during the CalNex and CARES is similar to other studies, there is certainly room for improvement. We have presented differences between observed and simulated quantities that can be attributed to either local emissions, sub-grid scale

meteorology (particularly at the Pasadena site), secondary formation processes (mostly from SOA), long-range transport (mostly dust, but some anthropogenic species as well), or a combination of these uncertainties. To date, only a few aerosol modeling studies have been conducted using the CalNex and CARES data and brief comparison of the model performance with those studies is described next.

Ensberg et al. [2013] evaluated simulated inorganic and black carbon aerosols from the CMAQ model that used a domain encompassing southern California with a grid spacing of 4 km. Since that study also uses the CARB 2008 emission inventory, their CMAQ simulation should be most comparable to the DEF_ANT simulation. They also found that simulated BC concentrations were usually higher than observed, with biases between 0.09 to 0.19 $\mu g\ m^{-3}$ for five CIRPAS Twin Otter flights and between -0.03 and 0.07 $\mu g\ m^{-3}$ for five WP-3D flights. In this study, biases in BC are between 0.08 and 0.20 $\mu g\ m^{-3}$ for the same five Twin Otter flights and between 0.06 and 0.13 $\mu g\ m^{-3}$ for the same five WP-3D flights (Table S37). So the model performance is similar for the Twin Otter flights, but the present WRF-Chem simulation has a somewhat higher bias than CMAQ for the WP-3D flights. For inorganics, *Ensberg et al.* [2013] report biases in SO_4^{2-}, NO_3^-, and NH_4^+ that vary between 0.0 to 1.30 $\mu g\ m^{-3}$, -1.47 to -0.31 $\mu g\ m^{-3}$, and -0.77 to -0.11 $\mu g\ m^{-3}$, respectively among the ten aircraft flights. In this study, we obtain biases that vary between -0.19 to 0.32 $\mu g\ m^{-3}$, -2.22 to 0.75 $\mu g\ m^{-3}$, and -1.03 to 0.12 $\mu g\ m^{-3}$ for SO_4^{2-}, NO_3^-, and NH_4^+, respectively (Tables S39 – S41). Biases in SO_4^{2-} from CMAQ were consistently positive, while biases in NO_3^- and NH_4^+ were negative. In contrast, the biases in the present study were both higher and lower than observed for the inorganic aerosols depending on the flight. The different statistics between the CMAQ and WRF-Chem simulations likely arise from a number of factors. While the emissions are almost the same, the models use different treatments for meteorology, trace gas chemistry, and aerosols and employ boundary conditions from different global chemical transport models. Differences in SO_4^{2-} are likely to due the lack of aqueous chemistry and cloud-aerosol interactions in this study that might be important at times in the Los Angeles Basin and over the adjacent ocean where most of the CIRPAS Twin Otter measurements were collected.

Knote et al. [2013] also use the WRF-Chem model, with a similar domain size and resolution as in this suty, the 2008 CARB emission inventory, the MOSAIC aerosol model (but with 4 size bins), and the same global models for boundary conditions. Differences in their model configuration with the present study include some of the meteorological parameterizations, the use of the MOZART photochemical mechanism, SOA treatment, and a shorter simulation period. The simulated diurnal variations in SO_4^{2-}, NO_3^-, and NH_4^+ concentrations at the four supersites reported in *Knote et al.* [2013] are similar to those shown in this study. There are some differences in simulated NO_3^- at the Bakersfield and Pasadena sites and the simulated overall mean NH_4^+ is higher in *Knote et al.* [2013] and closer to observed. These differences are likely due to differences in the trace gas chemistry between MOZART

1116 and SAPRC-99 that will influence gas-to-particle partitioning. Not surprisingly, the largest difference
1117 between the two studies is associated with OA, with consistent over-predictions at the four supersites in
1118 *Knote et al*. [2013] and consistent under-predictions in this study. However, simulated average OA in this
1119 study is similar in magnitude to many of the aircraft measurements. *Knote et al* [2013] employ an
1120 anthropogenic SOA formation based on a tracer co-emitted with CO as described by *Hodzic and Jimenez*
1121 [2011], while the present study uses a VBS approach described in *Shrivastava et al*. [2011].
1122 Interestingly, simulated OH at the Pasadena site is higher than observed in our DEF_ANT simulation and
1123 is too low in *Knote et al*. [2013], showing that different photochemical mechanisms will lead to different
1124 biases in OH that will affect SOA concentrations to some extent. Since SOA is the largest fraction of OA
1125 at most sites and most times, differences in the treatment of SOA will have a large impact on simulated
1126 $PM_{2.5}$.
1127 It would be useful to compare the different treatments used in *Ensberg et al*. [2013] and *Knote et*
1128 *al.* [2013], as well as other studies with those used in this investigation to more fairly compare the
1129 performance of trace gas and aerosol treatments when all other processes such as domain configuration,
1130 meteorology, emissions, and boundary conditions are the same. This would also be useful to better
1131 identify the areas of improvement needed in specific processes that affect the aerosol lifecycle. Such a
1132 process-oriented methodology was proposed by *Fast et al*. [2011] and is worth considering in the future
1133 which can be achieved by merging code into a single version of WRF-Chem.
1134 It was also useful to examine model performance over all of California because of the terrain
1135 complexity and land-ocean contrasts that influences boundary-layer properties and circulations in the
1136 vicinity of major anthropogenic sources. In general, the magnitude and diurnal and multi-day variations
1137 in OA, SO_4^{2-} and NH_4^+ were better simulated over northern California, while NO_3^- was better simulated
1138 over southern California. While the temporal and spatial variations in BC were similar to observed, the
1139 simulated concentrations were usually too high everywhere using the CARB 2008 emissions. The
1140 magnitude was better represented in the model when BC emissions were reduced by half, suggesting a
1141 bias in the emissions inventory. Conversely, comparison of the POA factor determined from PMF
1142 analyses of AMS measurements with the simulated POA suggests that the CARB 2008 emissions
1143 inventory of POA was reasonable for this period. PMF analyses from the AMS measurements obtained
1144 on the G-1, WP-3D, and CIRPAS Twin Otter [*Craven et al*., 2013] aircraft are needed to further evaluate
1145 the emissions inventory. Over southern California, the largest errors in aerosol composition
1146 concentrations occurred at the Pasadena sampling site; however, these errors were smaller aloft along the
1147 aircraft transects in the vicinity of Los Angeles. The near-surface wind speed bias and the inability of the
1148 model to represent the large wind direction variations at the Pasadena site (Figs. S2d,e) suggests that sub-
1149 grid scale effects associated with the terrain are influencing model performance at this site. The model

performs better aloft because the aircraft sampled a significant portion of the urban plume affected by the larger-scale land-sea breezes and thermally-driven circulations in the basin. Differences in performance along the aircraft flight paths (predominately during the day) and at the Pasadena site may be due to a simulated nighttime boundary layer that is too shallow, leading to near-surface concentrations of most trace gases that are too high at night. The model performance is also better at the other three primary sampling sites because the local terrain is simpler and the 4 km grid spacing is likely sufficient to represent the local slope and valley thermally-driven circulations. However, sub-grid scale effects due to variations in emissions in the vicinity of the T1 site likely contribute to errors in the relative contribution of anthropogenic and biogenic sources of trace gases and aerosols.

Errors in simulated secondary aerosol formation and aging processes result from uncertainties in precursor emissions, missing multigenerational oxidative chemistry for organics, and model treatments of gas-to-particle partitioning. For example, there may be missing sources of SO_2^{2-} in a portion of the Los Angeles basin that could contribute to the under-prediction in SO_4^{2-} at the Pasadena site. However, we show that errors in SO_4^{2-} predictions over northern California are likely due to relatively small transport errors in space and time. It is not clear what processes are contributing to the under-prediction in NO_3^-. At the Pasadena site, simulated NH_3 was too high during most of the day on average suggesting that simulated NO_3^- should be too high. Therefore, the entire nitrogen cycle needs to be examined to determine whether emissions of other precursor species, such as NO and NO_2, are contributing to errors in NO_3^-. Unfortunately, there were no NH_3 and HNO_3 observations over northern California during CARES (other than a few WP-3D flights over northern California) to help evaluate the under predictions of NO_3^- at the surface and aloft in that region.

It is not surprising that there are errors in simulated OA concentrations, given that the theoretical understanding of SOA formation and chemical processing is incomplete. When the model does simulate reasonable OA concentrations, it may be for the wrong reasons. OA under-predictions in the current model may be due to missing important interactions associated with anthropogenic emissions influencing biogenic SOA [e.g. *Carlton et al.,* 2010] or using lower yields that neglect multigenerational biogenic chemistry [*Shrivastava et al*., 2011] which were shown to be important on some days during CARES [*Shilling et al.*, 2013; *Setyan et al*., 2012]. In addition, the current model does not include contributions of glyoxal chemistry that was shown by *Knote et al*. [2013] to potentially produce up to ~15% more SOA in the vicinity of the Los Angeles basin. Biomass burning was a source of trace gases and aerosols neglected in this study. While relatively few fires were observed in California by satellite detection methods during the 2-month period, biomass-burning aerosols from a large number of small, undetectable fires could contribute to the background concentrations of OA and BC. Analyses of the mass spectra from single particle measurements [*Cahill et al*., 2012] indicate that a substantial fraction of aerosols

could be associated with biomass burning; however, the analyses cannot determine whether they are due to local or distant sources and there can be confounding factors that lead to overestimation of biomass burning particles with single particle measurements [*Hayes et al*., 2013; *Aiken et al*., 2010]. In our study, biomass burning from long-rang transport is included through the boundary conditions, but the current MOZART configuration does not differentiate OA anthropogenic, biomass burning, or biogenic sources. Another issue is that MOZART likely underestimates SOA severely [*Dunlea et al*., 2009; *Emmons et al*., 2010], which influences the WRF-Chem boundary conditions of OA. We acknowledge that reducing the anthropogenic emission rates by 50% is arbitrary, but some adjustment is needed to account for likely reductions in emissions over time in California.

Considering that the current theoretical understanding of SOA formation and transformation processes is highly uncertain [e.g. *Jimenez et al.,* 2009], errors in the treatment of organic aerosol processes in models are expected [e.g. *Volkamer et al*., 2006; *Hodzic et al.*, 2010]. New insights from recent laboratory and field data [e.g. *Perraud et al*., 2012; *Vaden et al*. 2011; *Virtanen et al*. 2010] as well as explicit modeling studies [e.g. *Lee-Taylor et al*., 2011] that identify important organic chemical reactions, examine the role of semi- and intermediate volatile organic compounds, and quantify phase and volatility of SOA will likely provide improved modeling frameworks. Still unaccounted removal processes of organic vapors that are in equilibrium with SOA may also significantly affect SOA concentrations [*Hodzic et al*., 2013]. The results of simulated OA using a revised VBS framework that includes new findings on volatility and fragmentation [*Shrivastava et al*., 2013] will be presented in a subsequent study.

We demonstrated that evaluating predictions with only surface aerosol concentrations is insufficient in terms of understanding uncertainties contributing to column optical properties that affect aerosol radiative forcing. It would have been difficult, if not impossible, to ascertain errors associated with simulated aerosols originating outside of the California region without the extensive aircraft and remote sensing measurements available during CalNex and CARES. The regional sampling from the HSRL-1 on the B-200 aircraft was the most valuable measurement to quantify the over-prediction in aerosols in the free troposphere. Even though the simulated concentrations were relatively small in the free troposphere compared to boundary layer concentrations, the vertically integrated effect was large enough to affect predictions of AOD that will affect shortwave radiation reaching the surface. The in-situ measurements also provided some evidence of over-predictions in the free troposphere for transects upwind of urban emission sources; however, the lidar provides more complete information on aerosol loading and extinction in the vertical column than could possibly be obtained from in situ sampling. In addition, the in-situ measurements do not provide information for all aerosol components or coarse aerosols (> 1 μm). *Kassianov et al.* [2012] showed that coarse particles often contributed more than 50%

of the total observed aerosol volume during CARES and that even during clean conditions those coarse particles contribute significantly to direct aerosol radiative forcing. *Yu et al.* [2012] used satellite measurements averaged over multiple years to show that dust contributes a large fraction of the AOD over the northern Pacific Ocean. Additional analyses of single particle measurements [e.g. *Laskin et al*., 2012; *Moffet et al*., 2013; *Vaden et al*., 2011] coupled with size distribution information are needed to fully evaluate the simulated dust and sea-salt aerosol.

While no field campaign can provide measurements to evaluate every aspect of an aerosol model, the extensive meteorological, trace gas, and aerosol measurements collected during CalNex and CARES is the most comprehensive dataset currently available for the western U.S. It is particularly useful to assess the strengths and weaknesses of current and new treatments of SOA because of the proximity of both anthropogenic and biogenic precursors, the complexity of meteorology that will influence aerosol formation, growth, and removal, and the use of state-of-the-science instrumentation to provide data on organic gases and aerosols.

7. Summary and Conclusion

This study integrated the wide range of meteorological, chemistry, and aerosol data collected during the CARES and CalNex field campaigns and by operational monitoring networks into a single publically available dataset for the Aerosol Modeling Testbed. The AMT was used to comprehensively evaluate the performance of one configuration of the WRF-Chem model to simulate aerosols and their precursors over California between May and June of 2010. We also assessed the sensitivity of the aerosol predictions to uncertainties associated with the emission inventories and boundary conditions. Independent measurements showed that the model captured the overall meteorological conditions as reflected in simulated temperature, humidity, cloudiness, circulations, and boundary layer depth. Any errors in the meteorological quantities are consistent with those typically seen in other other mesoscale modeling studies.

The main findings of this modeling study are:

- Reducing the 2008 CARB emissions inventory by 50% improved simulated CO, NO_x, and anthropogenic hydrocarbons such as toluene and formaldehyde at most sites and along most aircraft flight paths.
- Reducing anthropogenic emission rates led to reductions in mixing ratios of isoprene and terpene when biogenic emissions rates remained the same. It is possible that there are uncertainties in biogenic emissions from the on-line MEGAN model used in WRF-Chem, but uncertainties in these emissions are also coupled to interactions with anthropogenic sources that affect the

oxidation capacity of the atmosphere, as shown by comparing the simulations with and without anthropogenic emissions. Isoprene mixing ratios were usually too low in the simulations that employed anthropogenic emissions, except at the Bakersfield site and along the WP-3D flights north of 35^{o} N where the simulated values were similar to observations.

- Simulated spatial and temporal variability in BC was qualitatively similar to surface and aircraft measurements when emissions of BC are reduced by 50%.
- While the spatial and temporal variability of OA is simulated reasonably well, the magnitude is generally too low, particularly at the Pasadena site. In contrast with other adjustments to the emissions, comparisons with PMF results suggest that the original POA emission estimates may be reasonable.
- Simulated SO_4^{2-} was too low in southern California, but the magnitude as well as the diurnal and multi-day variability was better represented over northern California.
- Simulated NO_3^- was too low everywhere, but the magnitude as well as the diurnal and multi-day variability was better represented over southern California.
- Long-range transport of aerosols simulated by the global model was likely too high in the free troposphere even though their concentrations were relatively low. In addition, the sensitivity simulation that removed anthropogenic emissions suggest that CO from long-range transport might be up to 20 ppb too high.
- The bias in aerosols in the free troposphere leads to over-predictions in AOD by about a factor of two, and offsets the effect of the under-predictions of boundary-layer aerosols resulting primarily from local emissions. Reducing aerosol concentrations by half from long-range transport greatly improves the simulated AOD in all regions of California.

Our long-term objectives are to use WRF-Chem to quantify regional-scale variations in aerosol radiative forcing over California and determine the relative role of emissions from local and distant sources. This study was a necessary first step that rigorously evaluates simulated aerosol mass, composition, and size distribution. These properties influence the model's treatment of optical properties and consequently aerosol radiative forcing. While this study does not extensively examine all simulated aerosol optical properties, we evaluated simulated AOD and extinction profiles to check for consistency with simulated aerosol concentrations. Our evaluation using measurements from in-situ and remote instrumentation deployed on the surface, aircraft, and ship platforms shows that simulated mass and composition both at the surface and aloft needs improvement to better represent AOD and extinction profiles and to have confidence in calculations of aerosol radiative forcing during the CalNex and CARES

periods as well as other time periods. In addition, an evaluation of the simulated single scattering albedo and other optical properties is needed.

The extensive data collected during CalNEX and CARES provide a valuable opportunity to make sure that aerosol optical properties are simulated adequately for the correct reasons. The combined field campaign and operational data provide an ideal testbed to evaluate aerosol models in more detail and develop improved treatments for aerosol processes. Simulating SOA is particularly important since it is often the largest fraction of observed fine mode aerosol mass. New particle formation events were observed during CARES [*Zaveri et al*., 2012; *Setyan et al*., 2014] and CalNex [*Alm et al*., 2012; *Pennington et al.*, 2012] and better representing the growth of aerosols could affect the overall mass and number in the region. Some studies are beginning to explore the role of mixing state on aerosol optical properties and cloud condensation nuclei [e.g. *Zhang et al*., 2013; *Matsui et al.*, 2013], which could be important at regional spatial scales. These challenging issues will be explored in forthcoming studies using the CalNex and CARES testbed.

Acknowledgements: We thank the numerous scientists (including Ronald Cohen, Allen Goldstein, Joost de Gouw, Tom Ryerson, Ilana Pollack, and Carsten Warneke), pilots, and other staff that contributed to the data collection during CalNex and CARES. CalNex was sponsored by the National Oceanographic and Atmospheric Administration (NOAA) Climate Change and Air Quality programs, the National Aeronautics and Space Administration (NASA) Radiation Sciences and Tropospheric Chemistry program, and the California Air Resources Board. CARES was supported by the U.S. Department of Energy's (DOE) Atmospheric Radiation Measurement (ARM) and Atmospheric System Research (ASR) programs. Patrick Hayes and Jose Jimenez were partially supported by CARB 11-305 and DOE (BER/ASR) DE-SC0006035 and Patrick Hayes was also partially supported by a CIRES Visiting Postdoctoral Fellowship. We thank Elaine Chapman for providing comments on this manuscript. Funding for this research has been provided by the U.S. NOAA's Atmospheric Composition and Climate Program (NA11OAR4310160) and utilized resources provided by the Pacific Northwest National Laboratory (PNNL) Institutional Computing program. PNNL is operated for the U.S. DOE by Battelle Memorial Institute.

References

Aan de Brugh, J.M.J., Henzing, J.S., Schaap, M., Morgan, W.T., van Heerwaarden, C.C., Weijers, E.P., Coe, H., and Krol1, M.C.: Modelling the partitioning of ammonium nitrate in the convective boundary layer, *Atmos. Chem. Phys.,* 12, 3005-3023, doi:10.5194/acp-12-3005-2012, 2012.

Ahlm, L., Liu, S., Day, D.A., Russell, L.M., Weber, R., Gentner, D.R. Goldstein, A.H., DiGangi, J.P., Henry, S.B., Keutsch, F.N., VandenBoer, T.C., Markovic, M.Z., Murphy, J.G., Ren, X., and Scheller,

S.: Formation and growth of ultrafine particles from secondary sources in Bakersfield, California, *J. Geophys. Res*., 117, D00V08, doi:10.1029/2011jd017144, 2012.

Aiken, A.C., de Foy, B., Wiedinmyer, C., DeCarlo, P.F., Ulbrich, I.M., Wehrli, M.N., Szidat, S., Prevot, A.S.H., Noda, J., Wacker, L., Volkamer, R., Fortner, E., Wang, J., Laskin, A., Shutthanandan, V., Zheng, J., Zhang, R., Paredes-Miranda, G., Arnott, W.P., Molina, L.T., Sosa, G., Querol, X., and Jimenez, J.: Mexico city aerosol analysis during MILAGRO using high resolution aerosol mass spectrometry at the urban supersite (T0) – Part 2: Analysis of the biomass burning contribution and the non-fossil carbon fraction, *Atmos. Chem. Phys*., 10, 5315-5341, doi:10.5194/acp-10-5315-2010, 2010.

Angevine, W.M., Eddington, L., Durkee, K., Fairall, C., Bianco, L., and Brioude, J.: Meteorological model evaluation for CalNex 2010, *Mon. Wea. Rev*., 140, 3885-3906, doi:10.1175/MWR-D-12-00042.1, 2012.

Bahadur, R., Feng, Y., Russell, L.M., and Ramanathan, V.: Impact of California's air pollution laws on black carbon and their implications for direct radiative forcing, *Atmos. Environ*., 45, 11662-1167, 2011.

Bahreini, R., Ervens, B., Middlebrook, A.M., Warneke, C., de Gouw, J.A., DeCarlo, P.F., Jimenez, J.L., Brock, C.A., Neuman, J.A., Ryerson, T.B., Stark, H., Atlas, E., Brioude, J., Fried, A., Holloway, J.S., Peischl, J., Richter, D., Walega, J., Weibring, P., Wollny, A.G., and Fehsenfeld, F.C.: Organic aerosol formation in urban and industrial plumes near Houston and Dallas, Texas, *J. Geophys. Res*., 114, D00F16, doi: 10.1029/2008JD011493, 2009.

Bahreini, R., Middlebrook, A.M., de Gouw, J.A., Warneke, C., Trainer, M., Brock, C.A., Stark, H., Brown, S.S., Dube, W.P., Gilman, J.B., Hall, K., Holloway, J.S., Kuster, W.C., Perring, A.E., Prevot, A.S.H., Schwarz, J.P., Spackman, J.R., Szidat, S., Wagner, N.L., Weber, R.J., Zotter, P., and Parrish, D.D.: Gasoline emissions dominate over diesel in formation of secondary organic aerosol mass, *Geophys. Res. Lett.*, 39, L06805, doi:10.1029/2011GL050718, 2012.

Baklanov, A., Schlünzen, K., Suppan, P., Baldasano, J., Brunner, D., Aksoyoglu, S., Carmichael, G., Douros, J., Flemming, J., Forkel, R., Galmarini, S., Gauss, M., Grell, G., Hirtl, M., Joffre, S., Jorba, O., Kaas, E., Kaasik, M., Kallos, G., Kong, X., Korsholm, U., Kurganskiy, A., Kushta, J., Lohmann, U., Mahura, A., Manders-Groot, A., Maurizi, A., Moussiopoulos, N., Rao, S.T., Savage, N., Seigneur, C., Sokhi, R.S., Solazzo, E., Solomos, S., Sørensen, B., Tsegas, G., Vignati, E., Vogel, B., and Zhang, Y.: Online coupled regional meteorology chemistry models in Europe: current status and prospects, *Atmos. Chem. Phys*., 14, 317-398, doi:10.5194/acp-14-317-2014, 2014.

Bao, J.-W., Michelson, S.A., Persson, P.O.G., Djalavoa, I.V., and Wilczak, J.M.: Observed and WRF-simulated low-level winds in a high-ozone episode during the Central California Ozone Study, *J. Appl. Meteor. Clim*., 47, 2372-2394, 2008.

Baron, P.A., and Willeke, K.: Aerosol Measurement: Principles, Techniques and Applications, 2nd Edition, Wiley-Interscience, New York, 1168 pp, 2001.

Barth, M.C., Kim, S.-W., Wang, C., Pickering, K.E., Ott, L.E., Stenchikov, G., Leriche, M., Cautenet, S., Pinty, J.-P., Barthe, Ch., Mari, C., Helsdon, J.H., Farley, R.D., Fridlind, A.M., Ackerman, A.S., Spiridonov, V., and Telenta, B.: Cloud-scale model intercomparison of chemical constituent transport in deep convection, *Atmos. Chem. Phys.*, 7, 4709-4731, 2007.

Bouvier-Brown, N.C., Goldstein, A.H., Gilman, J.B., Kuster, W.C., and de Gouw, J.A.: In-situ ambient quantification of monoterpenes, sesquiterpenes, and related oxygenated compounds during BEARPEX 2007: implications for gas- and particle-phase chemistry, *Atmos. Chem. Phys*., 9, 5505-5518, 2009.

1363 Brioude, J., Angevine, W.M., Ahmadov, R., Kim, S.-W., Evan, S., McKeen, S.A. Hsie, E.-Y., Frost, G.J.,
1364 Neuman, J.A., Pollack, I.B., Peischl, J., Ryerson, T.B., Holloway, J., Brown, S.S., Nowak, J.B.,
1365 Roberts, J.M., Wofsy, S.C., Santoni, G.W., Oda, T., and Trainer, M.: Top-down estimate of surface
1366 flux in the Los Angeles Basin using a mesoscale inverse modeling technique: assessing anthropogenic
1367 emissions of CO, NO_x and CO_2 and their impacts, *Atmos. Chem. Phys*., 13, 3661–3677,
1368 doi:10.5194/acp-13-3661-2013, 2013.

1369 Cahill, J.F., Suski, K., Seinfeld, J.H., Zaveri, R.A., and Prather, K.A.: The mixing state of carbonaceous
1370 aerosol particles in northern and southern California measured during CARES and CalNex 2010,
1371 *Atmos. Chem. Phys*., 12, 10989–11002, doi:10.5194/acp-12-10989-2012, 2012.

1372 Canagaratna M.R., Jayne, J.T., Jimenez, J.L., Allan, J.D., Alfarra, M.R., Zhang, Q., Onasch, T.B.,
1373 Drewnick, F., Coe, H., Middlebrook, A. Delia, A., Williams, L.R., Trimborn, A.M., Northway, M.J.,
1374 DeCarlo, P.F., Kolb, C.E., Davidovits, P., and Worsnop, D.R.: Chemical and microphysical
1375 characterization of ambient aerosols with the aerodyne aerosol mass spectrometer, *Mass Spectrom*
1376 *Rev*., 62, 185-222, doi:10.1002/mas.20115, 2007.

1377 CARB: The California Almanac of Emissions and Air Quality – 2009 Edition, Available at:
1378 *http://www.arb.ca.gov/aqd/almanac/almanac09/chap309.htm,* 2009.

1379 Carlton, A.G., Pinder, R.W., Bhave, P.V., and Pouliot, G.A.: To what extent can biogenic SOA be
1380 controlled? *Environ. Sci. Technol*., 44, 3376–3380, doi:10.1021/es903506b, 2010.

1381 Carter,W.P.L.: Documentation of the SAPRC-99 Chemical Mechanism for VOC Reactivity Assessment,
1382 Draft report to the California Air Resources Board. Contracts 92–329 and 95–308, 8 May, Available
1383 at: *http://www.cert.ucr.edu/_carter/absts.htm#saprc99*, 2000a.

1384 Carter, W.P.L.: Implementation of the SAPRC-99 Chemical Mechanism into the Models-3 Framework,
1385 Report to the United States Environmental Protection Agency, 29 January, Available at:
1386 *http://www.cert.ucr.edu/_carter/absts.htm#s99mod3*, 2000b.

1387 Chan, A.W.H., Isaacman, G., Wilson, K.R., Worton, D.R., Ruehl, C.R., Nah, T., Gentner, D.R.,
1388 Dallmann, T.R., Kirchstetter, T.W., Harley, R.A., Gilman, J.G., Kuster, W.C., de Gouw, J.A.,
1389 Offenberg, J.H., Kleindienst, T.E., Lin, Y.H., Rubitschun, C.L., Surratt, J.D., Hayes, P.L.,Jimenez,
1390 and J.L., Goldstein, A.H.: Detailed chemical characterization of unresolved complex mixtures in
1391 atmospheric organics: Insights into emission sources, atmospheric processing, and secondary organic
1392 aerosol formation, *J. Geophys. Res.,* 118, 6783–6796, doi:10.1002/jgrd.50533, 2013.

1393 Chow, J.C., Chen, L.W.A., Watson, J.G., Lowenthal, D.H., Magliano, K.A., Turkiewicz, K., and
1394 Lehrman, D.E.: PM2.5 chemical composition and spatiotemporal variability during the California
1395 Regional PM10/PM2.5 Air Quality Study (CRPAQS), *J. Geophys. Res*., 111, D10S04, 2006.

1396 Cooper, O.R., Oltmans, S.J., Johnson, B.J., Brioude, J., Angevine, W., Trainer, M., Parrish, D.D.,
1397 Ryerson, T.R., Pollack, I., Cullis, P.D., Ives, M.A., Tarasick, D.W., Al-Saadi, J., and Stajner, I.:
1398 Measurement of western U.S. baseline ozone from the surface to the tropopause and assessment of
1399 downwind impact regions, *J. Geophys. Res*., 116, D00V03, doi:10.1029/2011JD016095, 2011.

1400 Craven, J.S., Metcalf, A.R., Bahreini, R., Middlebrook, A., Hayes, P.L., Duong, H.T., Sorooshian, A.,
1401 Jimenez, J.L., Flagan, R.C., and Seinfeld, J.H.: Los Angeles Basin airborne organic aerosol
1402 characterization during CalNex, *J. Geophys. Res*., 118, 11,453–11,467, doi:10.1002/jgrd.50853, 2013.

1403 Croes, B.E., and Fujita, E.M.: Overview of the 1997 Southern California Ozone Study (SCOS97-
1404 NARSTO), *Atmos. Environ*., 37, S3-S26, doi:10.1016/S1352-2310(03)00379-0, 2003.

1405 DeCarlo, P.F. Slowik, J.G., Worsnop, D.R., Davidovits, P., and Jimenez, J.L.: Particle morphology and
1406 density characterization by combined mobility and aerodynamic diameter measurements. Part 1:
1407 Theory, *Aerosol. Sci. Tech*., 38, 1185-1205, doi:10.1080/027868290903907, 2004.

Docherty, K.S., Aiken, A.C., Huffman, J.A., Ulbrich, I.M., DeCarlo, P.F., Sueper, D., Worsnop, D.R., Snyder, D.C., Peltier, R.E., Weber, R.J., Grover, B.D., Eatough, D.J., Williams, B.J., Goldstein, A.H., Ziemann, P.J., and Jimenez, J.L.: The 2005 Study of Organic Aerosols at Riverside (SOAR- 1): instrumental intercomparisons and fine particle composition, *Atmos. Chem. Phys*., 11, 12387-12420, 2011.

Dubovik, O., Holben, B., Eck, T.F., Smirnov, A., Kaufman, Y.J., King, M.D., Tanre, D., and Slutsker, I.: Variability of absorption and optical properties of key aerosol types observed in worldwide locations, *J. Atmos. Sci*., 59, 590−608, 2002.

Dunlea, E.J., DeCarlo, P.F., Aiken, A.C., Kimmel, J.R., Peltier, R.E., Weber, R.J., Tomlinson, J., Collins, D.R., Shinozuka, Y., McNaughton, C.S., Howell, S.G., Clarke, A.D., Emmons, L.K., Apel, E.C., Pfister, G.G., van Donkelaar, A., Martin, R.V., Millet, D.B., Heald, C.L., and Jimenez, J.L.: Evolution of Asian aerosols during transpacific transport in INTEX-B, *Atmos. Chem. Phys*., 9, 7257-7287, 2009.

Duong, H.T., Sorooshian, A., Craven, J.S., Hersey, S.P., Metcalf, A.R., Zhang, X., Weber, R.J., Jonsson, H., Flagan, R.C., and Seinfeld, J.H.: Water-soluble organic aerosol in the Los Angeles Basin and outflow regions: Airborne and ground measurements during the 2010 CalNex field campaign, *J. Geophys. Res*., 116, D00V04, doi:10.1029/2011JD016674, 2011.

Emmons, L.K., Walters, S., Hess, P.G., Lamarque, J.-F., Pfister, G.G., Fillmore, D., Granier, C., Guenther, A., Kinnison, D., Laepple, T., Orlando, J., Tie, X., Tyndall, G., Wiedinmyer, C., Baughcum, S.L., and Kloster, S.: Description and evaluation of the Model for Ozone and Related chemical Tracers, version 4 (MOZART-4), *Geosci. Model Dev*., 3, 43–67, doi:10.5194/gmd-3-43-2010, 2010.

Ensberg, J.J., J.S. Craven, A.R. Metcalf, J.D. Allan, W.M. Angevine, R. Bahreini, J. Brioude, C. Cai, H. Coe, J.A. de Gouw, R.A. Ellis, J.H. Flynn, C.L. Haman, P.L. Hayes, J. L. Jimenez, B.L. Lefer, A.M. Middlebrook, J.G. Murphy, J.A. Neuman, J.B. Nowak, J.M. Roberts, J. Stutz, J.W. Taylor, P.R. Veres, J.M. Walker, and J.H. Seinfeld: Inorganic and black carbon aerosols in the Los Angeles Basin during CalNex, *J. Geophys. Res*., 118, 1777-1803, doi:10.1029/2012JD018136, 2013.

Ervens, B., B.J. Turpin, and R.J. Weber: Secondary organic aerosol formation in cloud droplets and aqueous particles (aqSOA): A review of laboratory, field and model studies, *Atmos. Chem. Phys*., 11, 11069-11102, doi:10.5194/acp-11-11069-2011, 2011.

Fahey, K.M., and Pandis, S.N.: Optimizing model performance: Variable size resolution in cloud chemistry modeling, *Atmos. Environ*., 35, 4471–4478, 2001.

Fast, J.D., Gustafson Jr., W.I., Berg, L.K., Shaw, W.J., Pekour, M., Shrivastava, M., Barnard, J.C., Ferrare, R.A., Hostetler, C.A., Hair, J.A., Erickson, M., Jobson, B.T., Flowers, B., Dubey, M.K. Springston, S., Pierce, R.B., Dolislager, L., Pederson, J., and Zaveri, R.A.: Transport and mixing patterns during the Carbonaceous Aerosol and Radiative Effects Study (CARES), *Atmos. Chem. Phys.,* 12, 1759-1783, 2012.

Fast, J.D., Gustafson Jr., W.I., Chapman, E.G., Easter, R.C., Rishel, J., Zaveri, R.A., Grell, G., and Barth, M.: The Aerosol Modeling Testbed: A community tool to objectively evaluate aerosol process modules, *Bull. Amer. Meteor. Soc*., 92, 343-360, 2011.

Fast, J.D, Gustafson, Jr., W.I., Easter, R.C., Zaveri, R.A., Barnard, J.C., Chapman, E.G., and Grell, G.A.: Evolution of ozone, particulates, and aerosol direct forcing in an urban area using a new fully-coupled meteorology, chemistry, and aerosol model, *J. Geophys. Res.,* 111, doi:10.1029/2005JD006721, 2006.

Feng, Y., Penner, J.E., Silman, S., and Liu, X.: Effects of cloud overlap in photochemical models, *J. Geophys. Res*., 109, D04310, doi;10.1029/2003JD004040, 2004.

Fraser, M.P., Grosjean, D., Grosjean, E., and Cass, G.R.: Air quality model evaluation data for organics, 1, Bulk chemical composition and gas/particle distribution factors, *Environ. Sci. Technol*., 30, 1731–1743, 1996.

Fujita, E.M., Campbell, D.E., and Snorradottir, T.: Central California Ozone Study (CCOS) Data Validation: Final Report, Prepared for San Joaquin Valleywide Air Pollution Study Agency, California Air Resources Board. Available *at http://www.dri.edu/project-reports?start=1*, 2005.

Gentner, D.R., Isaacman, G., Worton, D.R., Chan, A.W.H., Dallmann, T.R., Davis, L., Liu, S., Day, D.A., Russell, L.M., Wilson, K.R., Weber, R., Guha, A., Harley, R.A., and Goldstein, A.H.: Elucidating secondary organic aerosol from diesel and gasoline vehicles through detailed characterization of organic carbon emissions, *Proc. Natl. Acad. Sci. U.S.A.,* 109(45), 18,318–18,323, doi:10.1073/pnas.1212272109, 2012.

Gong, S. L., Barrie, L.A., and Lazare, M.: Canadian Aerosol Module (CAM): A size-segregated simulation of atmospheric aerosol processes for climate and air quality models, 2. Global sea-salt aerosol and its budgets, *J. Geophys. Res., 107 (D24)*, doi:10.1029/2001JD002004, 2002.

Granier, C., Bessagnet, B., Bond, T., D'Angiola, A., van der Gon, H.D., Frost, G.J., Heil, A., Kaiser, J.W., Kinne, S., Klimont, Z., Kloster, S. Lamarque, J.-F., Liousse, C., Masui, T., Meleux, F., Mieville, A., Ohara, T., Raut, J.-C., Riahi, K., Schultz, M.G., Smith, S.J., Thompson, A., van Aardenne, J., van der Werf, G.R., van Vuuren, D.P.: Evolution of anthropogenic and biomass burning emissions of air pollutants at global and regional scales during the 1980–2010 period, *Climate Change*, 109, 163-190, doi:10.1007/s10584-011-0154-1, 2011.

Grell, G.A., Peckham, S.E., Schmitz, R., McKeen, S.A., Frost, G., Skamarock, W.C., and Eder, B.: Fully coupled "online" chemistry within the WRF model, *Atmos. Environ*., 39, 6957-6975, 2005.

Griffin, R.J.., Dabdub, D., Kleeman, M.J., Fraser, M.P. Cass, G.R., and Seinfeld, J.H.: Secondary organic aerosol 3. Urban/regional scale model of size- and composition-resolved aerosols, *J. Geophys. Res*., 107, 4334, doi:10.1029/2001JD000544, 2002.

Guenther, A., Karl, T., Harley, P., Wiedinmyer, C., Palmer, P.I., and Geron, C.: Estimates of global terrestrial isoprene emissions using MEGAN (Model of Emissions of Gases and Aerosols from Nature), *Atmos. Chem. Phys*., 6, 3181-3210, 2006.

Gustafson, W.I. Jr., Berg, L.K., Easter, R.C., and Ghan, S.J.: The Explicit-Cloud Parameterized-Pollutant hybrid approach for aerosol–cloud interactions in multiscale modeling framework models: tracer transport results, *Environ. Res. Lett*., 3, 025005, doi:10.1088/1748-9326/3/2/025005, 2008.

Gustafson, W.I. Jr., Qian, Y., and Fast, J.D.: Downscaling aerosols and the impact of neglected sub-grid processes on aerosol radiative forcing for a representative GCM grid spacing, *J. Geophys. Res.* 116, D13303, doi:10.1029/2010JD015480, 2011.

Hair, J.W., Hostetler, C.A., Cook, A.L., Harper, D.B., Ferrare, R.A., Mack, T.L., Welch, W., Izquierdo, L.R., and Hovis, F.E.: Airborne High Spectral Resolution Lidar for profiling aerosol optical properties, *Appl. Optics*, 47(36), 6734-6752, doi: 10.1364/AO.47.006734, 2008.

Hayes, P.L., Ortega, A.M., Cubison, M.J., Froyd, K.D., Zhao, Y., Cliff, S.S., Hu, W.W., Toohey, D.W. Flynn, J.H., Lefer, B.L., Grossberg, N., Alvarez, S., Rappenglück, B., Taylor, J.W., Allan, J.D., Holloway, J.S., Gilman, J.B., Kuster, W.C., de Gouw, J.A., Massoli, P., Zhang, X., Liu, J., Weber, R.J., Corrigan, A.L., Russell, L.M., Isaacman, G., Worton, D.R., Kreisberg, N.M., Goldstein, A.H., Thalman, R., Waxman, E.M., Volkamer, R., Lin, Y.H., Surratt, J.D., Kleindienst, T.E., Offenberg, J.H., Dusanter, S., Griffith, S., Stevens, P.S., Brioude, J., Angevine, W.M., and Jimenez, J.L.: Organic

aerosol composition and sources in Pasadena, California, during the 2010 CalNex campaign, *J. Geophys. Res*., 118, 9233-9257, doi:10.1009/jgrd.50530, 2013.

Heald, C.L. Coe, H., Jimenez, J.L., Weber, R.J., Bahreini, R., Middlebrook, A.M., Russell, L.M., Jolleys, M., Fu, T.-M., Allan, J.D., Bower, K.N., Capes, G., Crosier, J., Morgan, W.T., Robinson, N.H., Williams, P.I., Cubison, M.J., DeCarlo, P.F., and Dunlea, E.J.: Exploring the vertical profile of atmospheric organic aerosol: comparing 17 aircraft field campaigns with a global model *Atmos. Chem. Phys.*, 11, 12673-12696, doi:10.5194/acp-11-12673-2011, 2011.

Heald, C.L., Collett Jr., J.L., Lee, T., Benedict, K.B., Schwandner, F.M., Li, Y., Clarisse, L., Hurtmans, D.R., Van Damme, M., Clerbaux, C., Coheur, P.-F., Philip, S., Martin, R.V., and Pye, H.O.T.: Atmospheric ammonia and particulate inorganic nitrogen over the United States, *Atmos. Chem. Phys.*, 12, 10295–10312, doi:10.5194/acp-12-10295-2012, 2012.

Held, T., Ying, Q., Kleeman, M.J., Schauer, J.J., and Fraser, M.P.: Comparison of the UCD/CIT air quality model and the CMB source–receptor model for primary airborne particulate matter, *Atmos. Environ*. 39, 2281-2297, doi:10.1016/j.atmosenv.2004.12.034, 2005.

Herndon, S.C., Onasch, T.B., Wood, E.C., Kroll, J.H., Canagaratna, M.R., Jayne, J.T., Zavala, M.A., Knighton, W.B., Mazzoleni, C., Dubey, M.K., Ulbrich, I.M., Jimenez, J.L., Seila, R., de Gouw, J.A., de Foy, B., Fast, J., Molina, L.T., Kolb, C.E., and Worsnop, D.R.: The correlation of secondary organic aerosol with odd oxygen in a megacity outflow, *Geophys. Res. Lett., 35,* L15804, doi:10.1029/2008GL034058, 2008.

Hersey, S.P., Craven, J.S., Metcalf, A.R., Lin, J., Lathem, T., Suski, K.J., Cahill, J.F., Duong, H.T., Sorooshian, A., Jonsson, H.H., Shiraiwa, M., Zuend, A., Nenes, A., Prather, K.A., Flagan, R.C., and Seinfeld, J.H.: Composition and hygroscopicity of the Los Angeles Aerosol: CalNex, *J. Geophys. Res*., 118, 3016-3036, doi:10.1022/jgrd.50307, 2013.

Hodzic, A. and Jimenez, J.L.: Modeling anthropogenically controlled secondary organic aerosols in a megacity: a simplified framework for global and climate models, *Geosci. Model Dev*., 4, 901–917, doi:10.5194/gmd-4-901-2011, 2011.

Hodzic, A., Jimenez, J.L., Madronich, S., Canagaratna, M.R., DeCarlo, P.F., Kleinman, L., and Fast, J.: Modeling organic aerosols in a megacity: potential contribution of semi-volatile and intermediate volatility primary organic compounds to secondary organic aerosol formation, *Atmos. Chem. Phys.*, 10, 5491-5514, doi:10.5194/acp-10-5491-2010, 2010.

Hodzic A., Madronich, S., Aumont B., Lee-Taylor, J., Karl, T., Camredon, M., and Mouchel-Vallon, C.: Limited influence of dry deposition of semi-volatile organic vapors on secondary organic aerosol formation in the urban plume, *Geophys. Res. Lett*., 40, 3302–3307, 2013.

Holben, B.N., Eck, T.F., Slutsker, I., Tanré, D., Buis, J.P., Setzer, A., Vermote, E., Reagan, J.A., Kaufman, Y., Nakajima, T., Lavenu, F., Jankowiak, I., and Smirnov, A.: AERONET—A federated instrument network and data archive for aerosol characterization, *Remote Sensing Environ*., 66, 1–16, 1998.

Huang, M., Carmichael, G.R., Adhikary, B., Spak, S.N., Kulkarni, S., Cheng, Y.F., Wei, C., Tang, Y., Parrish, D.D., Oltmans, S.J., D'Allura, A., Kaduwela, A., Cai, C., Weinheimer, A.J., Wong, M., Pierce, R.B., Al-Saadi, J.A., Streets, D.G., and Zhang, Q.: Impacts of transported background ozone on California air quality during the ARCTAS-CARB period – a multi-scale modeling study, *Atmos. Chem. Phys*., 10, 6947-6968, doi:10.5194/acp-10-6947-2010, 2010.

Huang M., Carmichael, G.R., Kulkarni, S., Streets, D.G., Lu, Z., Zhang, Q., Pierce, R.B., Kondo, Y., Jimenez, J.L., Cubison, M.J., Anderson, B., and Wisthaler, A.: Sectoral and geographical contributions to summertime continental United States (CONUS) black carbon spatial distributions, *Atmos. Environ*., 51, 165-174, doi:10.1016/j.atmosenv.2012.01.021, 2012.

1543 Jacob, D.J., Crawford, J.H., Maring, H., Clarke, A.D., Dibb, J.E., Emmons, L.K., Ferrare, R.A., Hostetler,
1544 C.A., Russell, P.B., Singh, H.B., Thompson, A.M., Shaw, G.E., McCauley, E., Pederson, J.R., and
1545 Fisher, J.A.: The Arctic Research of the Composition of the Troposphere from Aircraft and Satellites
1546 (ARCTAS) mission: design, execution, and first results, *Atmos. Chem. Phys*., 10, 5191-5212,
1547 doi:10.5194/acp-10-5191-2010, 2010.

1548 Jacobson, M.Z.: Development and application of a new air pollution modeling system – Part III. Aerosol-
1549 phase simulations, *Atmos. Environ.,* 31, 587-608, 1997.

1550 Jacobson, M.Z.: GATOR-GCMM 2. A study of daytime and nighttime ozone layers aloft, ozone in
1551 national parks, and weather during the SARMAP field campaign, *J. Geophys. Res*., 106, 5403-5420,
1552 2001.

1553 Jimenez, J.L., Canagaratna, M.R., Donahue, N.M., Prevot, A.S.H., Zhang, Q., Kroll, J.H., DeCarlo, P.F.,
1554 Allan, J.D., Coe, H., Ng, N.L., Aiken, A.C., Docherty, K.S., Ulbrich, I.M., Grieshop, A.P., Robinson,
1555 A.L., Duplissy, J., Smith, J.D., Wilson, K.R., Lanz, V.A., Hueglin, C., Sun, Y.L., Tian, J., Laaksonen,
1556 A., Raatikainen, T., Rautiainen, J., Vaattovaara, P., Ehn, M., Kulmala, M., Tomlinson, J.M., Collins,
1557 D.R., Cubison, M.J., Dunlea, E.J., Huffman, J.A., Onasch, T.B., Alfarra, M.R., Williams, P.I., Bower,
1558 K., Kondo, Y., Schneider, J., Drewnick, F., Borrmann, S., Weimer, S., Demerjian, K., Salcedo, D.,
1559 Cottrell, L., Griffin, R., Takami, A., Miyoshi, T., Hatakeyama, S., Shimono, A., Sun, J.Y., Zhang,
1560 Y.M., Dzepina, K., Kimmel, J.R., Sueper, D., Jayne, J.T., Herndon, S.C., Trimborn, A.M., Williams,
1561 L.R., Wood, E.C., Middlebrook, A.M., Kolb, C.E., Baltensperger, U., and Worsnop, D.R.: Evolution
1562 of organic aerosols in the atmosphere, *Science*, 326, 1525–1529, doi:10.1126/science.1180353, 2009.

1563 Jin, L., Brown, N.J., Harley, R.A., Bao, J.-W., Michelson, S.A., and Wilczak, J.M.: Seasonal versus
1564 episodic performance evaluation for an Eulerian photochemical air quality model, *J. Geophys. Res*.,
1565 115, D09302, doi:10.1019/2009JD12680, 2010.

1566 Kang, D., Mathur, R., and Rao, S.T.: Assessment of bias-adjusted PM2.5 air quality forecasts over the
1567 continental United States during 2007, *Geosci. Model Dev*., 3, 309–320, 2010.

1568 Kassianov, E., Pekour, M., and Barnard, J.: Aerosols in central California: Unexpectedly large
1569 contribution of coarse mode to aerosol radiative forcing, *Geophys. Res. Lett*., 39, L20806,
1570 doi:10.1029/2012GL053469, 2012.

1571 Knote C., Hodzic, A., Jimenez, J.L., Volkamer, R., Baidar, S., Brioude, J., Fast, J.D., Gilman, J.B.,
1572 Goldstein, A., de Gouw, J., Hayes, P., Jobson, B.T., Knighton, W.B., Kuster, W.C., Oetjen, H.,
1573 Orlando, J., Song, C., Stark, H., Stevens, P.S., Thalman, R., Tyndall, G., Warneke, C., Washenfelder,
1574 R., Waxman, E., and Zhang, Q.: Simulation of semi-explicit mechanisms of SOA formation from
1575 glyoxal in a 3D model, *Atmos. Chem. Phys. Discuss*. 13, 26699-26759, 2013.

1576 Kozawa, K.H., Park, S.S., Mara, S.L., and Herner, J.D.: Verifying emission reductions from heavy-duty
1577 diesel trucks operating on southern California freeways, *Environ. Sci. Tech*., Early on-line release,
1578 doi:10.1021/es4044177, 2014.

1579 Laborde, M. Schnaiter, M., Linke, C., Saathoff, H., Naumann, K.-H., Mohler, O., Berlenz, S., Wagner,
1580 U., Taylor, J.W., Liu, D., Flynn, M., Allan, J.D., Coe, H., Heimerl6, K., Dahlko¨tter, F., Weinzier, B.,
1581 Wollny, A.G., Zanatta, M., Cozic, J., Laj, P., Hitzenberger, R., Schwarz, J.P., and Gysel, M.: Single
1582 particle soot photometer intercomparison at the AIDA chamber. *Atmos. Meas. Tech*., 5, 3077-3097,
1583 doi:10.5194/amt-5-3077-2012, 2012.

1584 Lack. D.A., Moosmüller, H., McMeeking, G.R., Chakrabarty, R.K., and Baumgardner, D.: Characterizing
1585 elemental, equivalent black, and refractory black carbon aerosol particles: a review of techniques,
1586 their limitations and uncertainties, *Anal. Bioanal. Chem*., 406, 99-122, doi:10.1007/s00216-013-7402-
1587 3, 2014.

1588 Langford, A.O., Brioude, J., Cooper, O.R., Senff, C.J., Alvarez II, R.J., Hardesty, R.M., Johnson, and
1589 B.J., Oltmans, S.J.: Stratospheric influence on surface ozone in the Los Angeles area during late
1590 spring and early summer of 2010, *J. Geophys. Res*., 117, D00V06, doi:10.1029/2011JD016766, 2012.

1591 Langridge, J.M., Lack, D., Brock, C.A., Bahreini, R., Middlebrook, A.M., Neuman, J.A., Nowak, J.B.,
1592 Perring, A.E., Schwarz, J.P., Spackman, J.R., Holloway, J.S., Pollack, I.B., Ryerson,T.B., Roberts,
1593 J.M., Warneke, C., de Gouw, J.A., Trainer, M.K., and Murphy, D.M.: Evolution of aerosol properties
1594 impacting visibility and direct climate forcing in an ammonia-rich urban environment, *J. Geophys.*
1595 *Res*., 117, D00V11, doi:10.1029/2011JD017116, 2012.

1596 Laskin, A., Moffet, R.C., Gilles, M.K., Fast, J.D., Zaveri, R.A., Wang, B., Nigge, P., and Shuttanandan,
1597 J.: Tropospheric chemistry of internally mixed sea salt and organic particles: Surprising reactivity of
1598 NaCl with weak organic acids, *J. Geophys. Res*., 117, D15302, doi:10.1029/2012JD017743, 2012.

1599 Lawson, D.R., 1990: The southern California air quality study*, J. Air Waste Manage. Assoc*., 40, 156-165.

1600 Lee-Taylor, J., Madronich, S., Aumont, B., Baker, A., Camredon, M., Hodzic, A., Tyndall, G.S., Apel, E.,
1601 and Zaveri, R.A.: Explicit modeling of organic chemistry and secondary organic aerosol partitioning
1602 for Mexico City and its outflow plume, *Atmos. Chem. Phys*., 11, 13219-13241, doi:10.5194/acp-12-
1603 7577-2012, 2011.

1604 Lindinger, W., Hansel, A., and Jordan, A.: On-line monitoring of volatile organic compounds at pptv
1605 levels by means of proton-transfer-reaction mass spectrometry (PTR-MS) – medical applications,
1606 food control and environmental research, *Int. J. Mass Spectrom*., 173, 191–241, 1998.

1607 Liu, S., Alm, L., Day, D.A., Russell, L.M., Zhao, Y., Gentner, D.R., Weber, R.J., Goldstein, A.H., Jaoui,
1608 M., Offenberg, J.H., Kleindienst, T.E., Rubitschun, C., Surratt, J.D., Sheesley, R.J., and Scheller, S.:
1609 Secondary organic aerosol formation from fossil fuel sources contribute majority of summertime
1610 organic mass at Bakersfield, *J. Geophys. Res*., 117, D00V26, doi:10.1029/2012JD018170, 2012.

1611 Liu, Y.J., Herdlinger-Blatt, I., McKinney, K.A., and Martin, S.T.: Production of methyl vinyl ketone and
1612 methacrolein via the hydroperoxyl pathway of isoprene oxidation, *Atmos. Chem. Phys*., 13, 5715-
1613 5730, doi:10.5194/acp-13-5715-2013, 2013.

1614 Lu, R., Turco, R.P., and Jacobson, M.Z.: An integrated air pollution modeling system for urban and
1615 regional scales: 2. Simulations for SCAQS 1987, *J. Geophys. Res*., 102, 6081-6098, 1997.

1616 Malm, W., Sisler, J., Huffman, D., Eldred, R., and Cahill, T.: Spatial and seasonal trends in particle
1617 concentration and optical extinction in the United States, *J. Geophys. Res*., 99, 1347−1370, 1994.

1618 Matsui, H., Koike, M., Kondo, Y., Moteki, N., Fast, J.D., and Zaveri, R.A.: Development and validation
1619 of a black carbon mixing state resolved three-dimensional model: Aging processes and radiative
1620 impact*, J. Geophys. Res*. 118, 2304-2326, doi:10.1029/2012JD018446, 2013.

1621 Meng, Z., D. Dabdub, and J.H. Seinfeld: Size-resolved and chemically resolved model of atmospheric
1622 aerosol dynamics, *J. Geophys. Res*., 103, 3419-3435, 1998.

1623 Metcalf, A.R., Craven, J.S., Ensberg, J.J., Brioude, J., Angevine, W., Sorooshian, A., Duong, H.T.,
1624 Jonsson, H.H., Flagan, R.C., and Seinfeld, J.H.: Black carbon aerosol over the Los Angeles Basin
1625 during CalNex, *J. Geophys. Res.*, 117, D00V13, doi:10.1029/2011JD017255, 2012.

1626 Middlebrook., A.M., Bahreini, R., Jimenez, J.L., and Canagaratna, M.R.: Evaluation of composition-
1627 dependent collection efficiencies for the Aerodyne Aerosol Mass Spectrometer using field data,
1628 *Aerosol Sci. Tech.,* 46, 258-271, doi:10.1080/02786826.2011.620041, 2012.

1629 Moffet, R.C., Rodel, T., Kelly, S., Carroll, G., Fast, J., Zaveri, R., Laskin, A., and Gilles, M.: Spectro-
1630 microscopic studies of carbonaceous aerosol aging in central California, *Atmos. Chem. Phys.* 13,
1631 10445-10459, doi:10.5194/acp-13-10445-2013, 2013.

1632 Moore, R.H., Cerully, K., Bahreini, R., Brock, C.A., Middlebrook, A.M., and Nenes, A.: Hygroscopicity
1633 and composition of California CCN during summer 2010, *J. Geophys. Res*., 117, D00V12,
1634 doi:10.1029/2011JD017352, 2012.

1635 Nilsson, E.D., Rannik, U., Kulmala, M., Buzorius, G., and O'Dowd, C.D.: Effects of continental
1636 boundary layer evolution, convection, turbulence and entrainment, on aerosol formation, *Tellus*, 53,
1637 441-461, doi:10.1034/j.1600-0889.2001.530409.x, 2001.

1638 Peischl, J., Ryerson, T.B., Holloway, J.S., Trainer, M., Andrews, A.E., Atlas, E.L., Blake, D.R., Daube,
1639 B.C., Dlugokencky, E.J., Fischer, M.L., Goldstein, A.H., Guha, A., Karl, T., Kofler, J., Kosciuch, E.,
1640 Misztal, P.K., Perring, A.E., Pollack, I.B., Santoni, G.W., Schwarz, J.P., Spackman, J.R., Wofsy,
1641 S.C., and Parrish, D.D.: Airborne observations of methane emissions from rice cultivation in the
1642 Sacramento Valley of California, *J. Geophys. Res*., 117, D00V25, doi:10.1029/ 2012JD017994, 2012.

1643 Pennington, M.R., Klems, J.P., Bzdek, B.R., and Johnston, M.V.: Nanoparticle chemical composition and
1644 diurnal dependence at the CalNex Los Angeles ground site, *J. Geophys. Res*., 117, D00V10,
1645 doi:10.1029/2011JD017061, 2012.

1646 Perraud, V., Bruns, E.A., Ezell, M.J., Johnson, S.N., Yu, Y., Alexander, M.L., Zelenyuk, A., Imre, D.,
1647 Chang, W.L., Dabdub, D., Pankow, J.F., and Finlayson-Pitts, B.J.: Nonequilibrium atmospheric
1648 secondary organic aerosol formation and growth, *Proc. Natl. Acad. Sci. U.S.A*., 109(8), 2836–2841,
1649 doi:10.1073/pnas.1119909109, 2012.

1650 Pfister, G.G., Parrish, D.D., Worden, H., Emmons, L.K., Edwards, D.P., Wiedinmyer, C., Diskin, G.S.,
1651 Huey, G., Oltmans, S.J., Thouret, V., Weinheimer, A., and Wisthaler, A.: Characterizing summertime
1652 chemical boundary conditions for airmasses entering the US West Coast, *Atmos. Chem. Phys*., 11,
1653 1769–1790, doi:10.5194/acp-11-1769-2011, 2011.

1654 Pollack,, I.B., Ryerson, T.B., Trainer, M., Parrish, D.D., Andrews, A.E., Atlas, E.L., Blake, D.R., Brown,
1655 S.S., Commane, R., Daube, B.C., de Gouw, J.A., Dubé, W.P., Flynn, J., Frost, G.J., Gilman, J.B.,
1656 Grossberg, N., Holloway, J.S., Kofler, J., Kort, E.A., Kuster, W.C., Lang, P.M., Lefer, B., Lueb,
1657 R.A., Neuman, J.A., Nowak, J.B., Novelli, P.C., Peischl, J., Perring, A.E., Roberts, J.M., Santoni, G.,
1658 Schwarz, J.P., Spackman, J.R., Wagner, N.L., Warneke, C., Washenfelder, R.A., Wofsy, S.C., and
1659 Xiang, B.: Airborne and ground-based observations of a weekend effect in ozone, precursors, and
1660 oxidation products in the California South Coast Air Basin, *J. Geophys. Res*., 117, D00V05,
1661 doi:10.1029/2011JD016772, 2012.

1662 Pun, B.K., Balmori, R.T.F., Seigneur, C.: Modeling wintertime particulate matter formation in central
1663 California, *Atmos. Environ*., 43, 402-409, doi:10.1016/j.atmosenv.2008.08.040, 2009.

1664 Qian, Y., Gustafson Jr., W.I., and Fast, J.D.: An investigation of the sub-grid variability of trace gases and
1665 aerosols for global climate models, *Atmos Chem. Phys*., 10, 6917-6946, 2010.

1666 Rollins, A.W., Browne, E.C., Min, K.-E., Pusede, S.E., Wooldridge, P.J., Gentner, D., Goldstein, A.H.,
1667 Liu, S., Day, D.A., Russell, L.M., and Cohen, R.C.: Evidence for NOx control over nighttime SOA
1668 formation, *Science*, 337, 1210-1212, 2012.

1669 Rollins, A.W., Pusede, S.E., Wooldridge, P.J., Min, K.-E., Gentner, D.R., Goldstein, A.H., Liu, S., Day,
1670 D.A., Russell, L.M., Rubitschun, C.L., Surratt, J.D., and Cohen, R.C.: Gas/Particle partitioning of
1671 total alkyl nitrates observed with TD-LIF in Bakersfield, *J. Geophys. Res.,* 118, 6651–6662
1672 doi:10.1002/jgrd.50522, 2013.

1673 Ryerson, T.B., Andrews, A.E., Angevine, W.M., Bates, T.S., Brock, C.A., Cairns, B., Cohen, R.C.,
1674 Cooper, O.R., de Gouw, J.A., Fehsenfeld, R.C., Ferrare, R.A., Fischer, M.L., Flagan, R.C., Goldstein,
1675 A.H., Hair, J.W., Hardesty, R.M., Hostetler, C.A., Jimenez, J.L., Langford, A.O., McCauley, E.,
1676 McKeen, S.A., Molina, L.T., Nenes, A., Oltmans, S.J., Parrish, D.D., Pederson, J.R., Pierce, R.B.,
1677 Prather, K., Quinn, P.K., Seinfeld, J.H., Senff, C.J., Sorooshian, A., Stutz, J., Surratt, J.D., Trainer,

M., Volkamer, R., Williams, E.J., and Wofsy, S.C.: The 2010 California Research at the Nexus of Air Quality and Climate Change (CalNex) field study, *J. Geophys. Res*., 118, 5830-5866, doi:10.1002/jgrd.50331, 2013.

Scarino, A.J., Obland, M.D., Fast, J.D., Burton, S.P., Ferrare, R.A., Hostetler, C.A., Berg, L.K., Lefer, B., Haman, C., Hair, J.W., Rogers, R.R., Butler, C., Cook, A.L., and Harper, D.B.: Comparison of Mixed Layer Heights from Airborne High Spectral Resolution Lidar, Ground-based Measurements, and the WRF-Chem Model during CalNex and CARES, *Atmos. Chem. Phys. Discuss.*, 13, 13721-13772, 2013.

Setyan, A., Zhang, Q., Merkel, M., Knighton, W.B., Sun, Y., Song, C., Shilling, J.E., Onasch, T.B., Herndon, S.C., Worsnop, D.R., Fast, J.D., Zaveri, R.A., Berg, L.K., Wiedensohler, A., Flowers, B.A., Dubey, M.K., and Subramanian, R.: Characterization of submicron particles influenced by mixed biogenic and anthropogenic emissions using high-resolution aerosol mass spectrometry: Results from CARES, *Atmos. Chem. Phys*., 12, 8131-8156, 2012.

Setyan, A., Song, C., Merkel, M., Knighton, W.B., Onasch, T.B., Canagaratna, M.R., Worsnop, D.R., Wiedensohler, A., Shilling, J.E., and Zhang, Q.: Chemistry of new particle growth in mixed urban and biogenic emissions: insights from CARES, *Atmos. Chem. Phys. Discuss*., 14, 2043-2085, doi:10.5194/acpd-14-2043-2014, 2014.

Shilling, J.E., Zaveri, R.A., Fast, J.D., Kleinman, L., Alexander, M.L., Canagaranta, M.R., Fortner, E., Jayne, J.T., Sedlacek, A., Setyan, A., Springston, S., Worsnop, D., and Zhang, Q.: Enhanced SOA formation from mixed anthropogenic and biogenic emissions during the CARES campaign, *Atmos. Chem. Phys.,* 13, 2091-2113, 2013.

Shrivastava, M., Fast, J.D., Easter, R.C., Gustafson Jr., W.I., Zaveri, R.A., Hodzic, A., and Jimenez, J.: Modeling organic aerosols in a megacity: comparison of simple and complex representations of the volatility basis set approach, *Atmos. Chem. Phys.*, 11, 6639-6662, 2011.

Shrivastava, M., Zelenyuk, A., Imre, D., Easter, R., Beranek, J., Zaveri, and R.A., Fast, J.D.: Implications of low volatility SOA and gas-phase fragmentation reactions on SOA loadings and their spatial and temporal evolution in the atmosphere, *J. Geophys. Res*., doi:10.1002/jgrd.50160, 2013.

Skamarock, W.C., Klemp, J.B., Dudhia, J., Gill, D.O., Barker, D.M., Wang, W., and Powers, J.G.: A description of the advanced research WRF version 2, NCAR Technical Note, NCAR/TN-468+STR, 8 pp, Available at *http://wrf-model.org/wrfadmin/publications.php*, 2005.

Spracklen, D.V., Jimenez, J.L., Carslaw, K.S., Worsnop, D.R., Evans, M.J., Mann, G.W., Zhang, Q., Canagaratna, M.R., Allan, J., Coe, H., McFiggans, G., Rap, A., and P. Forster, P.: Aerosol mass spectrometer constraint on the global secondary organic aerosol budget, *Atmos. Chem. Phys*., 11, 12109–12136, doi:10.5194/acp-11-12109-2011, 2011.

Tang, Y., Carmichael, G.R., Uno, I., Woo, J.-H., Kurata, G., Lefer, B., Shetter, R.E., Huang, H., Anderson, B.E., Avery, M.A., Clarke, A.D., and Blake, D.R.: Impacts of aerosols and clouds on photolysis frequencies and photochemistry during TRACE-P: 2. Three-dimensional study using a regional chemical transport model, *J. Geophys. Res*., 108, 8822, doi:10.1029/2002JD003100, 2003.

Thompson, J.E., Hayes , P.L., Jimenez, J.L., Adachi, K., Zhang, X., Liu, J., Weber, R.J, Buseck, P.R.: Aerosol optical properties at Pasadena, CA during CalNex 2010, *Atmos. Environ*., 55, 190-200, doi:10.1016/j.atmosenv.2012.03.011, 2012.

Tsimpidi, A.P., Karydis, V.A., Zavala, M., Lei, W., Molina, L., Ulbrich, I.M., Jimenez, J.L., and Pandis, S.N.: Evaluation of the volatility basis-set approach for the simulation of organic aerosol formation in the Mexico City metropolitan area, *Atmos. Chem. Phys*., 10, 525–546, doi:10.5194/acp-10-525-2010, 2010.

1723 Vaden, T.D., Imre, D., Beranek, J., Shrivastava, M., and Zelenyuk, A.: Evaporation kinetics and phase of
1724 laboratory and ambient secondary organic aerosol, *Proc. Natl. Acad. Sci. U.S.A*., 2190-2195, doi:
1725 10.1073/pnas.1013391108, 2011.

1726 Veres, P.R., Roberts, J.M., Cochran, A.K., Gilman, J.B., Kuster, W.C., Holloway, J.S., Graus, M., Flynn,
1727 J., Lefer, B., Warneke, C., and de Gouw, J.: Evidence of rapid production of organic acids in an urban
1728 air mass, *Geophys. Res. Lett*., 38, L17807, doi:10.1029/2011GL048420, 2011.

1729 Virtanen, A., Joutsensaari, J., Koop, T., Kannosto, J., Yli-Pirilä, P., Leskinen, J., Mäkelä, J.M.,
1730 Holopainen, J.K., Pöschl, U., Kulmala, M., Worsnop, D.R., and Laaksonen, A.: An amorphous solid
1731 state of biogenic secondary organic aerosol particles, *Nature*, 467, 824-827, doi:10.1038/nature09455,
1732 2010.

1733 Volkamer, R., Jimenez, J.L., San Martini, F., Dzepina, K., Zhang, Q., Salcedo, D., Molina, L.T.,
1734 Worsnop, D.R., and Molina, M.J.: Secondary organic aerosol formation from anthropogenic air
1735 pollution: Rapid and higher than expected, *Geophys. Res. Lett*., 33(17), L17811,
1736 doi:10.1029/2006gl026899, 2006.

1737 Vutukuru, S., Griffin, R.J., and Dabdub, D.: Simulation and analysis of secondary organic aerosol
1738 dynamics in the South Coast Air Basin of California, *J. Geophys. Res*., 111, D10S12,
1739 doi:10.1029/2005JD006139, 2006.

1740 Walker, J.M., Philip, S., Martin, R.V., and Seinfeld, J.H.: Simulation of nitrate, sulfate, and ammonium
1741 aerosols over the United States, *Atmos. Chem. Phys*., 12, 11213–11227, doi:10.5194/acp-12-11213-
1742 2012, 2012.

1743 Wang, H., Easter, R.C., Rasch, P.J., Wang, M., Liu, X., Ghan, S.J., Qian, Y., Yoon, J.-H., Ma, P.-L., and
1744 Vinoj, V.: Sensitivity of remote aerosol distributions to representation of cloud–aerosol interactions in
1745 a global climate model, *Geosci. Model Dev*., 6, 765–782, doi:10.5194/gmd-6-765-2013, 2013.

1746 Warneke, C., Veres, P., Holloway, J.S., Stutz, J., Tsai, C., Alvarez, S., Rappenglueck, B., Fehsenfeld,
1747 F.C., Graus, M., Gilman, J.B., and de Gouw, J.A.: Airborne formaldehyde measurements using PTR-
1748 MS: calibration, humidity dependence, inter-comparison and initial results, *Atmos. Meas. Tech.,* 4,
1749 2345-2358, 2011.

1750 Willmott, C.J.: On the validation of models, *Phys.Geogr*., 2, 184-194, 1981.

1751 Wood, E.C., Canagaratna, M.R., Herndon, S.C., Onasch, T.B., Kolb, C.E., Worsnop, D.R., Kroll, J.H.,
1752 Knighton, W.B., Seila, R., Zavala, M., Molina, L.T., DeCarlo, P.F., Jimenez, J.L., Weinheimer, A.J.,
1753 Knapp, D.J., Jobson, B.T., Stutz, J., Kuster, W.C., and Williams, E.J.: Investigation of the correlation
1754 between odd oxygen and secondary organic aerosol in Mexico City and Houston, *Atmos. Chem.*
1755 *Phys*., 10, 8947-8968, doi:10.5194/acp-10-8947-2010, 2010.

1756 Xu, Y., Bahadur, R., Zhao, C., and Leung, L.R.: Estimating the radiative forcing of carbonaceous aerosols
1757 over California based on satellite and ground observations, *J. Geophys. Res*., 118,
1758 doi:10.1002/jgrd.50835, 2013.

1759 Yang, Q., Gustafson Jr., W.I., Fast, J.D., Wang, H., Easter, R.C., Wang, M., Ghan, S.J., Berg, L.K.,
1760 Leung, L.R., and Morrison, H.: Impact of natural and anthropogenic aerosols on stratocumulus and
1761 precipitation in the Southeast Pacific: a regional modelling study using WRF-Chem, *Atmos. Chem.*
1762 *Phys*., 12, 8777-8796, 2012.

1763 Ying, Q., and Kleeman, M.: Regional contributions to airborne particulate matter in central California
1764 during a severe pollution episode, *Atmos. Environ*., 43, 1218-1228,
1765 doi:10.1016/j.atmosenv.2008.11.019, 2009.

1766 Yu, H. Remer, L.A., Chin, M., Bian, H., Tan, Q., Yuan, T., and Zhang, Y.: Aerosols from overseas rival
1767 domestic emissions over North America, *Science*, 337, 566-569. doi:10.1126/science.1217576, 2012.

1768 Zaveri, R.A., Easter, R.C., Fast, J.D., and Peters, L.K.: Model for Simulating Aerosol Interactions and
1769 Chemistry (MOSAIC), *J. Geophysical Research*, 113, D13204, doi:10.1029/2007JD008782, 2008.

1770 Zaveri, R.A., Shaw, W.J., Cziczo, D.J., Schmid, B., Ferrare, R.A., Alexander, M.L., Alexandrov, M.,
1771 Arnott, W.P., Atkinson, D., Barnard, J.C., Berg, L.K., Beranek, J., Brechtel, F., Cahill, J.F., Cairns,
1772 B., Cappa, C.D., China, S., Comstock, J., Dubey, M.K., Easter, R.C., Erickson, M.H., Fast, J.D.,
1773 Floerchinger, C., Flowers, B.A., Fortner, E., Gaffney, J.S., Gilles, M.K., Gorkowski, K., Gustafson,
1774 W.I., Gyawali, M., Hair, J., Harworth, J.W., Herndon, S., Hostetler, C., Hubbe, J.M., Jayne, J.T.,
1775 Jeong, H., Jobson, B.T., Kassianov, E., Kleinman, L.I., Kolesar, K.R., Kluzek, C., Knighton, B.,
1776 Kubátová, A., Kuang, C., Laskin, A., Laulainen, N., Mazzoleni, C., Mei, F., Moffet, R., Nelson, D.,
1777 Obland, M., Onasch, T.B., Ottaviani, M., Pekour, M., Prather, K.A., Radney, J.G., Sedlacek, A.,
1778 Senum, G., Setyan, A., Shilling, J.E., Shrivastava, M., Song, C., Springston, S.R., Subramanian, R.,
1779 Suski, K., Tomlinson, J., Wallace, H.W., Wang, J., Worsnop, D.R., Zelenyuk, A., and Zhang, Q.:
1780 Overview of the 2010 Carbonaceous Aerosols and Radiative Effects Study (CARES), *Atmos. Chem.*
1781 *Phys.*, 12, 7647-7687, 2012.

1782 Zhang, H., DeNero, S.P., Joe, D.K., Lee, H.-H., Chen, S.-H., Michalakes, J., and Kleeman, M.J.:
1783 Development of a source oriented version of the WRF/Chem model and its application to the
1784 California Regional PM10/PM2.5 Air Quality Study, *Atmos. Chem. Phys. Discuss*., 13, 16457-16494,
1785 2013.

1786 Zhang, Y., Pun, B., Vijayaraghavan, K., Wu, S.-Y., Seigneur, C., Pandis, S.N., Jacobson, M.Z., Nenes,
1787 A., and Seinfeld, J.H.: Development and application of the Model of Aerosol Dynamics, Reaction,
1788 Ionization, and Dissolution (MADRID), *J. Geophys. Res*., 109, D01202, doi:10.1029/2003JD003501,
1789 2004.

1790 Zhang, Y., Liu, P., Liu, X.-H., Pun, B., Seigneur, C., Jacobson, M.Z., and Wang, W.-X.: Fine scale
1791 modeling of wintertime aerosol mass, number, and size distributions in central California, *J. Geophys.*
1792 *Res.*, 115, D15207, doi:10.1029/2009JD012950, 2010.

1793 Zhao, C., Leung, L.R., Easter, R., Hand, J., and Avise, J.: Characterization of speciated aerosol direct
1794 radiative forcing over California, *J. Geophys. Res*., 18, 2372-2388, doi:10.1029/2012JD018364, 2013.

1795 Zhao Y., Kreisberg, N.M., Worton, D.R., Isaacman, G., Gentner, D.R., Chan, A.W.H., Weber, R.J., Liu, S.,
1796 Day, D.A., Russell, L.M., Hering, S.V., and Goldstein, A.H.: Sources of organic aerosol investigated
1797 using organic compounds as tracers measured during CalNex in Bakersfield, *J. Geophys. Res*., 18, 1-
1798 11, doi:10.1002/jgrd.50825, 2013.

1799
1800

1801 Table 1. Selected WRF-Chem configuration options used for this study.

Atmospheric Process	Option
Advection	monotonic
Longwave Radiation	RRTMG
Shortwave Radiation	RRTMG
Surface Layer	Monin-Obukhov (Janic) similarity theory
Land Surface	Noah
Boundary Layer	Mellor-Yamada-Janic
Cumulus Convection	Kain-Fritsch
Cloud Microphysics	Morrison
Gas-Phase Chemistry	SAPRC-99
Photolysis	FTUV
Aerosol Chemistry	MOSAIC with volatility basis set (VBS)
Direct Effect	on
Indirect Effect	off

1802
1803

Table 2. Total daily emissions (metric tons) of trace gases and fine particulates (PM2.5) over the modeling domain for weekday and weekend periods derived from the 2008 CARB emission inventory (over California) and the 2005 National Emissions Inventory (elsewhere) as described in the text. VOC are the sum of all non-methane volatile organic compounds and OIN are other inorganic aerosol of unspecified composition.

	CO	**NO_x**	**SO_2**	**NH_3**	**VOC**	**BC**	**OA**	**SO_4**	**NO_3**	**OIN**
weekday	13669.0	3409.3	509.9	803.6	3302.2	56.9	156.1	43.1	1.4	242.4
weekend	14430.9	2031.0	499.7	803.3	3238.5	54.8	123.6	47.2	1.4	237.3

1812 Table 3. Description of simulations performed for this study.

Simulation Name	Description
DEF_ANT	Default configuration that employs the merged CARB 2008 emissions inventory over California and NEI 2005 emissions inventory elsewhere. Biogenic and sea-salt emissions are computed on-line.
50%_ANT	50% reduction of anthropogenic emissions, with the exception of SO_2 and NH_3 that are left unchanged; otherwise identical to DEF_ANT
0%_ANT	no anthropogenic emissions, otherwise identical to DEF_ANT
50%_LBC	50% reduction of aerosols for the initial and boundary conditions, otherwise identical to 50%_ANT

1813
1814

Table 4. Performance of simulated temperature (T), relative humidity (RH), wind speed (WS), and wind direction (WD) in terms of bias, root-mean-square error (RMSE), correlation coefficient (R), and index of agreement (IA) for the surface stations depicted in Fig. 1c. Statistics given for all of California (CA) and by region (Fig. 1c).

Variable	Region	Observed Mean	Bias	RMSE	R	IA
T (K)	CA	289.9	-0.5	3.4	0.90	0.94
	Southern CA	292.0	-0.3	3.5	0.87	0.93
	San Joaquin valley	293.1	-0.2	3.1	0.90	0.95
	Sacramento Valley	292.3	-0.7	3.2	0.89	0.94
	Coastal	287.4	-0.2	3.2	0.86	0.92
	Interior Mountains	288.9	-0.9	3.6	0.92	0.95
RH (%)	CA	55.6	-2.7	17.5	0.76	0.87
	Southern CA	57.7	-7.0	19.2	0.76	0.86
	San Joaquin Valley	49.2	-5.5	14.6	0.79	0.87
	Sacramento Valley	54.3	-0.7	14.0	0.79	0.89
	Coastal	65.9	0.2	17.1	0.72	0.85
	Interior Mountains	47.3	-0.5	17.5	0.74	0.85
WS ($m\ s^{-1}$)	CA	3.0	1.3	2.7	0.57	0.70
	Southern CA	2.6	1.2	2.6	0.58	0.68
	San Joaquin Valley	2.9	1.3	2.5	0.52	0.65
	Sacramento Valley	3.2	1.1	2.4	0.53	0.69
	Coastal	3.0	1.7	3.0	0.56	0.66
	Interior Mountains	3.8	0.7	2.7	0.61	0.77
WD (°)	CA	285.0	-12.7	99.9	0.27	0.77
	Southern CA	15.0	-22.5	121.0	0.23	0.67
	San Joaquin Valley	315.0	-9.7	68.8	0.38	0.81
	Sacramento Valley	255.0	-3.4	90.5	0.34	0.77
	Coastal	285.0	-3.1	75.3	0.27	0.82
	Interior Mountains	15.0	-17.6	114.8	0.20	0.78

Table 5. Performance of simulated temperature (T), relative humidity (RH), wind speed (WS), and wind direction (WD) in terms of bias, root-mean-square error (RMSE), correlation coefficient (R), and index of agreement (IA) for all of the aircraft flight paths and ship track.

	Platform	Number of Data Points	Observed Mean	Bias	RMSE	R	IA
T (K)	G-1	24213	294.7	-2.3	3.53	0.89	0.90
	WP-3D	442273	287.4	-2.9	5.11	0.90	0.92
	CIRPAS Twin Otter	3415	289.3	-3.0	4.21	0.86	0.86
	R/V Atlantis	35489	287.7	1.1	2.68	0.69	0.79
RH (%)	G-1	24041	39.3	0.1	12.90	0.65	0.80
	WP-3D	442273	37.5	-4.0	17.55	0.70	0.82
	CIRPAS Twin Otter	3413	49.2	-5.8	19.88	0.60	0.76
	R/V Atlantis	35489	84.8	-6.6	15.30	0.49	0.66
WS ($m\ s^{-1}$)	G-1	23988	5.4	-0.2	3.80	0.45	0.65
	WP-3D	440073	6.2	-0.1	3.98	0.71	0.83
	R/V Atlantis	35488	4.9	2.0	4.38	0.33	0.58
WD (°)	G-1	23988	195.0	9.6	57.60	0.36	0.84
	WP-3D	440073	315.0	-3.7	68.24	0.27	0.79
	R/V Atlantis	35488	255.0	12.4	72.40	0.23	0.60

Table 6. Performance in simulated wind speed (m s^{-1}) in terms of bias, root-mean-square error (RMSE), correlation coefficient (R), and index of agreement (IA) for the radar wind profilers shown in Fig. 1c. Statistics given for range gates (measurements at discrete altitudes) close to ~250, ~1000, and ~2000 m AGL. Statistics at TRK are not given because relatively little data were available May and June of 2010.

Station	Height (m AGL)	Number of Observations	Observed mean	Bias	RMSE	R	IA
BBY	245	1359	9.4	0.5	3.3	0.79	0.88
BKF	239	1265	2.2	2.3	3.6	0.08	0.34
CCL	253	1294	7.1	1.7	3.5	0.69	0.80
CCO	239	1347	7.3	0.3	4.0	0.54	0.74
GMN	253	622	5.5	6.3	6.0	0.34	0.51
IRV	290	1160	1.4	2.2	2.8	0.36	0.44
LHS	239	1206	5.6	0.1	3.0	0.60	0.77
LVR	271	1379	4.4	2.1	3.4	0.56	0.66
ONT	266	395	2.1	2.1	1.7	0.34	0.52
SAC	220	1370	7.0	0.6	3.0	0.64	0.79
USC	271	1193	3.1	1.2	2.5	0.58	0.71
VIS	271	1381	5.8	1.2	3.4	0.73	0.83
WAP	245	1024	2.7	1.6	2.7	0.52	0.64
BBY	994	630	7.0	0.8	2.3	0.67	0.81
BKF	992	1278	5.0	0.3	2.9	0.43	0.67
CCL	1006	1067	6.5	-0.5	2.8	0.56	0.75
CCO	992	753	7.3	-2.4	3.3	0.34	0.57
GMN	1006	660	8.1	-1.1	4.0	0.29	0.57
IRV	977	1074	3.0	1.2	2.8	0.14	0.44
LHS	992	1160	6.7	-0.5	3.1	0.51	0.71
LVR	1021	1237	6.6	0.3	2.8	0.59	0.77
ONT	1010	402	2.8	0.6	1.4	0.16	0.46
SAC	1021	1059	5.7	-0.2	2.4	0.61	0.78
USC	1021	702	3.6	1.6	2.8	0.33	0.51
VIS	1021	1014	4.8	0.4	2.2	0.58	0.76
WAP	989	908	5.4	1.0	2.9	0.59	0.75
BBY	1983	352	7.9	-0.5	1.5	0.78	0.88
BKF	1954	1302	7.4	-1.0	3.2	0.51	0.70
CCL	1969	946	6.3	-1.6	3.1	0.35	0.59
CCO	1954	702	7.9	-2.5	3.5	0.51	0.66
GMN	1969	475	9.1	-2.4	2.8	0.47	0.66
IRV	2014	629	6.9	-1.0	2.2	0.65	0.80
LHS	1954	1130	7.2	-1.2	2.9	0.56	0.73
LVR	1986	841	7.6	-0.4	2.3	0.67	0.81
ONT	2014	370	6.0	-0.8	1.7	0.55	0.74
SAC	1957	957	7.0	-0.8	2.5	0.61	0.77

USC	2014	367	6.5	-0.3	1.6	0.50	0.72
VIS	2003	962	5.2	-1.0	2.3	0.43	0.65
WAP	2027	821	8.2	-1.4	2.8	0.57	0.74

Table 7. Performance in simulated wind direction (degrees) in terms of bias, root-mean-square error (RMSE), correlation coefficient (R), and index of agreement (IA) for the radar wind profilers shown in Fig. 1c. Statistics given for range gates close to ~250, ~1000, and ~2000 m AGL. Statistics at TRK are not given because relatively little data were available May and June of 2010.

Station	Height (m AGL)	Number of Observations	Observed mean	Bias	RMSE	R	IA
BBY	245	1359	315.0	3.7	44.4	0.37	0.84
BKF	239	1265	285.0	16.3	66.0	0.33	0.81
CCL	253	1294	315.0	1.2	39.6	0.43	0.78
CCO	239	1347	135.0	-2.1	67.0	0.52	0.87
GMN	253	622	345.0	-14.6	71.3	0.07	0.93
IRV	290	1160	165.0	-11.5	70.1	0.33	0.73
LHS	239	1206	345.0	2.6	66.3	0.05	0.88
LVR	271	1379	255.0	17.2	55.3	0.32	0.69
ONT	266	395	255.0	-7.9	71.2	0.25	0.61
SAC	220	1370	255.0	14.4	36.5	0.45	0.84
USC	271	1193	255.0	-21.5	67.5	0.43	0.81
VIS	271	1381	345.0	-0.1	53.2	0.29	0.79
WAP	245	1024	165.0	5.5	65.8	0.43	0.82
BBY	994	630	345.0	4.1	40.6	0.32	0.93
BKF	992	1278	345.0	-1.5	58.5	0.26	0.86
CCL	1006	1067	315.0	7.2	50.2	0.41	0.85
CCO	992	753	165.0	1.4	75.6	0.30	0.83
GMN	1006	660	315.0	-0.9	58.8	0.40	0.91
IRV	977	1074	165.0	16.6	89.0	0.31	0.76
LHS	992	1160	345.0	-0.7	45.6	0.20	0.96
LVR	1021	1237	285.0	7.2	43.0	0.32	0.94
ONT	1010	402	225.0	9.5	81.2	0.46	0.81
SAC	1021	1059	345.0	5.6	56.2	0.31	0.89
USC	1021	702	345.0	-6.1	71.8	0.14	0.89
VIS	1021	1014	345.0	-3.2	52.8	0.28	0.86
WAP	989	908	345.0	4.6	60.3	0.38	0.90
BBY	1983	352	15.0	-6.0	34.8	0.48	0.98
BKF	1954	1302	315.0	0.8	44.3	0.49	0.91
CCL	1969	946	165.0	16.1	65.6	0.34	0.82
CCO	1954	702	165.0	2.9	63.3	0.16	0.85
GMN	1969	475	285.0	-2.5	60.9	0.38	0.87
IRV	2014	629	285.0	-8.3	50.3	0.44	0.91
LHS	1954	1130	345.0	3.0	43.9	0.39	0.93
LVR	1986	841	255.0	3.4	40.0	0.56	0.96
ONT	2014	370	285.0	-8.9	52.2	0.44	0.92
SAC	1957	957	195.0	4.6	43.2	0.60	0.95

USC	2014	367	315.0	-0.8	40.7	0.62	0.95
VIS	2003	962	345.0	7.0	47.9	0.30	0.91
WAP	2027	821	315.0	-3.1	43.9	0.50	0.92

1843
1844

Table 8. Performance of simulated carbon monoxide (CO), nitrogen oxide (NO), nitrogen dioxide (NO_2), sulfur dioxide (SO_2), ozone (O_3), isoprene, methyl-vinyl-ketone + methacrolein (MVK+MACR), toluene, terpene, and formaldehyde over all the G-1 flights in terms of bias, root-mean-square error (RMSE), correlation coefficient (R), and index of agreement (IA)

Trace Gas	Simulation	Number of Data Points	Observed Mean (ppbV)	Bias (ppbv)	RMSE	R	IA
CO	DEF_ANT	22675	140.2	13.9	34.0	0.60	0.71
	50%_ANT			-5.0	22.7	0.62	0.76
	0%_ANT			-24.5	34.7	0.45	0.49
	50%_LBC			-5.1	22.8	0.62	0.76
NO	DEF_ANT	21491	0.42	0.32	1.24	0.54	0.61
	50%_ANT			-0.13	0.66	0.56	0.69
	0%_ANT			-0.40	0.86	0.26	0.33
	50%_LBC			-0.13	0.66	0.56	0.69
NO_2	DEF_ANT	20361	1.05	0.63	2.11	0.57	0.64
	50%_ANT			-0.30	1.17	0.58	0.72
	0%_ANT			-0.99	1.67	0.28	0.39
	50%_LBC			-0.31	1.16	0.59	0.72
SO_2	DEF_ANT	15816	0.59	-0.28	0.77	0.25	0.51
	50%_ANT			-0.28	0.77	0.26	0.51
	0%_ANT			-0.59	0.92	0.12	0.42
	50%_LBC			-0.28	0.77	0.26	0.51
O_3	DEF_ANT	22378	48.1	3.4	12.4	0.77	0.85
	50%_ANT			-2.6	9.9	0.77	0.87
	0%_ANT			-18.9	23.4	0.40	0.51
	50%_LBC			-2.7	10.0	0.77	0.87
isoprene	DEF_ANT	21617	0.53	-0.40	0.94	0.65	0.49
	50%_ANT			-0.36	0.87	0.70	0.61
	0%_ANT			0.10	0.72	0.72	0.84
	50%_LBC			-0.36	0.87	0.70	0.61
MVK+ MACR	DEF_ANT	21636	0.58	-0.37	0.81	0.65	0.53
	50%_ANT			-0.34	0.78	0.68	0.57
	0%_ANT			-0.16	0.68	0.67	0.68
	50%_LBC			-0.34	0.78	0.67	0.57
toluene	DEF_ANT	20470	0.09	0.04	0.15	0.40	0.55
	50%_ANT			-0.03	0.09	0.42	0.64
	0%_ANT			-0.08	0.11	0.35	0.42
	50%_LBC			-0.03	0.09	0.42	0.64
terpene	DEF_ANT	21606	0.07	-0.06	0.09	0.25	0.46
	50%_ANT			-0.05	0.09	0.27	0.48
	0%_ANT			-0.02	0.10	0.32	0.55
	50%_LBC			-0.05	0.09	0.26	0.48

Table 9. Performance of simulated ozone (O_3), carbon monoxide (CO), nitrogen oxide (NO), nitrogen dioxide (NO_2), ammonia (NH_3), sulfur dioxide (SO_2), isoprene, methyl-vinyl-ketone + methacrolein (MVK+MACR), toluene, terpene, and formaldehyde over all the WP-3D flights in terms of bias, root-mean-square error (RMSE), correlation coefficient (R), and index of agreement (IA).

Trace Gas	Simulation	Number of Data Points	Observed Mean (ppbV)	Bias (ppbv)	RMSE	R	IA
CO	DEF_ANT	401896	155.2	17.0	45.6	0.80	0.86
	50%_ANT			-6.3	34.2	0.80	0.86
	0%_ANT			-29.6	60.7	0.27	0.43
	50%_LBC			-6.5	34.3	0.80	0.86
NO	DEF_ANT	370374	0.47	0.36	2.22	0.57	0.67
	50%_ANT			-0.14	1.35	0.59	0.69
	0%_ANT			-0.45	1.73	0.07	0.17
	50%_LBC			-0.14	1.35	0.59	0.69
NO_2	DEF_ANT	356465	1.53	1.28	4.34	0.65	0.72
	50%_ANT			-0.25	2.48	0.65	0.78
	0%_ANT			-1.48	3.52	0.06	0.30
	50%_LBC			-0.25	2.47	0.66	0.78
NH_3	DEF_ANT	301891	5.80	-3.68	15.23	0.47	0.28
	50%_ANT			-3.45	15.10	0.46	0.29
	0%_ANT			-5.82	16.82	0.04	0.21
	50%_LBC			-3.38	15.09	0.46	0.29
SO_2	DEF_ANT	385293	0.46	-0.14	0.91	0.30	0.51
	50%_ANT			-0.28	0.77	0.26	0.51
	0%_ANT			-0.45	0.91	0.06	0.34
	50%_LBC			-0.15	0.89	0.32	0.52
O_3	DEF_ANT	387766	59.0	-5.6	13.2	0.64	0.77
	50%_ANT			-8.8	14.0	0.67	0.73
	0%_ANT			-19.6	24.4	0.40	0.51
	50%_LBC			-8.9	14.0	0.67	0.73
isoprene	DEF_ANT	20380	0.05	-0.01	0.09	0.62	0.78
	50%_ANT			-0.01	0.09	0.57	0.74
	0%_ANT			0.12	0.27	0.43	0.43
	50%_LBC			-0.01	0.09	0.57	0.74
MVK+ MACR	DEF_ANT	1227	0.11	0.05	0.14	0.23	0.44
	50%_ANT			0.04	0.13	0.24	0.44
	0%_ANT			0.05	0.14	0.26	0.49
	50%_LBC			0.04	0.13	0.24	0.45
toluene	DEF_ANT	22350	0.07	0.10	0.25	0.76	0.66
	50%_ANT			0.01	0.10	0.76	0.86
	0%_ANT			-0.06	0.14	0.04	0.34
	50%_LBC			0.01	0.10	0.76	0.86
terpene	DEF_ANT	21654	0.01	-0.01	0.02	0.41	0.47
	50%_ANT			-0.01	0.02	0.26	0.39
	0%_ANT			0.00	0.02	0.28	0.51
	50%_LBC			-0.01	0.02	0.26	0.39

formaldehyde	DEF_ANT	22833	1.92	-0.69	1.04	0.77	0.76
	50%_ANT			-0.88	1.19	0.77	0.69
	0%_ANT			-1.36	1.71	0.62	0.50
	50%_LBC			-0.88	1.19	0.77	0.69

Table 10. Performance of simulated $PM_{2.5}$ at the IMPROVE monitoring sites in terms of bias, root-mean-square error (RMSE), correlation coefficient (R), and index of agreement (IA).

Aerosol Composition	Simulation	Observed Mean ($\mu g\ m^{-3}$)	Bias ($\mu g\ m^{-3}$)	RMSE	R	IA
SO_4	DEF_ANT	0.70	-0.27	0.43	0.63	0.66
	50%_ANT		-0.31	0.47	0.59	0.62
	0%_ANT		-0.42	0.58	0.35	0.50
	50%_LBC		-0.44	0.55	0.65	0.55
NO_3	DEF_ANT	0.48	-0.14	0.56	0.58	0.75
	50%_ANT		-0.33	0.58	0.57	0.65
	0%_ANT		-0.48	0.75	0.04	0.41
	50%_LBC		-0.32	0.57	0.57	0.66
BC	DEF_ANT	0.10	0.02	0.07	0.69	0.81
	50%_ANT		-0.02	0.07	0.64	0.70
	0%_ANT		-0.07	0.11	0.24	0.47
	50%_LBC		-0.04	0.08	0.69	0.66
OC	DEF_ANT	0.68	0.41	0.73	0.74	0.74
	50%_ANT		-0.05	0.38	0.74	0.85
	0%_ANT		-0.51	0.71	0.52	0.48
	50%_LBC		-0.09	0.38	0.74	0.85
seasalt	DEF_ANT	0.34	-0.29	0.99	0.81	0.26
	50%_ANT		-0.29	0.99	0.84	0.27
	0%_ANT		-0.30	0.99	0.88	0.27
	50%_LBC		-0.30	0.98	0.86	0.29
Cl	DEF_ANT	0.19	-0.18	0.58	0.47	0.24
	50%_ANT		-0.18	0.57	0.60	0.24
	0%_ANT		-0.18	0.57	0.79	0.25
	50%_LBC		-0.18	0.56	0.79	0.27
$PM_{2.5}$	DEF_ANT	3.90	0.27	2.23	0.50	0.71
	50%_ANT		-0.83	2.20	0.46	0.62
	0%_ANT		-2.00	3.03	0.08	0.45
	50%_LBC		-1.68	2.58	0.51	0.59
PM10	DEF_ANT	10.19	1.26	7.18	0.37	0.58
	50%_ANT		0.05	7.40	0.31	0.54
	0%_ANT		-1.37	8.02	0.22	0.50
	50%_LBC		-3.26	7.87	0.35	0.59

1868 Table 11. Performance of simulated aerosol composition over all the G-1 flights in terms of bias, root-
1869 mean-square error (RMSE), correlation coefficient (R), and index of agreement (IA).
1870

Aerosol Composition	Simulation	Observed Mean ($\mu g\ m^{-3}$)	Bias ($\mu g\ m^{-3}$)	RMSE	R	IA
SO_4^{2-}	DEF_ANT	0.53	-0.03	0.32	0.45	0.65
	50%_ANT		-0.09	0.34	0.41	0.62
	0%_ANT		-0.28	0.44	0.06	0.44
	50%_LBC		-0.21	0.38	0.43	0.59
NO_3^-	DEF_ANT	0.31	-0.14	0.35	0.30	0.41
	50%_ANT		-0.17	0.37	0.16	0.39
	0%_ANT		-0.29	0.45	-0.14	0.37
	50%_LBC		-0.21	0.39	0.18	0.40
NH_4^+	DEF_ANT	0.16	-0.11	0.23	0.15	0.40
	50%_ANT		-0.14	0.19	0.06	0.42
	0%_ANT		-0.16	0.19	-0.09	0.42
	50%_LBC		-0.14	0.19	0.06	0.42
BC	DEF_ANT	0.07	0.09	0.11	0.54	0.53
	50%_ANT		0.03	0.06	0.55	0.67
	0%_ANT		-0.03	0.07	0.18	0.38
	50%_LBC		0.01	0.05	0.54	0.69
OA	DEF_ANT	4.16	-1.70	3.32	0.76	0.70
	50%_ANT		-2.73	4.23	0.78	0.54
	0%_ANT		-3.75	5.34	0.78	0.44
	50%_LBC		-2.77	4.25	0.78	0.54
Cl	DEF_ANT	0.01	-0.01	0.04	0.07	0.15
	50%_ANT		-0.01	0.04	0.02	0.14
	0%_ANT		-0.01	0.04	0.07	0.18
	50%_LBC		-0.01	0.04	0.03	0.14

1871
1872

Table 12. Performance of simulated aerosol composition over all the WP-3D flights in terms of bias, root-mean-square error (RMSE), correlation coefficient (R), and index of agreement (IA).

Aerosol Composition	Simulation	Observed Mean ($\mu g\ m^{-3}$)	Bias ($\mu g\ m^{-3}$)	RMSE	R	IA
SO_4^{2-}	DEF_ANT	0.75	-0.20	0.47	0.66	0.74
	50%_ANT		-0.24	0.50	0.64	0.71
	0%_ANT		-0.42	0.68	0.39	0.50
	50%_LBC		-0.37	0.57	0.64	0.66
NO_3^-	DEF_ANT	0.71	0.03	1.64	0.57	0.74
	50%_ANT		-0.41	1.53	0.56	0.64
	0%_ANT		-0.69	1.92	0.07	0.28
	50%_LBC		-0.40	1.52	0.57	0.66
NH_4^+	DEF_ANT	0.48	-0.10	0.56	0.66	0.79
	50%_ANT		-0.24	0.59	0.64	0.68
	0%_ANT		-0.44	0.82	0.08	0.38
	50%_LBC		-0.27	0.60	0.65	0.68
BC	DEF_ANT	0.08	0.08	0.15	0.64	0.70
	50%_ANT		0.02	0.09	0.64	0.75
	0%_ANT		-0.03	0.12	0.19	0.37
	50%_LBC		0.00	0.09	0.64	0.76
OA	DEF_ANT	1.74	0.23	1.35	0.71	0.83
	50%_ANT		-0.58	1.47	0.71	0.72
	0%_ANT		-1.31	2.19	0.33	0.48
	50%_LBC		-0.64	1.49	0.72	0.72
Cl	DEF_ANT	0.02	-0.02	0.11	0.17	0.30
	50%_ANT		-0.02	0.11	0.12	0.23
	0%_ANT		-0.02	0.11	0.04	0.16
	50%_LBC		-0.01	0.12	0.08	0.22

Table 13. Performance of simulated aerosol composition over all the CIRPAS Twin Otter flights in terms of bias, root-mean-square error (RMSE), correlation coefficient (R), and index of agreement (IA).

Composition	Simulation	Observed Mean ($\mu g\ m^{-3}$)	Bias ($\mu g\ m^{-3}$)	RMSE	R	IA
SO_4^{2-}	DEF_ANT	0.60	-0.05	0.54	0.16	0.43
	50%_ANT		-0.31	0.57	0.27	0.42
	0%_ANT		-0.10	0.54	0.16	0.43
	50%_LBC		-0.22	0.58	0.11	0.44
NO_3^-	DEF_ANT	1.77	-0.57	2.02	0.49	0.68
	50%_ANT		-1.76	2.76	-0.16	0.41
	0%_ANT		-1.14	2.24	0.43	0.56
	50%_LBC		-1.10	2.20	0.44	0.58
NH_4^+	DEF_ANT	0.96	-0.45	0.85	0.51	0.64
	50%_ANT		-0.96	1.27	0.15	0.43
	0%_ANT		-0.64	0.97	0.47	0.54
	50%_LBC		-0.66	0.98	0.47	0.54
BC	DEF_ANT	0.05	0.19	0.26	0.41	0.36
	50%_ANT		-0.02	0.09	-0.15	0.24
	0%_ANT		0.08	0.13	0.39	0.51
	50%_LBC		0.07	0.12	0.41	0.54
OA	DEF_ANT	1.81	0.21	0.99	0.70	0.83
	50%_ANT		-1.65	2.02	0.53	0.45
	0%_ANT		-0.52	1.00	0.70	0.78
	50%_LBC		-0.54	1.02	0.70	0.78
Cl	DEF_ANT	0.12	-0.10	0.16	0.02	0.38
	50%_ANT		-0.09	0.15	0.12	0.41
	0%_ANT		-0.11	0.16	-0.01	0.38
	50%_LBC		-0.11	0.16	0.01	0.39

Table 14. Performance of simulated $PM_{2.5}$ for all the surface operational monitoring sites in terms of bias, root-mean-square error (RMSE), correlation coefficient (R), and index of agreement (IA).

Region	Simulation	Observed Mean ($\mu g\ m^{-3}$)	Bias ($\mu g\ m^{-3}$)	RMSE	R	IA
CA	DEF_ANT	8.4	-2.8	7.0	0.45	0.58
	50%_ANT		-4.4	7.9	0.44	0.48
	0%_ANT		-6.3	9.5	0.13	0.42
Southern CA	DEF_ANT	11.8	-4.5	8.1	0.48	0.60
	50%_ANT		-6.8	9.7	0.44	0.50
	0%_ANT		-9.51	12.2	-0.04	0.43
San Joaquin	DEF_ANT	7.7	-1.5	5.1	0.46	0.63
	50%_ANT		-3.6	6.0	0.43	0.51
	0%_ANT		-5.6	7.7	0.08	0.44
Sacramento Valley	DEF_ANT	4.8	0.1	3.7	0.32	0.52
	50%_ANT		-1.3	3.8	0.30	0.43
	0%_ANT		-2.7	4.7	0.08	0.42
Coastal	DEF_ANT	6.5	-3.0	7.2	0.09	0.34
	50%_ANT		-3.7	7.5	0.11	0.36
	0%_ANT		-4.6	8.0	0.23	0.37
Interior Mountains	DEF_ANT	6.3	-2.2	8.2	0.16	0.31
	50%_ANT		-3.2	8.5	0.15	0.30
	0%_ANT		-4.1	8.9	0.07	0.31

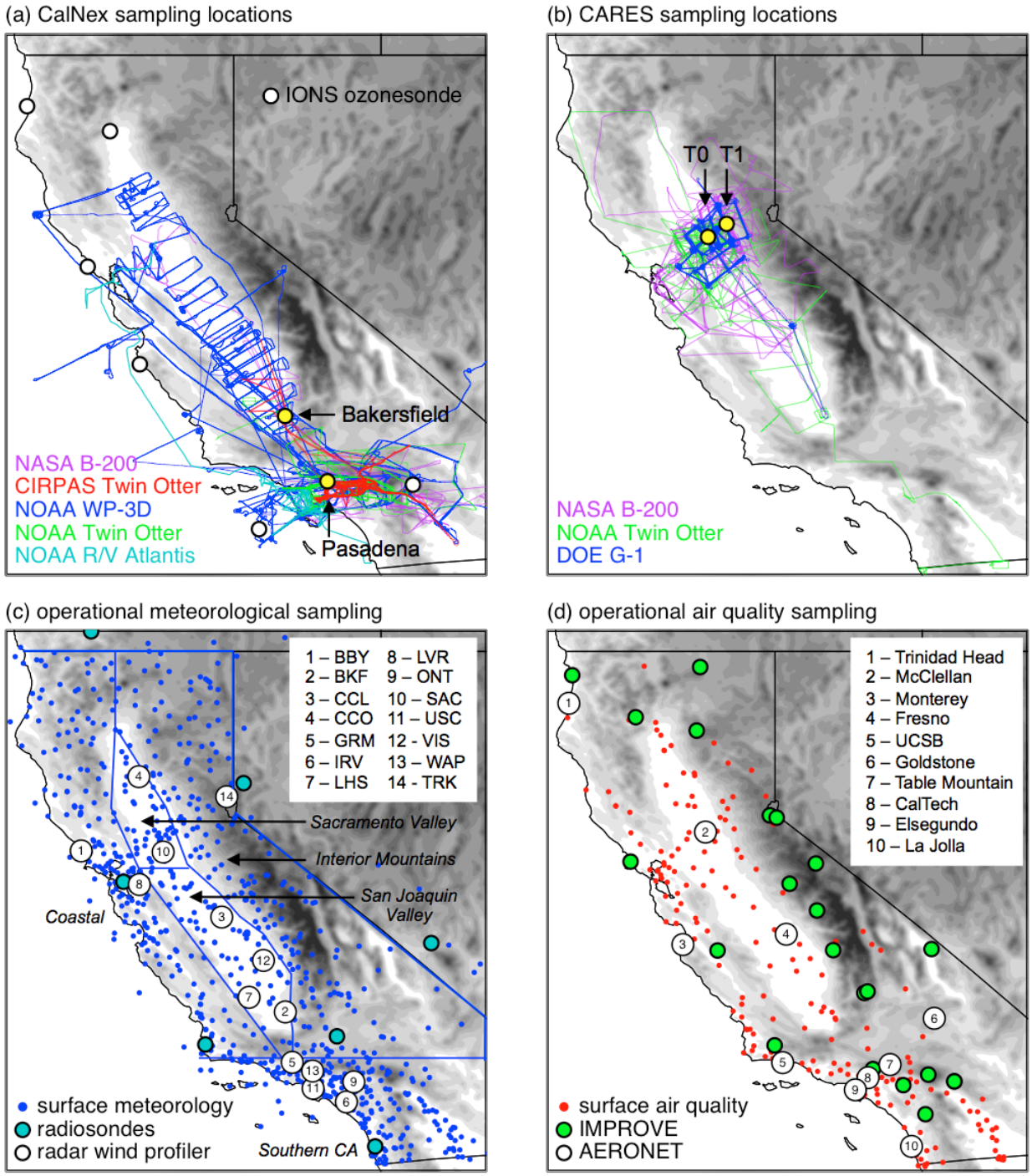

Figure 1. Geographic distributions of fixed and mobile sampling during the (a) CalNex and (b) CARES campaigns along with operational (c) meteorological and (d) air quality sampling sites. Yellow circle in (a) and (b) denote measurement supersites while blue lines in (c) denote geographic regions to compute statistics. Gray shading denotes model topography using Δx = 4 km. The modeling domain extends ~150 km west of the western boundary shown above. BBY= Bodega Bay, BKF=Bakersfield, CCL = Chowchilla, CCO = Chico, GRM = Gorman, IRV = Irvine, LHS = Lost Hills, LVR = Livermore, ONT = Ontario, SAC = Sacramento,

USC = University of Southern California, VIS = Visalia, WAP = Whiteman Airport Pacomia, TRK = Truckee.

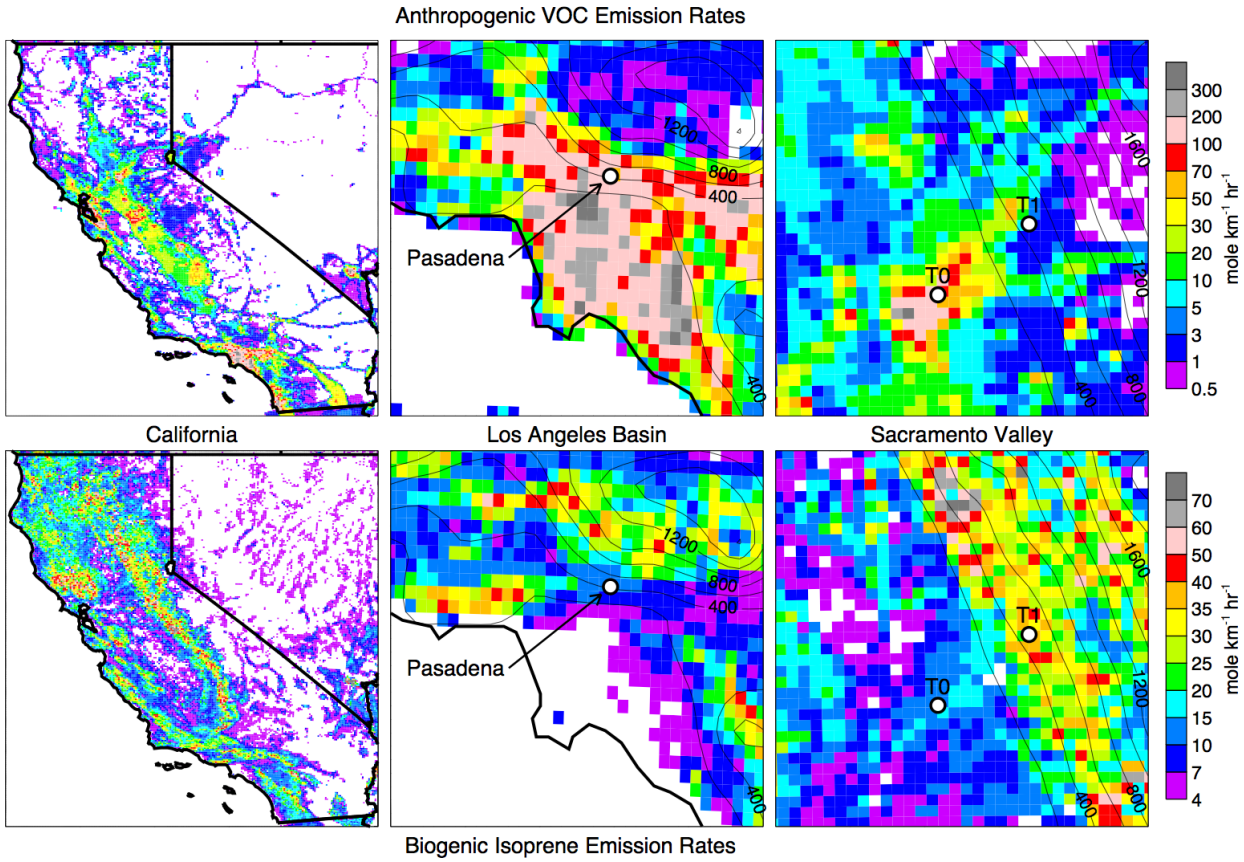

Figure 2. Spatial distribution of anthropogenic VOC (top) and biogenic isoprene (bottom) emission rates for a representative day at 10 LST over California and in the vicinity of the Pasadena, T0, and T1 supersites (white dots). The middle panels depict the Los Angeles Basin and the right panels depict a portion of the Sacramento Valley. Contours denote model topography (m) and regions that are not shaded denote low emission rates.

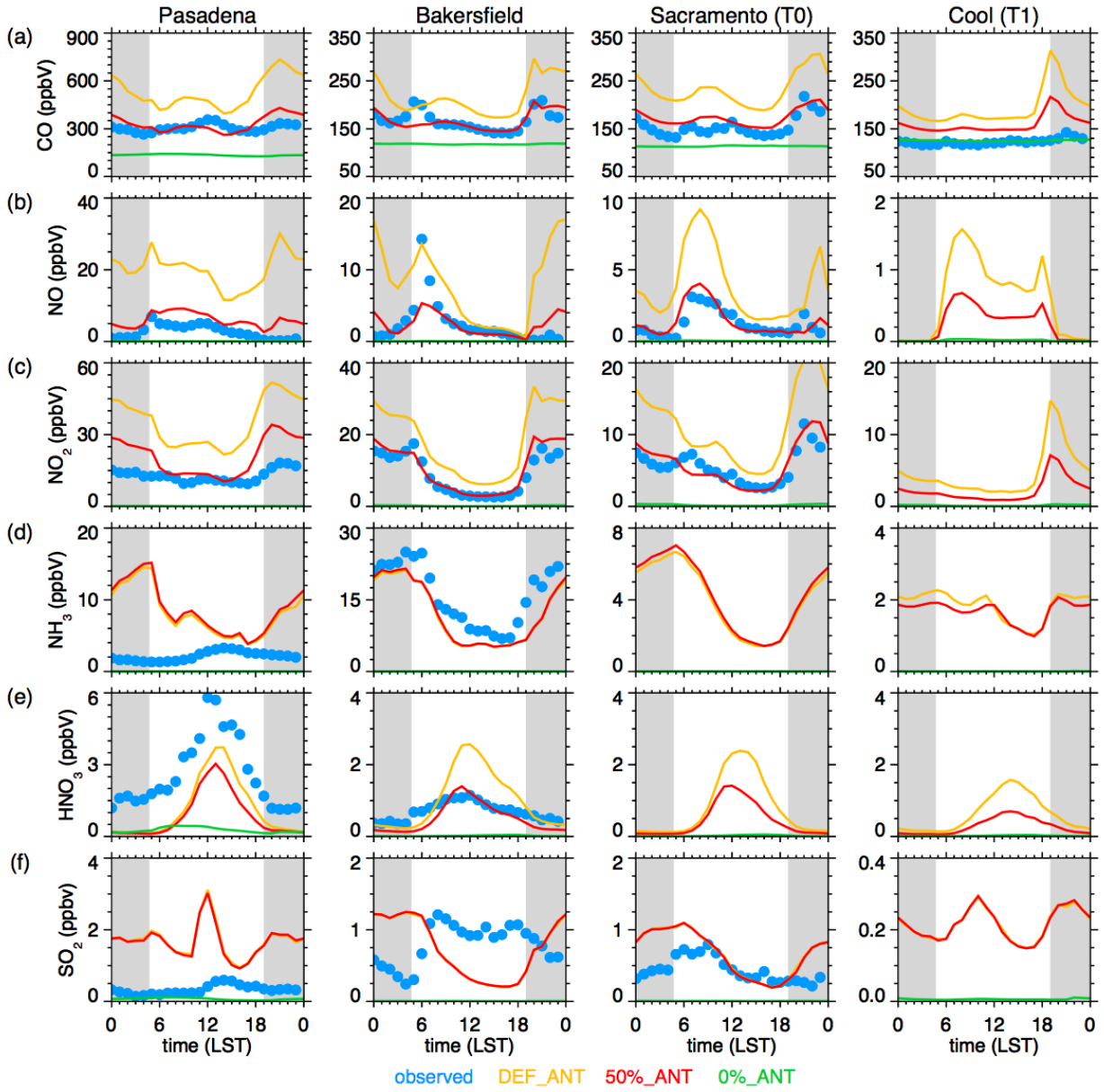

Figure 3. Observed and simulated diurnally-averaged (a) carbon monoxide (CO), (b) nitrogen oxide (NO), (c) nitrogen dioxide (NO_2), (d) ammonia (NH_3), (e) nitric acid (HNO_3), and (f) sulfur dioxide (SO_2) over the 2-month period at the Pasadena, Bakersfield, T0, and T1 supersites. Gray shading denotes night. Missing observations indicate measurements were not collected at a particular site. 50%_LBC simulation results not shown since they are nearly identical to those from the 50%_ANT simulation.

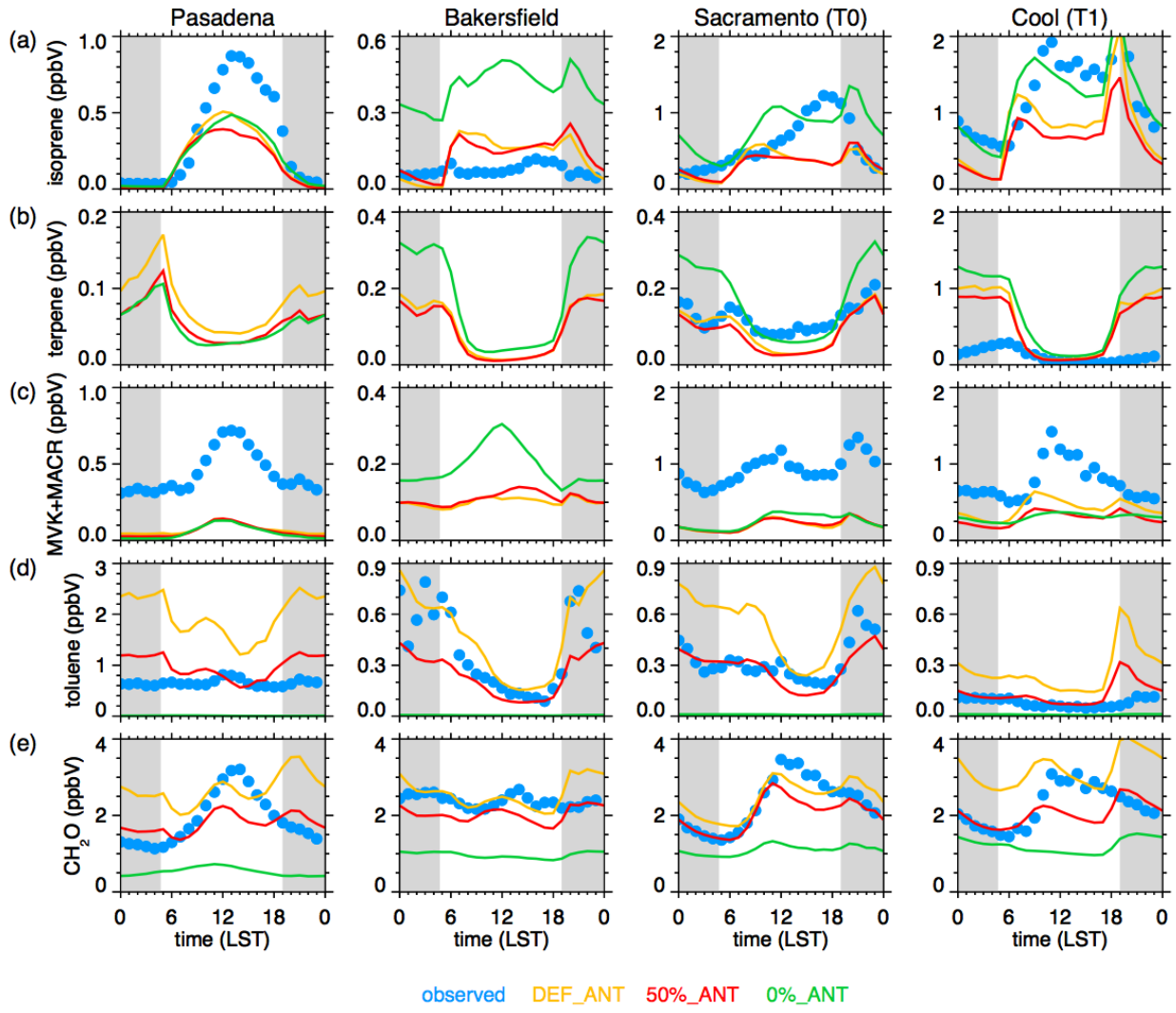

Figure 4. Observed and simulated diurnally-averaged (a) isoprene, (b) terpene, (c) methyl-vinyl-ketone + methacrolein (MVK+MACR), (d) toluene, and (e) formaldehyde (CH_2O) over the 2-month period at the Pasadena, Bakersfield, T0, and T1 supersites. Gray shading denotes night. Missing observations indicate measurements were not collected at a particular site. 50%_LBC simulation results not shown since they are nearly identical to those from the 50%_ANT simulation.

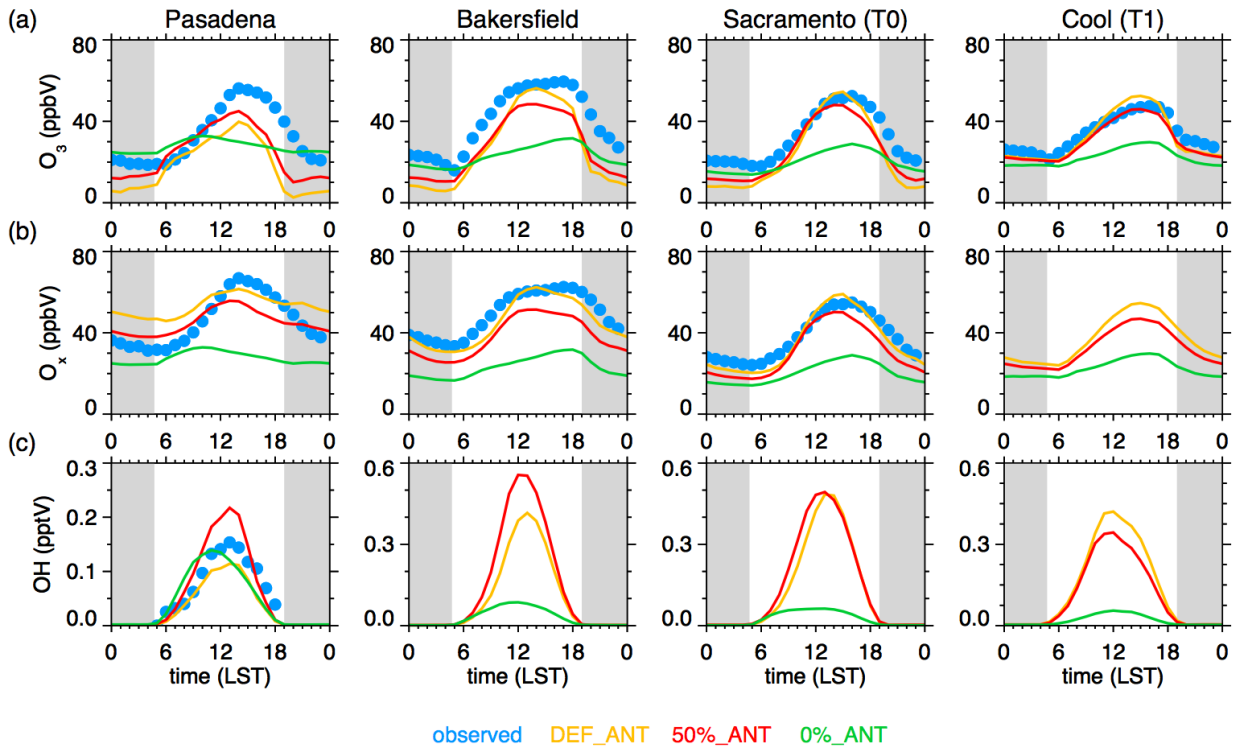

Figure 5. Observed and simulated diurnally-averaged (a) ozone (O_3), (b) Ox (O_3 +NO_2) and (c) OH over the 2-month period at the (a) Pasadena, Bakersfield, T0, and T1 supersites. Gray shading denotes night. 50%_LBC simulation results not shown since they are nearly identical to those from the 50%_ANT simulation. NO_2 not measured at T1, OH not yet available at Bakersfield, and OH not measured at T0 and T1.

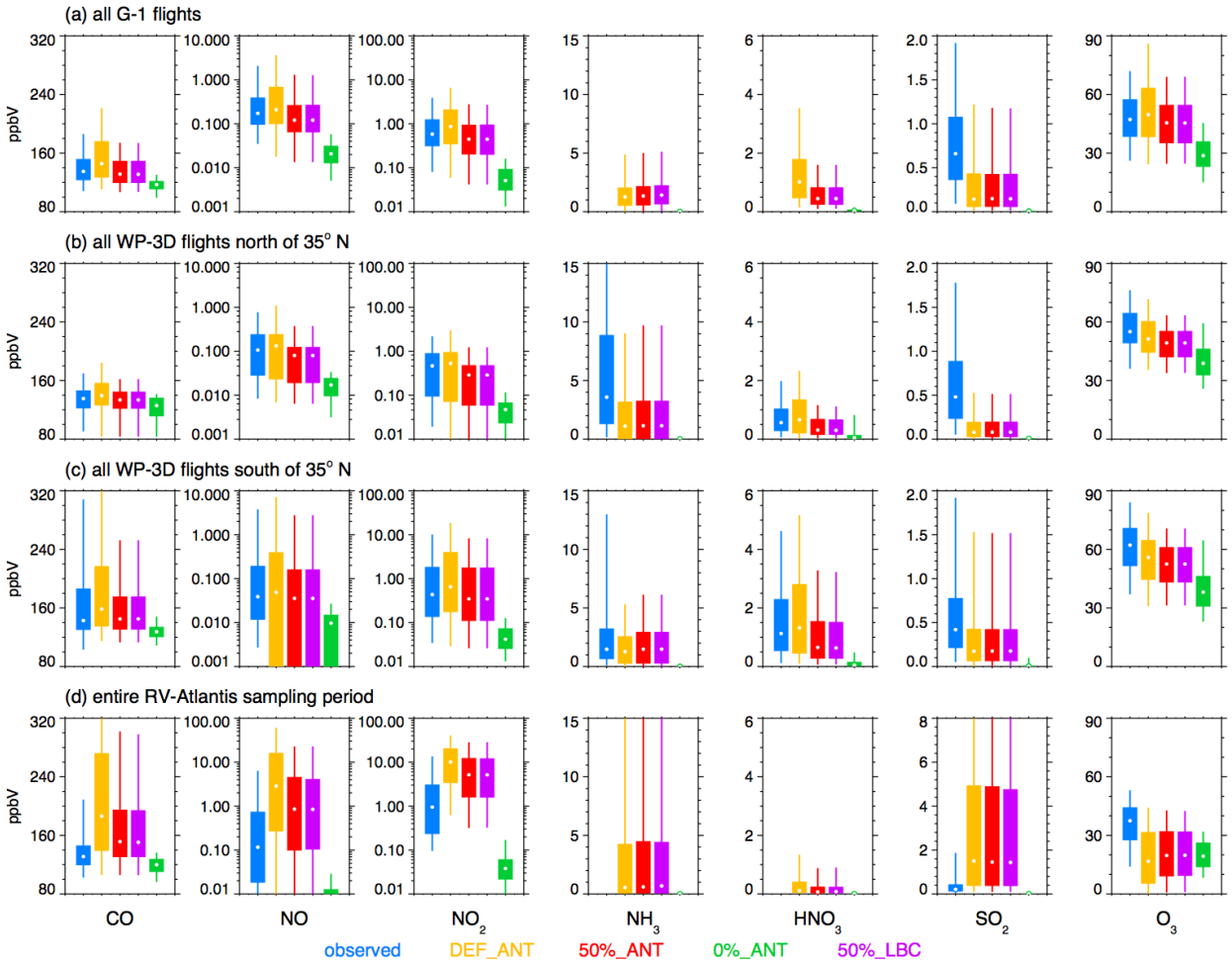

Figure 6. Percentiles for carbon dioxide (CO), nitrogen oxide (NO), nitrogen dioxide (NO_2), ammonia (NH_3), nitric acid (HNO_3), sulfur dioxide (SO_2), and ozone (O_3) for all (a) G-1 flights, (b) WP-3D flights north of 35 N, (c) WP-3D flight flights south of 35 N, and (d) the entire RV-Atlantis sampling period. Vertical lines denote 5th and 95th percentiles, boxes denote 25th and 75th percentiles, and the white dots denote the 50th percentiles. Note that NH_3 was not measured on the G-1 or the RV-Atlantis, but the model results are included for completeness.

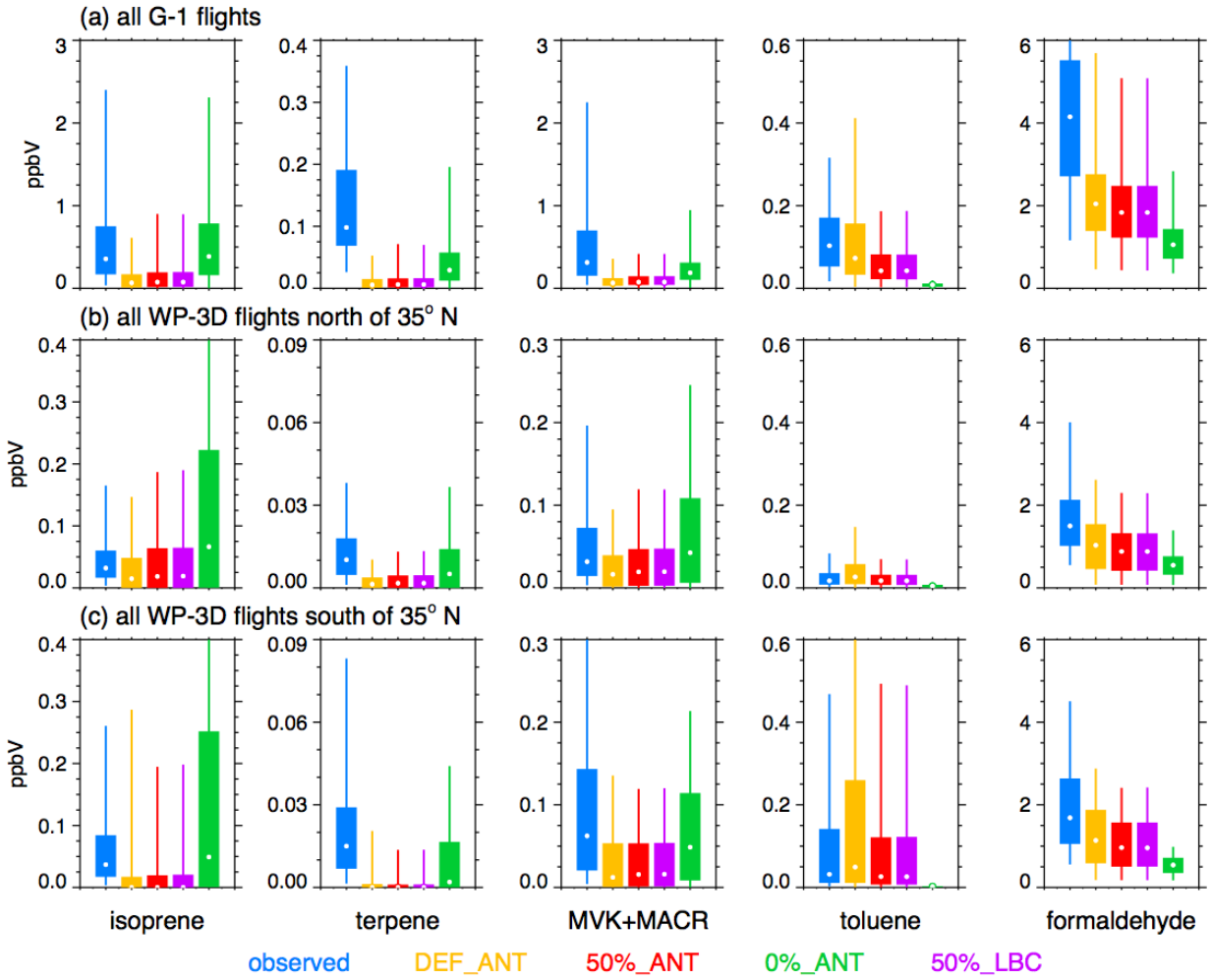

Figure 7. Percentiles as a function of height for isoprene, monoterpenes, methyl-vinyl-ketone + methacrolein (MVK+MACR), toluene, and formaldehyde for all (a) G-1 flights (b) WP-3D flights north of 35 N, and (c) WP-3D flight flights south of 35 N. Vertical lines denote 5th and 95th percentiles, boxes denote 25th and 75th percentiles, and the white dots denote the 50th percentiles. Note that formaldehyde was not measured on the G-1, but the model results are included for completeness.

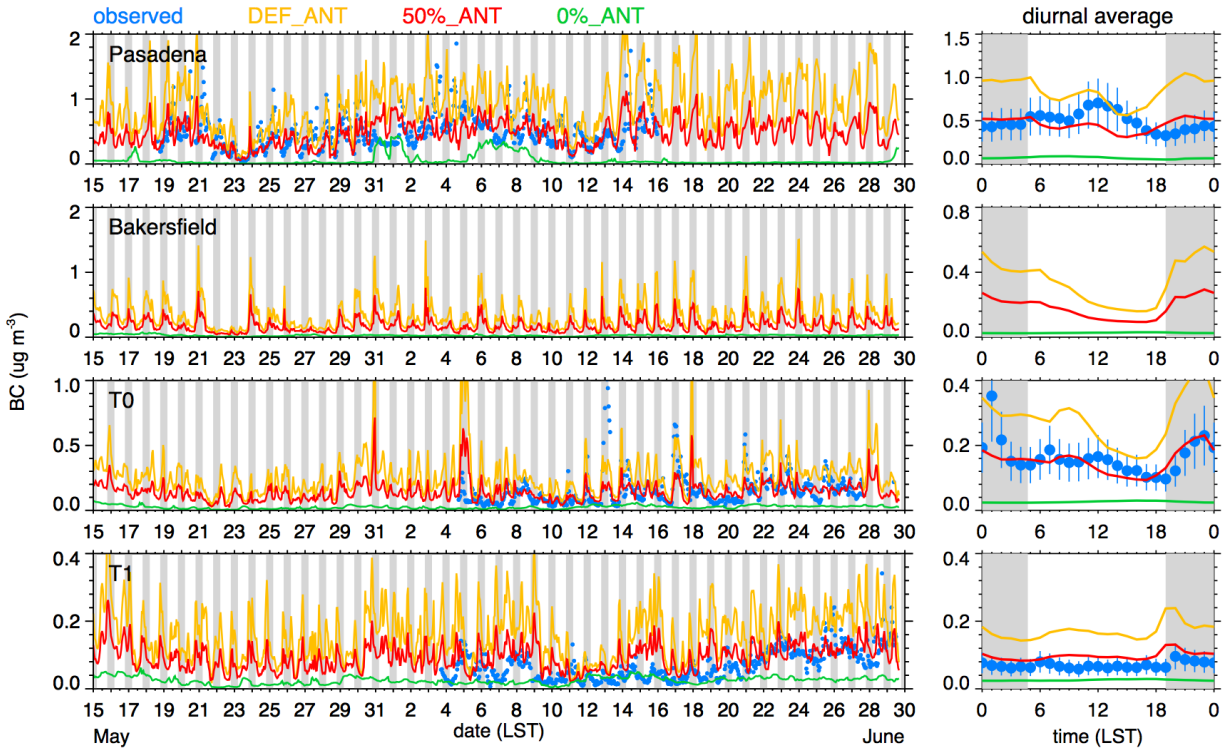

Figure 8. Observed and simulated time series (left panels) and average diurnal variation (right panels) of BC at the four supersites. Simulated BC is the total of the first four model size bins (i.e., aerosol diameters up to 0.625 μm). Gray shading denotes night and vertical lines in right panels denote measurement uncertainty range. Results from 50%_LBC simulation not shown since it is nearly the same as the 50%_ANT simulation. Bakersfield results shown for completeness even though no BC measurements were made at that site.

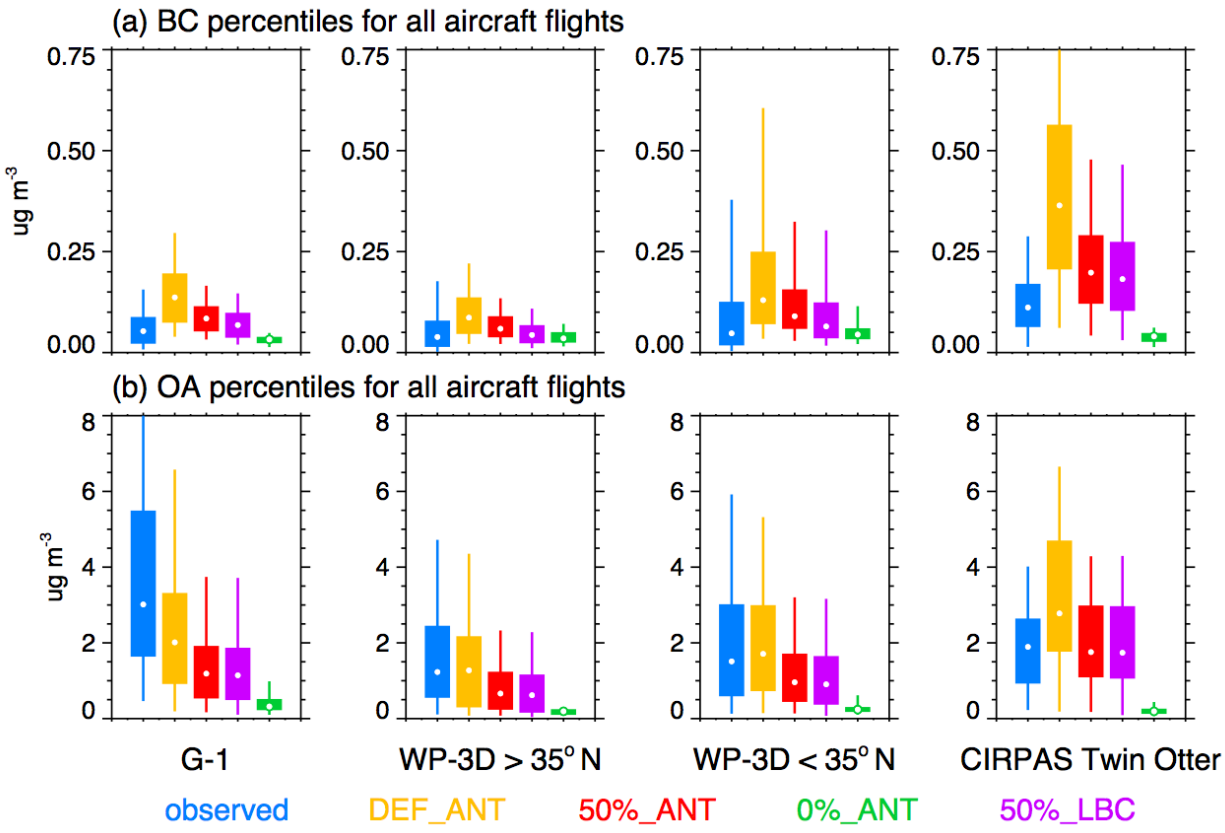

Figure 9. Percentiles for (a) black carbon (BC) and (b) organic matter (OA) for all G-1, WP-3D, and CIRPAS Twin Otter flights. Vertical lines denote 5th and 95th percentiles, boxes denote 25th and 75th percentiles, and the white dots denote the 50th percentiles.

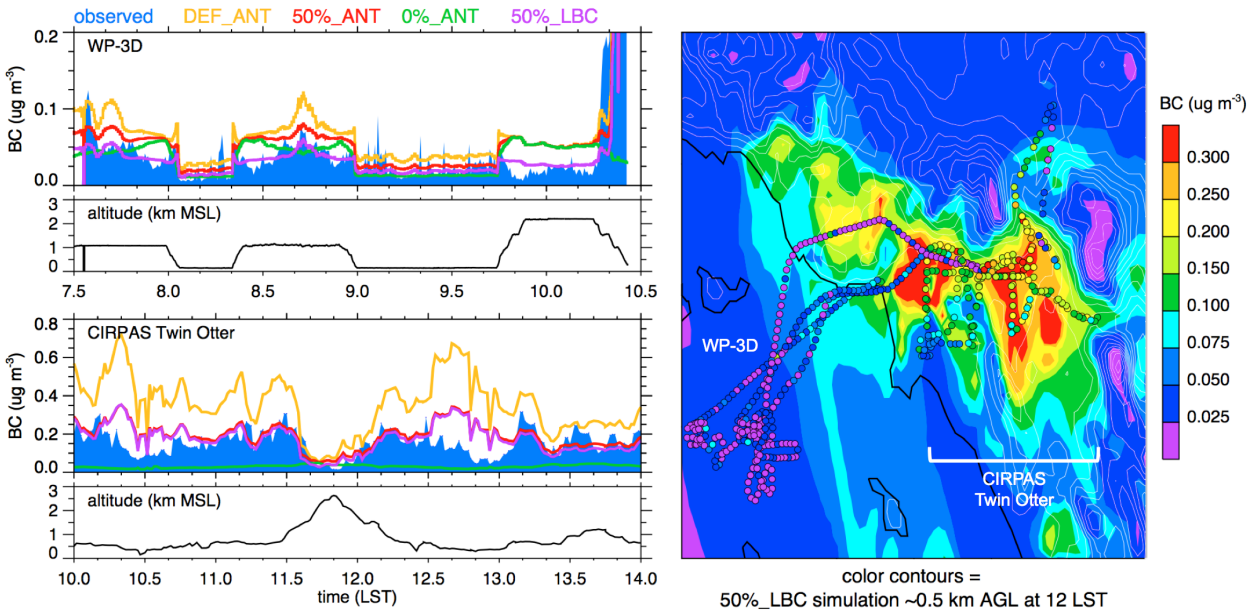

Figure 10. Observed and simulated BC on May 21, 2010 along the WP-3D and CIRPAS Twin Otter flight paths (left panels) and spatial variations in observed BC (right panel). Gray contour lines in right panel denote model topography.

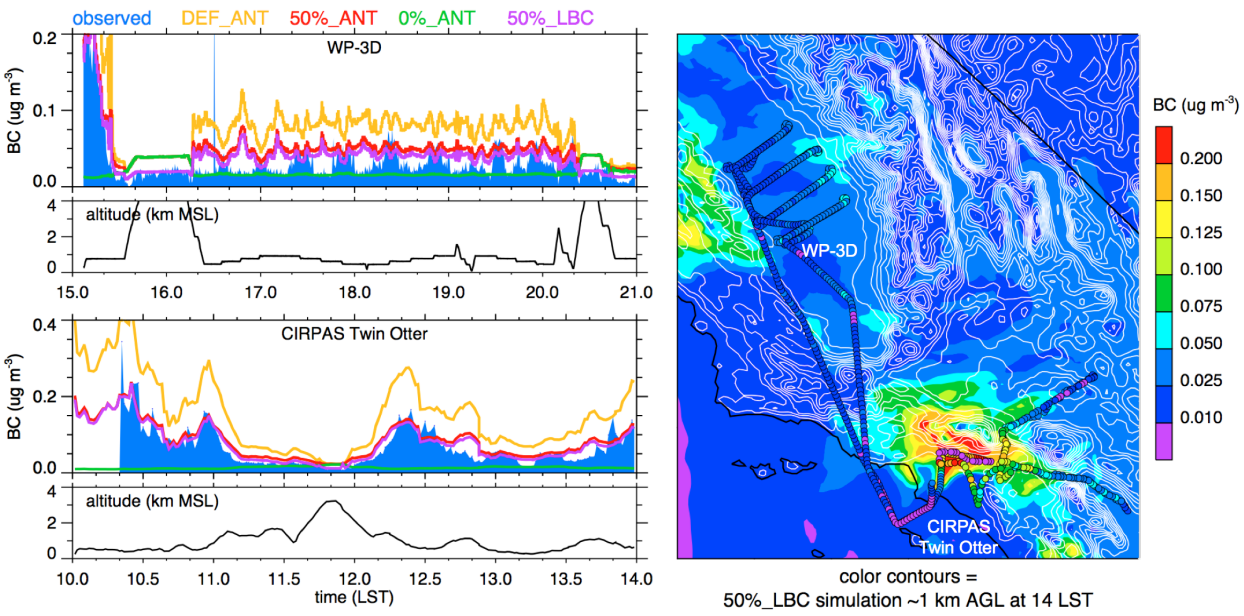

Figure 11. Same as Figure 10, except for May 24, 2010.

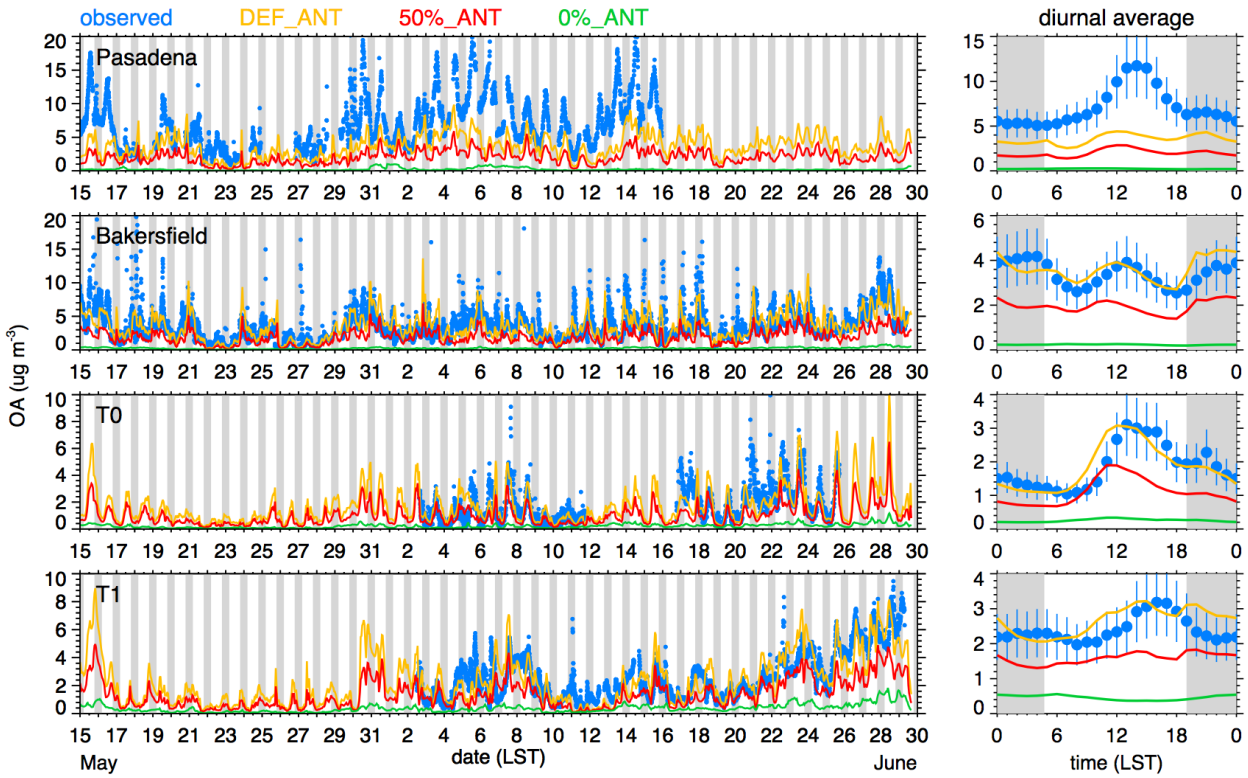

Figure 12. Observed (AMS instrument) and simulated time series (left panels) and average diurnal variation (right panels) of OA at the four supersites. Simulated OA is the total of the first four model size bins up to 0.625 μm diameter. Gray shading denotes night and vertical lines in right panels denote measurement uncertainty range. 50%_LBC simulation results not shown since they are nearly identical to those from the 50%_ANT simulation.

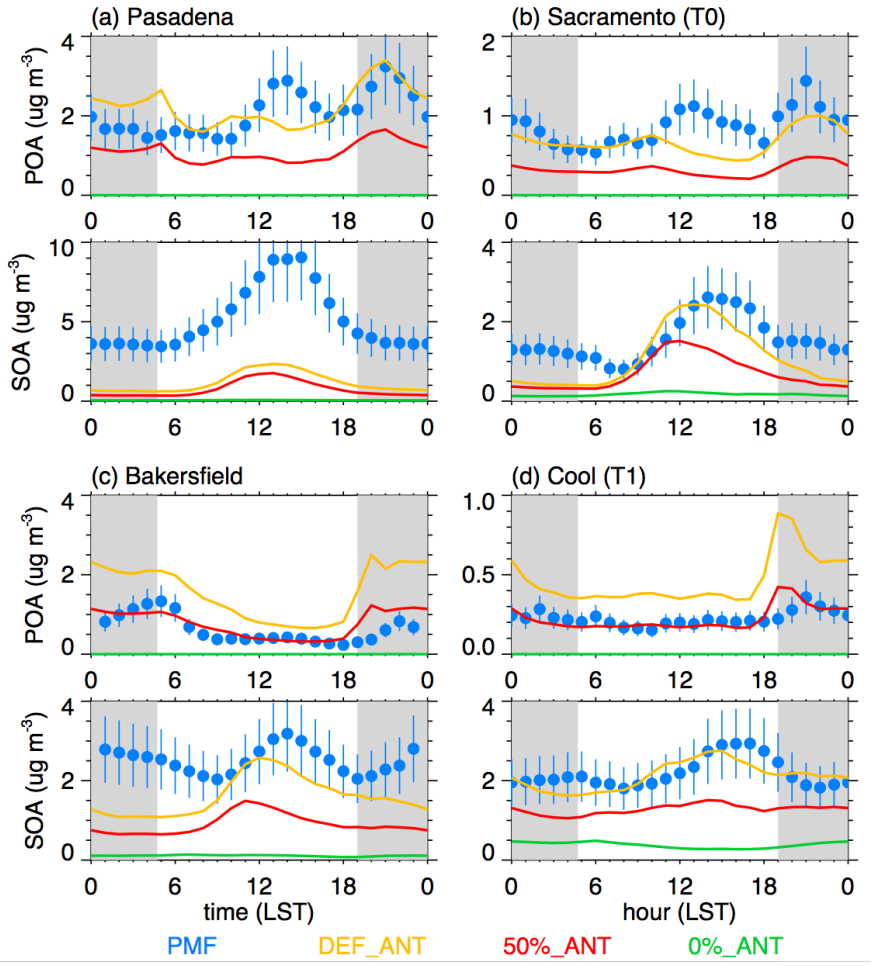

Figure 13. Diurnal averages of primary and secondary organic aerosol components at the (a) Pasadena, (b) T0, (c) Bakersfield, (d) T1 sites. Blue dots denote values derived from AMS measurements using Positive Matrix Factorization (PMF) techniques. Simulated POA and SOA are the total of the first four model size bins up to 0.625 μm diameters. Gray shading denotes night and vertical lines in right panels denote measurement uncertainty range. 50%_LBC simulation results not shown since they are nearly identical to those from the 50%_ANT simulation

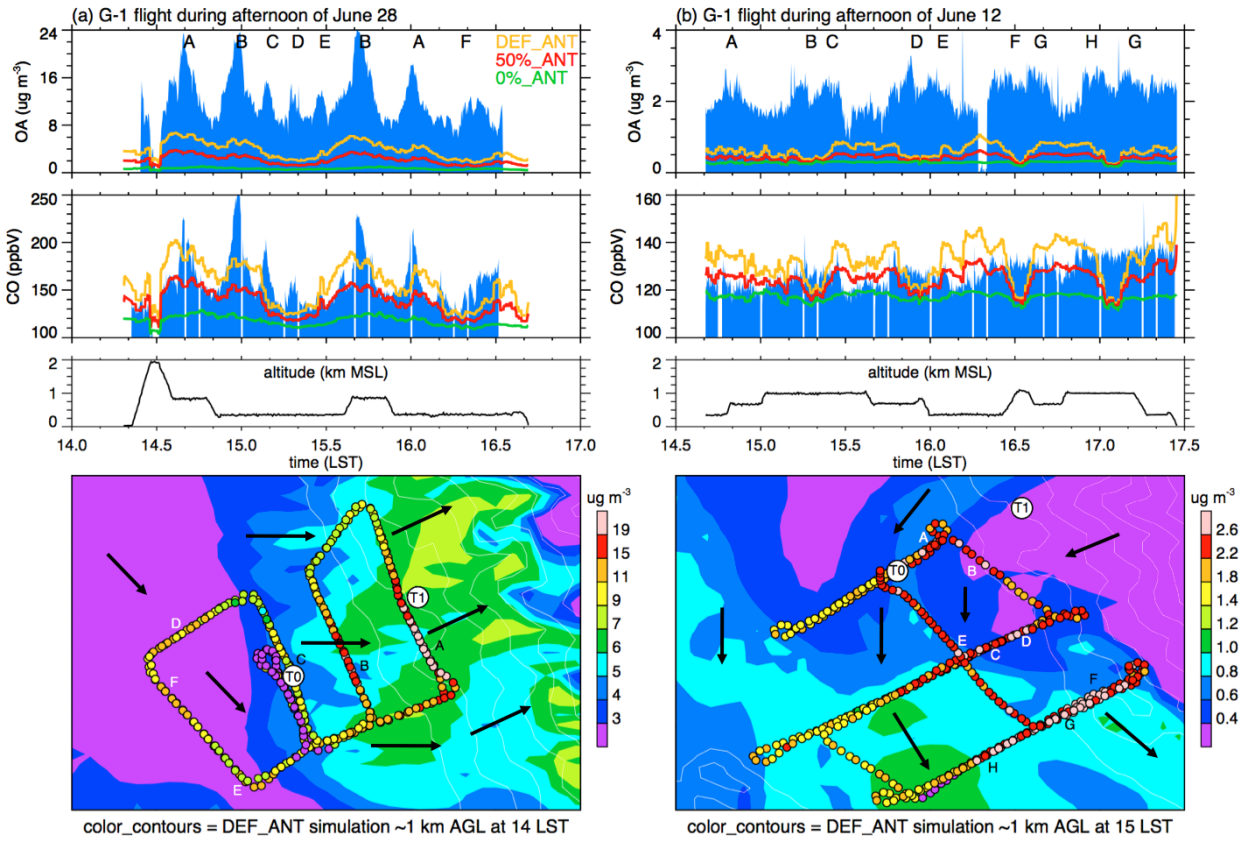

Figure 14. Observed and simulated OA during CARES in the vicinity of Sacramento for the afternoon of (a) June 28 and (b) June 12. (a) and (b) represent days with high and low observed OA, respectively. Simulated OA is the total of the first four model size bins up to 0.625 μm diameter.

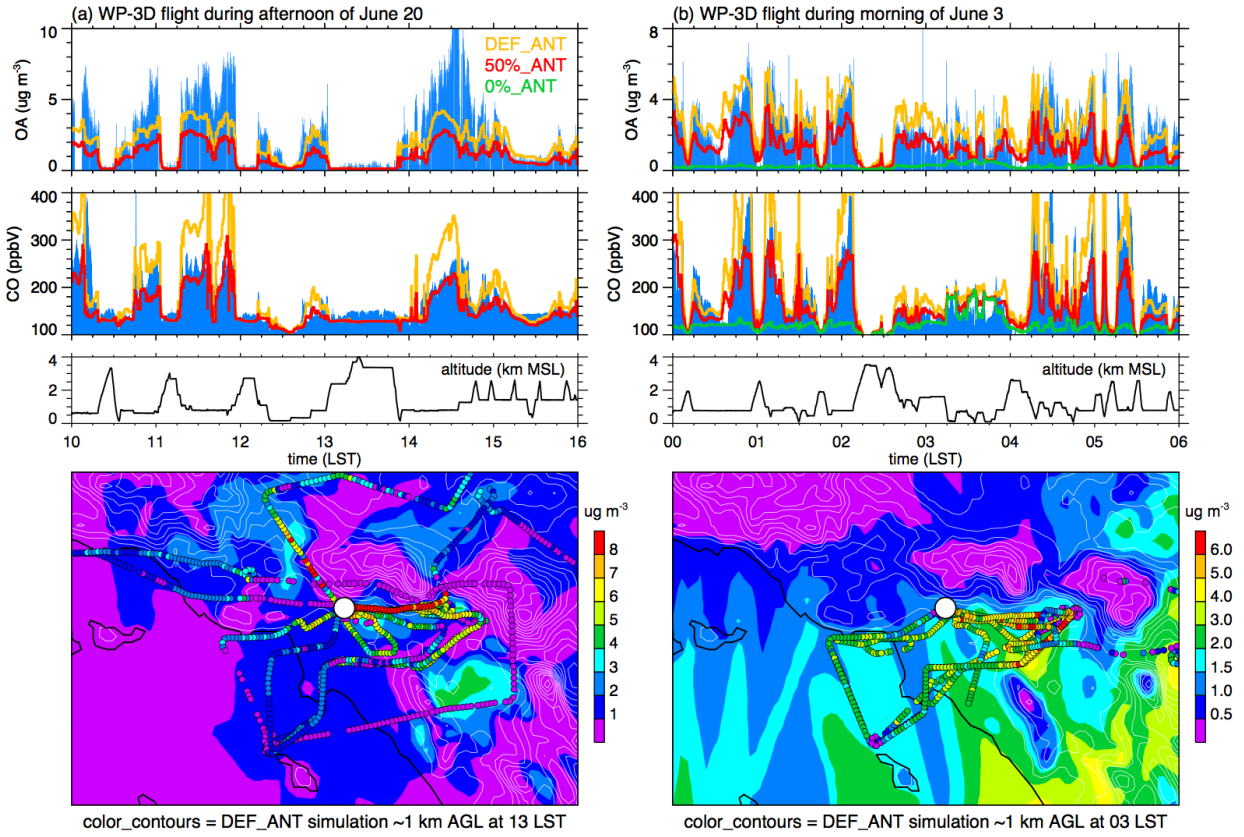

Figure 15. Observed and simulated OA during CalNex in the vicinity of Los Angeles during (a) the afternoon of June 20 and (b) the morning of June 3. (a) and (b) represent days with high and low observed OA, respectively. The white dot denotes the location of the Pasadena supersite. Simulated OA is the total of the first four model size bins up to 0.625 μm diameter.

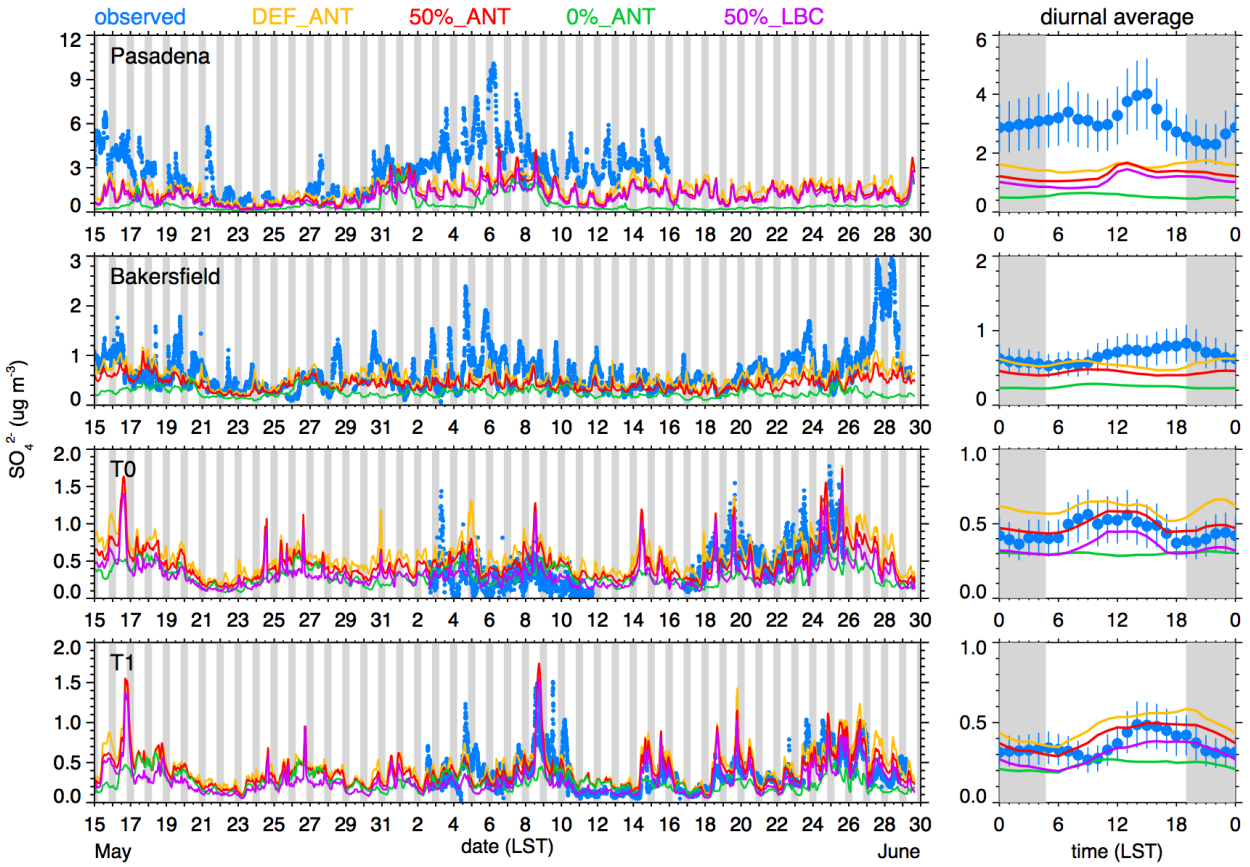

Figure 16. Observed and simulated time series (left panels) and average diurnal variation (right panels) of SO_4^{2-} at the four supersites. Simulated SO_4^{2-} is the total of the first four model size bins up to 0.625 μm diameter. Gray shading denotes night and vertical lines in right panels denote measurement uncertainty range.

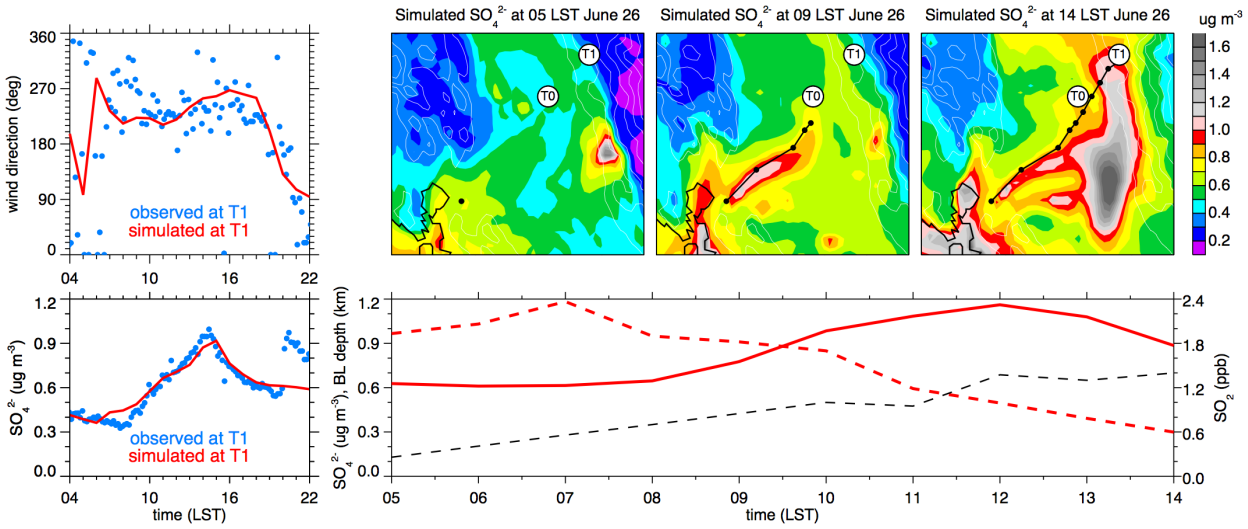

Figure 17. Observed and simulated time series of wind direction and SO_4^{2-} (left panels), near-surface SO_4^{2-} distributions between the San Francisco Bay area and the T1 site at 5, 9, and 14 LST and one air mass trajectory that arrives at the T1 site at 14 LST during the peak afternoon SO_4^{2-} concentration (upper right panels), and evolution of SO_4^{2-}, SO_2, and boundary layer (BL) height along the trajectory (lower right panel).

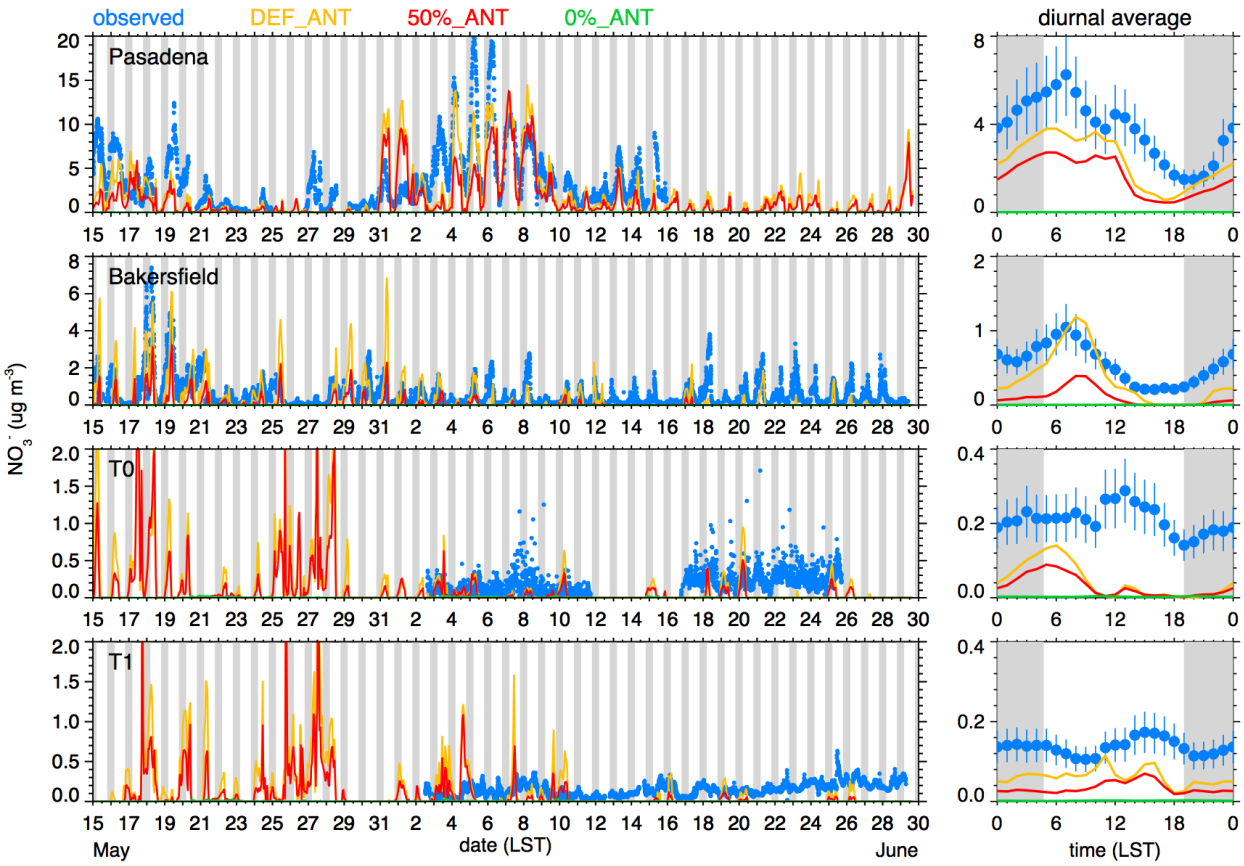

Figure 18. Observed and simulated time series (left panels) and average diurnal variation (right panels) of NO_3^- at the four supersites. Simulated NO_3^- is the total of the first four model size bins up to 0.625 μm diameter. Gray shading denotes night and vertical lines in right panels denote measurement uncertainty range. Results from 50%_LBC simulation not shown since it is nearly the same as the 50%_ANT simulation.

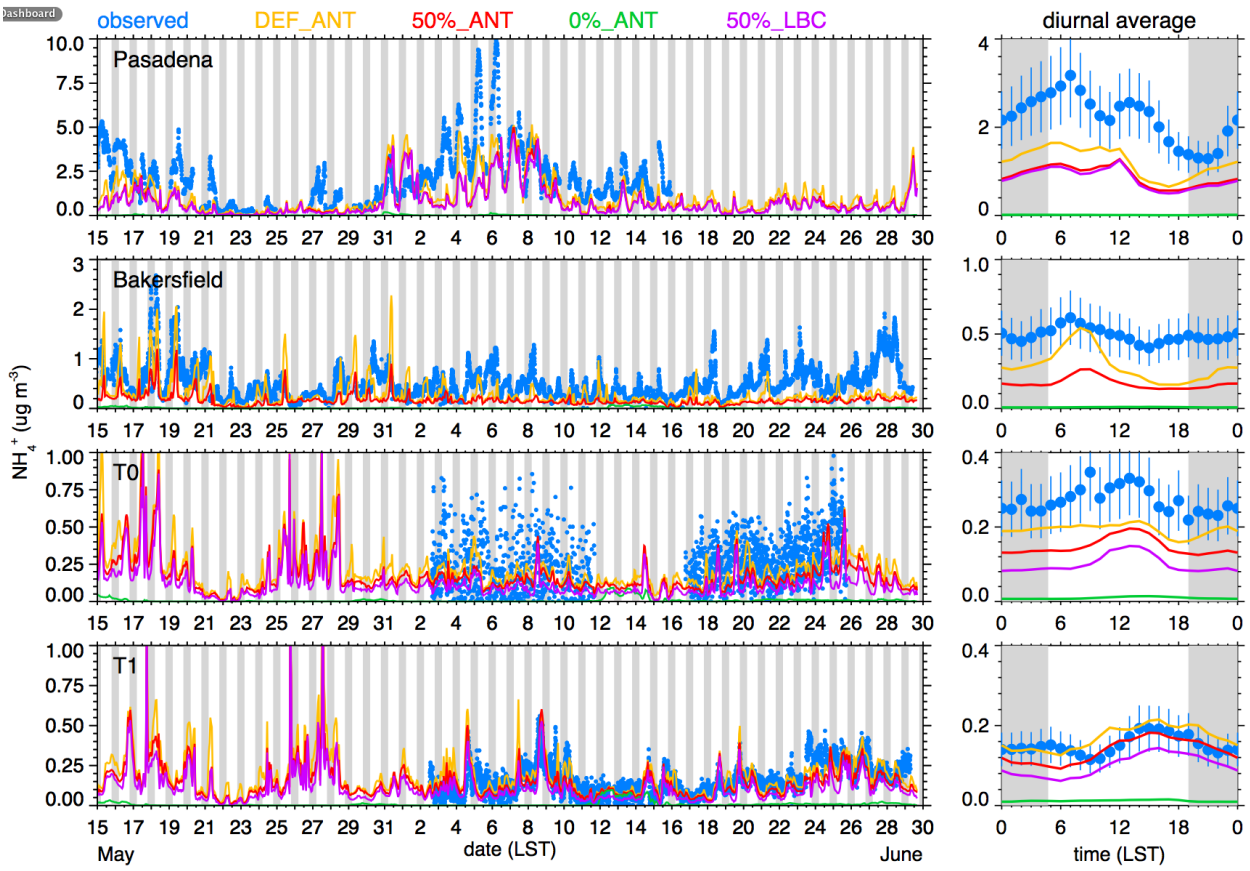

Figure 19. Observed (AMS instrument) and simulated time series (left panels) and average diurnal variation (right panels) of NH_4^+ at the four supersites. Gray shading denote night and vertical lines in right panels denote measurement uncertainty range. Simulated NH_4^+ is the total of the first four model size bins up to 0.625 μm diameter.

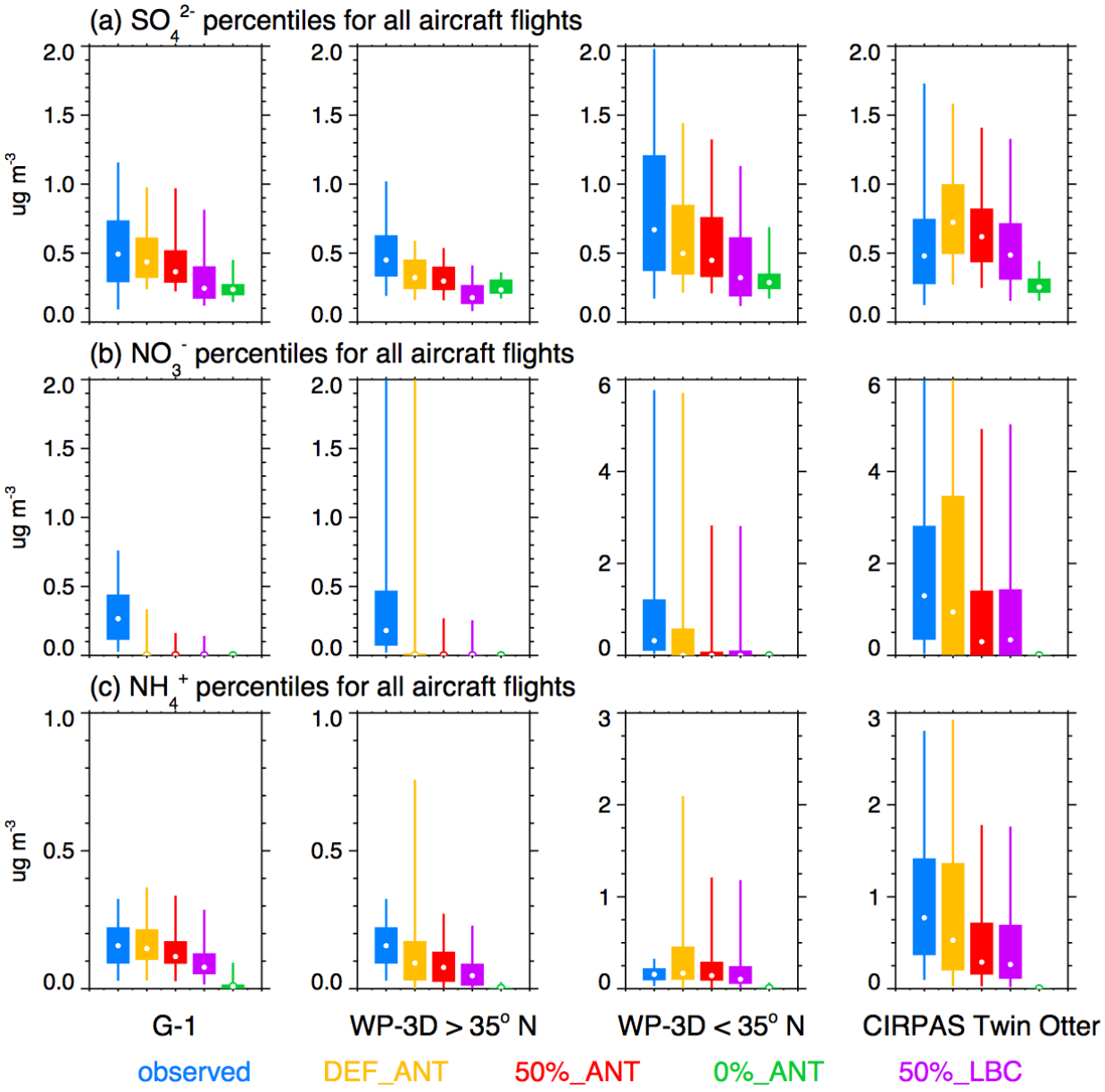

Figure 20. Percentiles for (a) sulfate (SO_4^{2-}), and (b) nitrate (NO_3^-), and ammonium (NH_4^+) for all G-1, WP-3D, and CIRPAS Twin Otter flights. Vertical lines denote 5th and 95th percentiles, boxes denote 25th and 75th percentiles, and the white dots denote the 50th percentiles. Note the scale differs for the northern and southern flights for NO_3^- and NH_4^+.

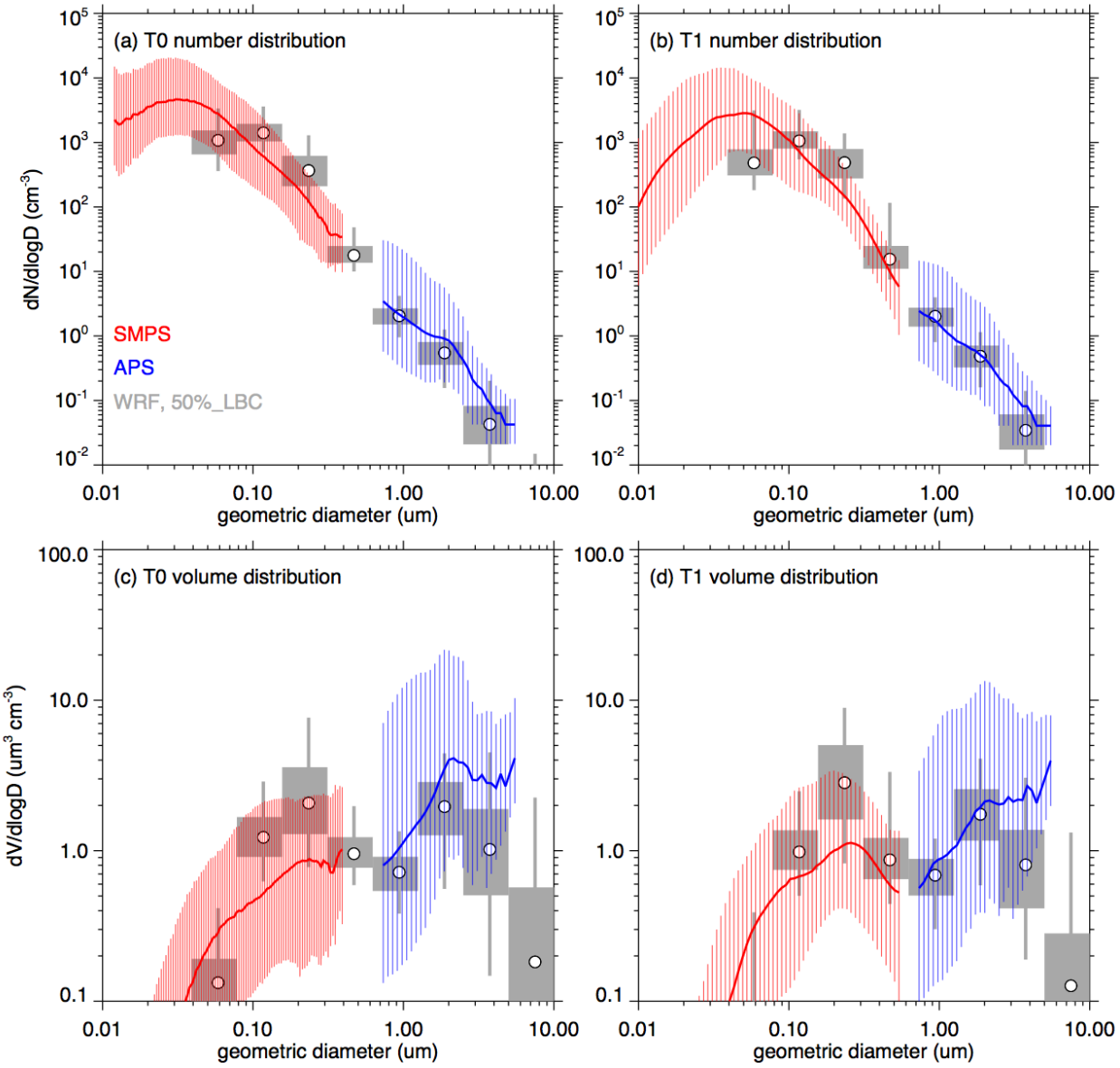

Figure 21. Overall observed aerosol number distribution from the SMPS (red) and APS (blue) instruments at the (a) T0 and (b) T1 sites during June 2010 along with the simulated aerosol number distribution (gray). (c) and (d) same as (a) and (b), except for aerosol volume distribution. Thick red and blue lines denote 50th percentile and thin vertical red and blue lines denote the 5th and 95th percentiles for the observations. Gray vertical lines denote simulated 5th and 95th percentiles, boxes denote 25th and 75th percentiles, and the white dots denote the 50th percentiles.

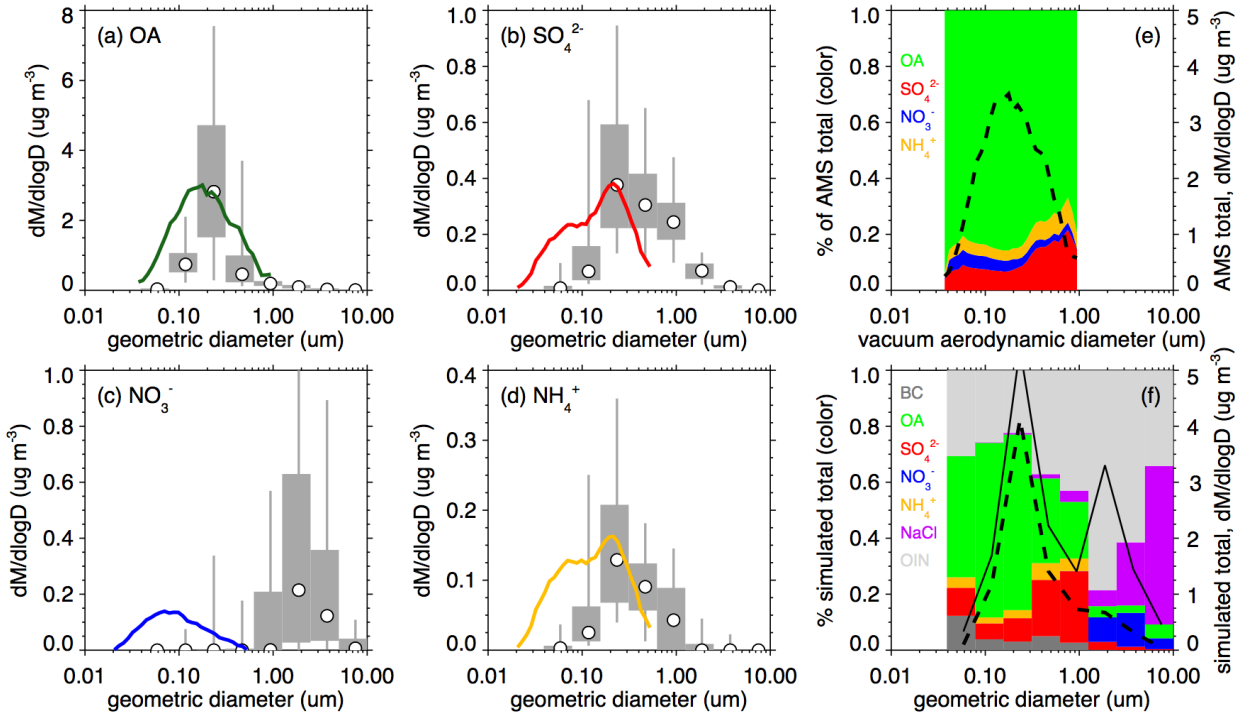

Figure 22. Observed size distribution of (a) OA, (b) SO_4^{2-}, (c) NO_3^-, and (d) NH_4^+ (thick colored lines) at the T1 site along with the percentiles for each size bin from the 50%_LBC simulation (gray). Vertical lines denote 5th and 95th percentiles, boxes denote 25th and 75th percentiles, and the white dots denote the 50th percentiles. (e) and (f) depict % of total mass by composition as well as total mass. Dashed lines in (e) and (f) are for the total of OA, SO_4^{2-}, NO_3^-, and NH_4^+, while the solid line in (f) is for all aerosol components in the model.

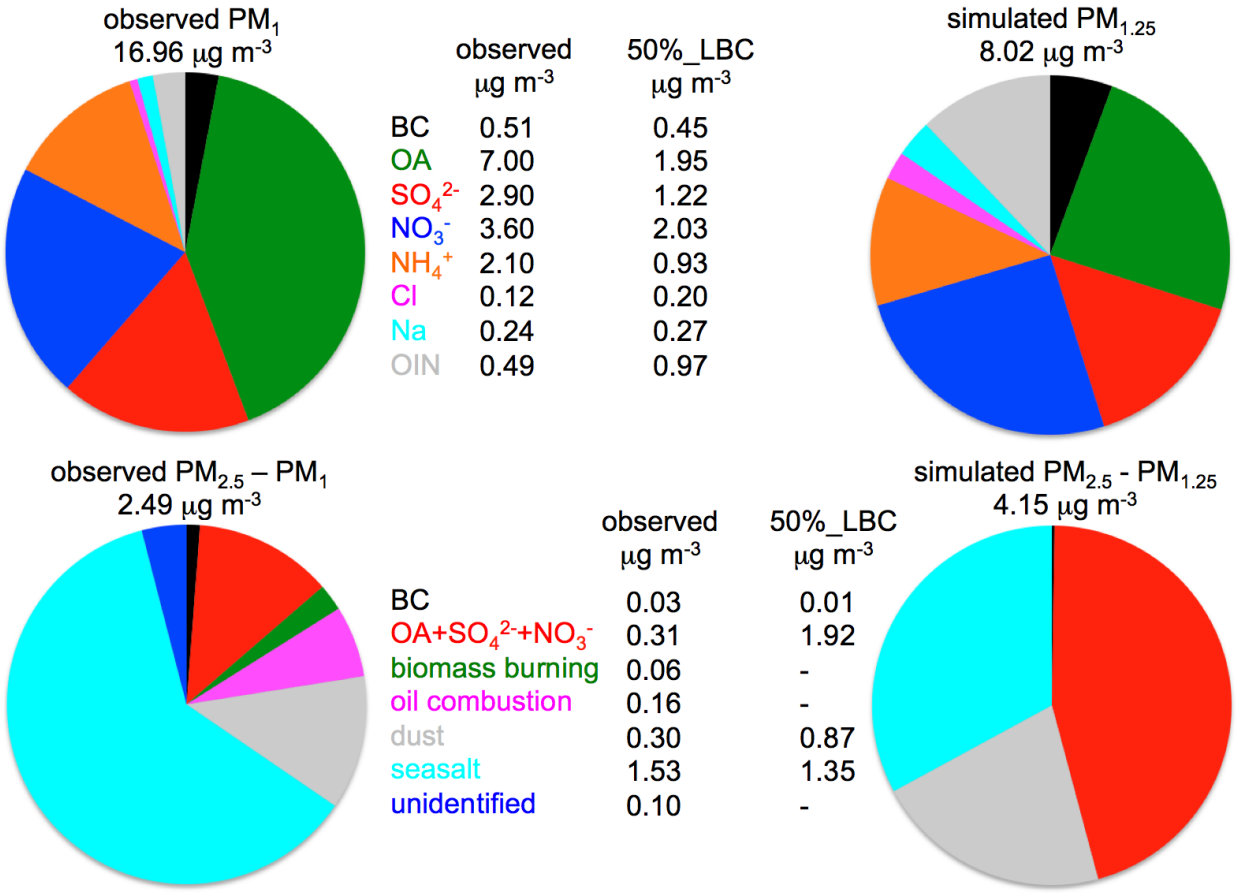

Figure 23. Average aerosol composition observed (left) and simulated (right) at the Pasadena site. Observations adapted from *Hayes et al.* [2013] where PM_1 observations obtained from AMS, EC/OC Sunset Analyzer, and X-ray fluorescence analysis and $PM_{2.5} - PM_1$ observations obtained from PALMS particle types.

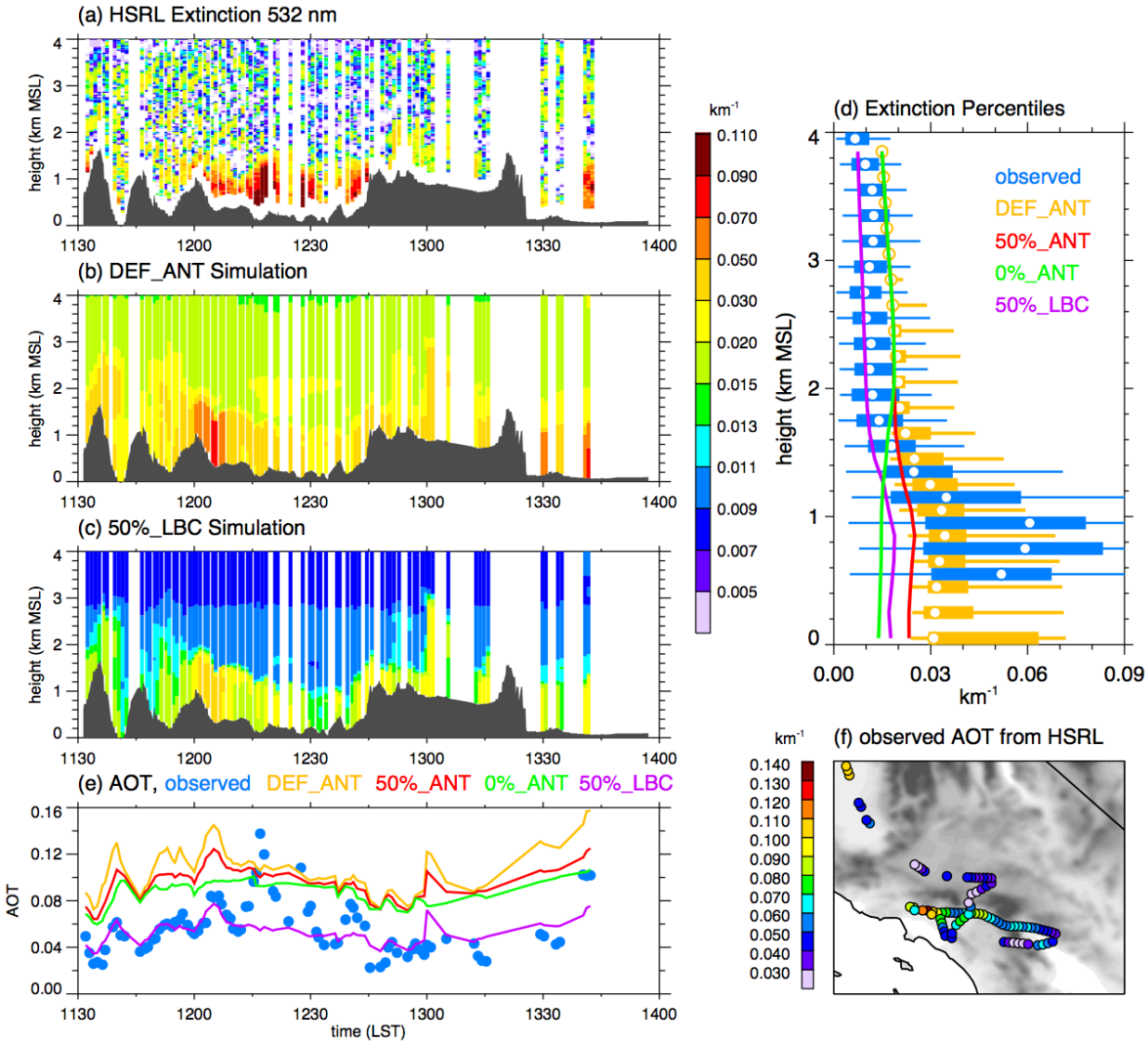

Figure 24. (a) Observed extinction along the B-200 aircraft flight on May 25 over southern California and the corresponding simulated profiles from (b) DEF_ANT and (c) 50%_LBC. (d) Percentiles of extinction as a function of altitude over the entire flight binned for the observations and DEF_ANT simulation, where vertical lines denote 50th percentiles from the 50%_ANT, 0%_ANT, and 50%_LBC simulation. (e) Observed and simulated column integrated AOT obtained from the extinction profiles along the flight path shown in (f).

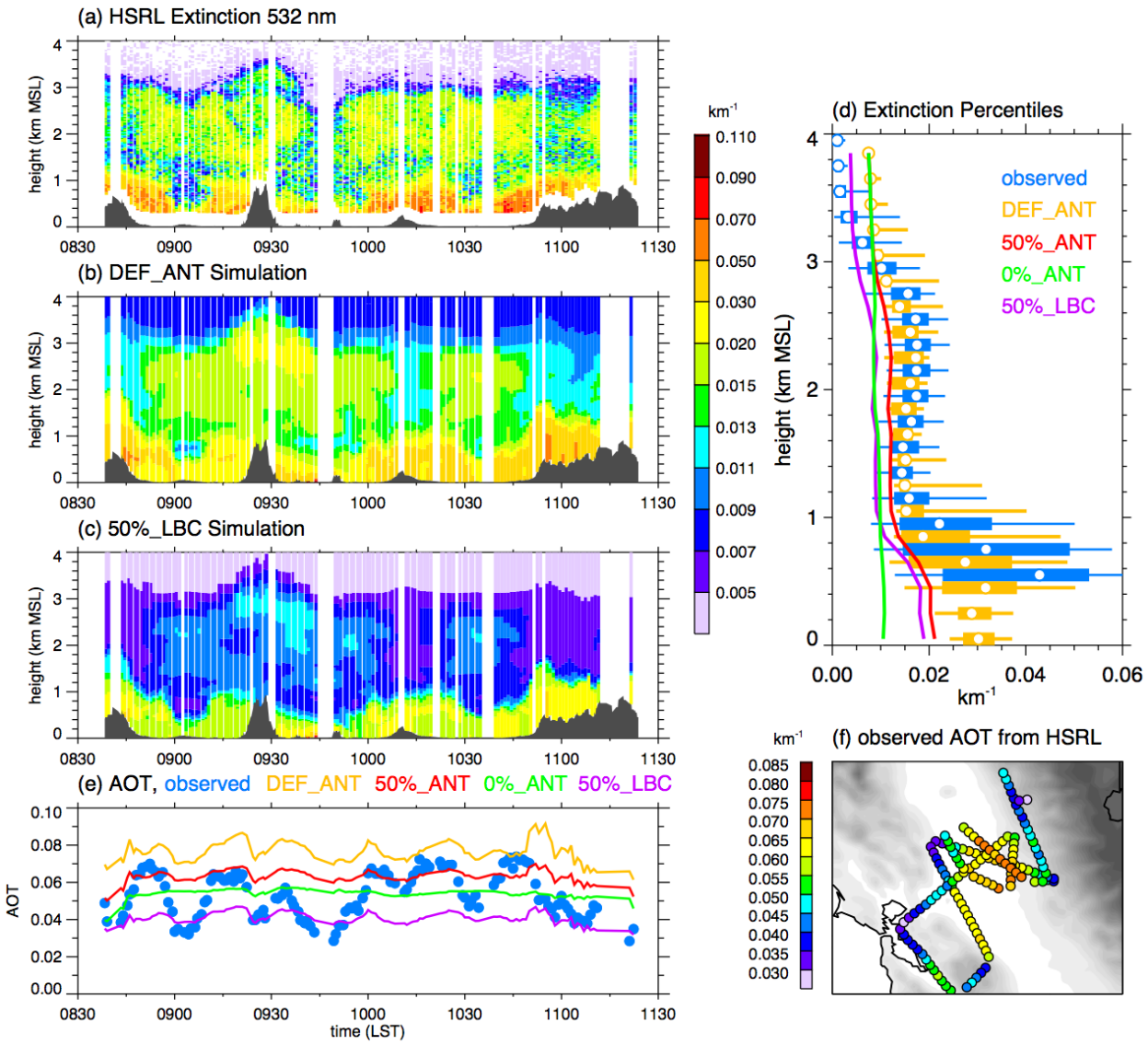

Figure 25. (a) Observed extinction along the B-200 aircraft flight in the vicinity of Sacramento on June 27 and the corresponding simulated profiles from (b) DEF_ANT and (c) 50%_LBC. (d) Percentiles of extinction as a function of altitude over the entire flight binned for the observations and DEF_ANT simulation, where vertical lines denote 50th percentiles from the 50%_ANT, 0%_ANT, and 50%_LBC simulation. (e) Observed and simulated column integrated AOT obtained from the extinction profiles along the flight path shown in (f).

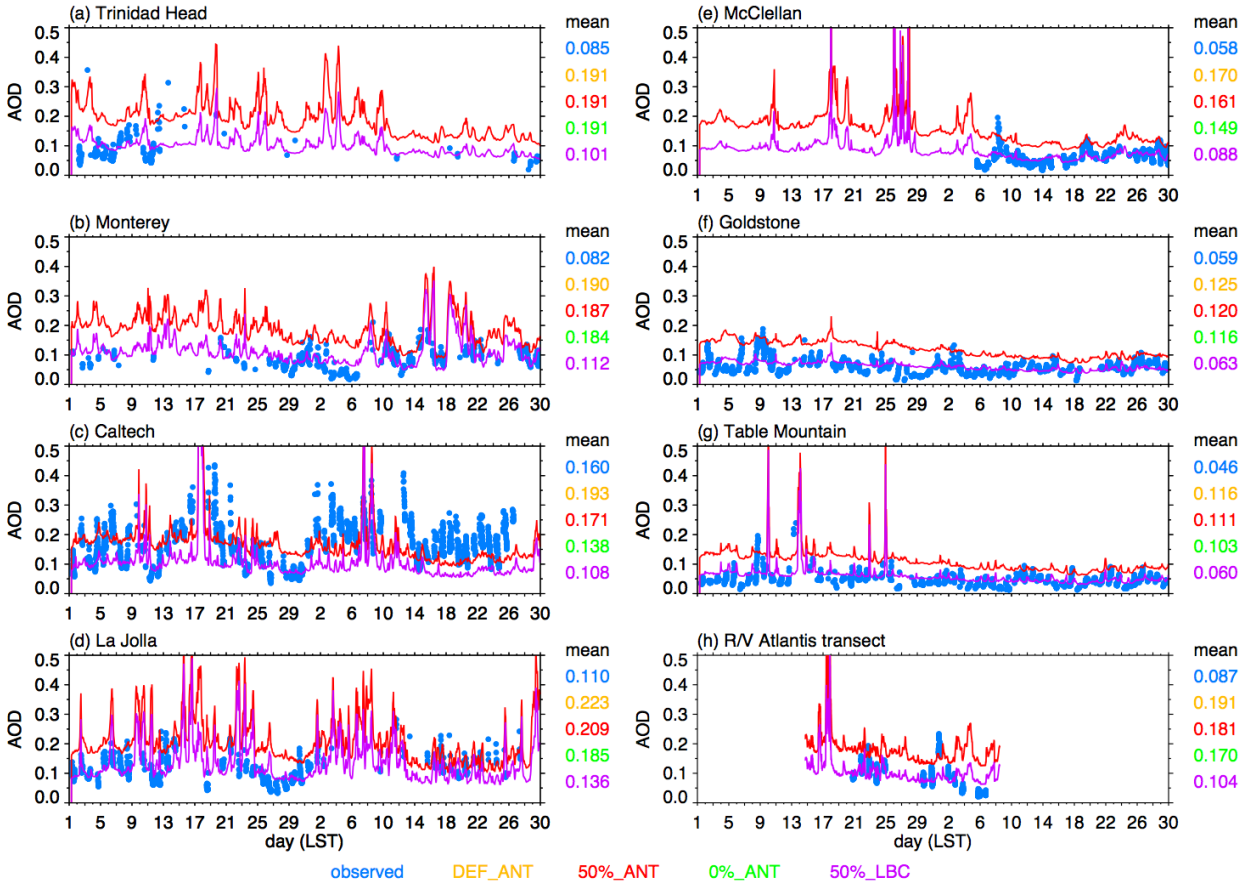

Figure 26. Observed and simulated AOD at 500 nm at the (a) Trinidad Head, (b) Monterey, (c) Caltech, (d) La Jolla, (e) McClellan, (f) Goldstone, and (g) Table Mountain AERONET sites depicted in Figure 1d and (h) along the R/V Atlantis transect depicted in Figure 1a. Average values over the 2-month period are given to the right of each panel.